



applied sciences

Advances in Soil Pollution and Geotechnical Environment

Edited by
Bing Bai

Printed Edition of the Special Issue Published in *Applied Sciences*

Advances in Soil Pollution and Geotechnical Environment

Advances in Soil Pollution and Geotechnical Environment

Editor

Bing Bai

MDPI • Basel • Beijing • Wuhan • Barcelona • Belgrade • Manchester • Tokyo • Cluj • Tianjin



Editor

Bing Bai
School of Civil Engineering
Beijing Jiaotong University
Beijing
China

Editorial Office

MDPI
St. Alban-Anlage 66
4052 Basel, Switzerland

This is a reprint of articles from the Special Issue published online in the open access journal *Applied Sciences* (ISSN 2076-3417) (available at: <https://www.mdpi.com/journal/applsci/special-issues/soil-pollution-geotechnical-environment>).

For citation purposes, cite each article independently as indicated on the article page online and as indicated below:

LastName, A.A.; LastName, B.B.; LastName, C.C. Article Title. <i>Journal Name</i> Year , <i>Volume Number</i> , Page Range.
--

ISBN 978-3-0365-6177-6 (Hbk)

ISBN 978-3-0365-6178-3 (PDF)

© 2022 by the authors. Articles in this book are Open Access and distributed under the Creative Commons Attribution (CC BY) license, which allows users to download, copy and build upon published articles, as long as the author and publisher are properly credited, which ensures maximum dissemination and a wider impact of our publications.

The book as a whole is distributed by MDPI under the terms and conditions of the Creative Commons license CC BY-NC-ND.

Contents

About the Editor	vii
Preface to “Advances in Soil Pollution and Geotechnical Environment”	ix
Bing Bai	
Special Issue on Advances in Soil Pollution and the Geotechnical Environment Reprinted from: <i>Appl. Sci.</i> 2022 , <i>12</i> , 12000, doi:10.3390/app122312000	1
Yi Cai, Jingwen Xing, Ruoyao Huang, Xike Ruan, Nianqing Zhou and Dongze Yi	
Occurrence Characteristics of Inorganic Nitrogen in Groundwater in Silty-Clay Riparian Hyporheic Zones under Tidal Action: A Case Study of the Jingzi River in Shanghai, China Reprinted from: <i>Appl. Sci.</i> 2022 , <i>12</i> , 7704, doi:10.3390/app12157704	3
Min Wang, Jiaming Wen, Heng Zhuang, Weiyi Xia, Ningjun Jiang and Yanjun Du	
Screening Additives for Amending Compacted Clay Covers to Enhance Diffusion Barrier Properties and Moisture Retention Performance Reprinted from: <i>Appl. Sci.</i> 2022 , <i>12</i> , 7341, doi:10.3390/app12147341	21
Gailei Tian and Zhihong Zhang	
A Calculation Method of Thermal Pore Water Pressure Considering Overconsolidation Effect for Saturated Clay Reprinted from: <i>Appl. Sci.</i> 2022 , <i>12</i> , 6325, doi:10.3390/app12136325	39
Junran Zhang, Zhihao Meng, Tong Jiang, Shaokai Wang, Jindi Zhao and Xinxin Zhao	
Experimental Study on the Shear Strength of Silt Treated by Xanthan Gum during the Wetting Process Reprinted from: <i>Appl. Sci.</i> 2022 , <i>12</i> , 6053, doi:10.3390/app12126053	49
Yuedong Wu, Xiangyu Zhou and Jian Liu	
Long-Term Performance of the Water Infiltration and Stability of Fill Side Slope against Wetting in Expressways Reprinted from: <i>Appl. Sci.</i> 2022 , <i>12</i> , 5809, doi:10.3390/app12125809	67
Jihong Qu, Tiangang Yan, Yifeng Zhang, Yuepeng Li, Ran Tian, Wei Guo and Jueyan Jiang	
An Experimental Study on the Migration of Pb in the Groundwater Table Fluctuation Zone Reprinted from: <i>Appl. Sci.</i> 2022 , <i>12</i> , 3870, doi:10.3390/app12083870	81
Yuepeng Li, Liuyue Wang, Xun Zou, Jihong Qu and Gang Bai	
Experimental and Simulation Research on the Process of Nitrogen Migration and Transformation in the Fluctuation Zone of Groundwater Level Reprinted from: <i>Appl. Sci.</i> 2022 , <i>12</i> , 3742, doi:10.3390/app12083742	95
Zhongping Yang, Jiazhao Chang, Xuyong Li, Keshan Zhang and Yao Wang	
The Effects of the Long-Term Freeze–Thaw Cycles on the Forms of Heavy Metals in Solidified/Stabilized Lead–Zinc–Cadmium Composite Heavy Metals Contaminated Soil Reprinted from: <i>Appl. Sci.</i> 2022 , <i>12</i> , 2934, doi:10.3390/app12062934	117
Lianfei Kuang, Qiyin Zhu, Xiangyu Shang and Xiaodong Zhao	
Molecular Dynamics Simulation of Nanoscale Elastic Properties of Hydrated Na-, Cs-, and Ca-Montmorillonite Reprinted from: <i>Appl. Sci.</i> 2022 , <i>12</i> , 678, doi:10.3390/app12020678	133

Xinpei Yu, Hongbin Xiao, Zhenyu Li, Junfeng Qian, Shenping Luo and Huanyu Su Experimental Study on Microstructure of Unsaturated Expansive Soil Improved by MICP Method Reprinted from: <i>Appl. Sci.</i> 2022 , <i>12</i> , 342, doi:10.3390/app12010342	149
Ruxue Liu, Xinru Yang, Jiayin Xie, Xiaoyu Li and Yongsheng Zhao Experimental Investigation on the Effects of Ethanol-Enhanced Steam Injection Remediation in Nitrobenzene-Contaminated Heterogeneous Aquifers Reprinted from: <i>Appl. Sci.</i> 2021 , <i>11</i> , 12029, doi:10.3390/app112412029	163
Yuedong Wu, Hui Liu and Jian Liu Use of Foamed Cement Banking for Reducing Expressways Embankment Settlement Reprinted from: <i>Appl. Sci.</i> 2021 , <i>11</i> , 11959, doi:10.3390/app112411959	179
Wenfang Chen, Yaobin Zhang, Weiwei Shi, Yali Cui, Qiulan Zhang, Yakun Shi and Zexin Liang Analysis of Hydrogeochemical Characteristics and Origins of Chromium Contamination in Groundwater at a Site in Xinxiang City, Henan Province Reprinted from: <i>Appl. Sci.</i> 2021 , <i>11</i> , 11683, doi:10.3390/app112411683	189

About the Editor

Bing Bai

Bing Bai is currently a professor working at the Beijing Jiaotong University, Beijing, China. He holds a Ph.D. in Geotechnical Engineering from Wuhan University, China. His research interests include geo-environmental engineering, thermal consolidation theory, and contaminant transport theory and control methods. Recently, he devoted himself to research on advances in soil pollution and geotechnical environments. He developed a theory describing the cotransport of heavy metals and suspended particles at different temperatures in porous media and proposed a nonlinear attachment–detachment model with hysteresis suitable for substances with sizes ranging from ions to large particles, which is of great significance in understanding groundwater pollution mechanisms and in the development of purification technology. He has published more than 150 academic papers and five scientific books. He serves as an editorial board member of the *Journal of Geotechnical Engineering and Rock and Soil Mechanics of China*. He is the member of several professional committees, such as the Special Committee on Soil Constitutive Relationship, the Strength of China Society of Civil Engineering, and the Special Committee on Energy Underground Structure and Engineering of the Chinese Society of Rock Mechanics

Preface to “Advances in Soil Pollution and Geotechnical Environment”

Soil pollution and disposal technology is currently a hot topic in geo-environmental engineering that involves the interaction of mechanisms, migration processes, and treatment measures of various types of pollutants (e.g., heavy metals, organic pollutants, acid or alkali substances, and radioactive materials) with geotechnical media, as well as heat flow processes and thermal damage. Application areas include industrial pollutant treatment in shallow seepage, groundwater exploitation, geothermal resource development, thermal energy storage, waste disposal in metal mining, and landfill leachate barriers.

This Special Issue on: “Advances in Soil Pollution and the Geotechnical Environment” addresses the most recent developments in soil pollution and restoration, contaminant hydrology, and ground disturbance to stimulate fruitful technical and scientific interactions between professionals.

A total of thirteen papers in various fields of soil pollution and the geotechnical environment, including soil pollution, soil restoration, and heat transfer in soils, are presented in this Special Issue. Although the submissions for this Special Issue have been closed, more in-depth research in the field of soil pollution and the geotechnical environment continues to address the challenges we face today, such as soil pollution mechanisms, pollutant migration, and the remediation efficiency of pollutants.

Thanks to all the authors and peer reviewers for their valuable contributions to this the Special Issue, “Advances in Soil Pollution and the Geotechnical Environment”. I would also like to express my gratitude to all the staff and people involved in the creation of this Special Issue.

Bing Bai
Editor

Editorial

Special Issue on Advances in Soil Pollution and the Geotechnical Environment

Bing Bai

School of Civil Engineering, Beijing Jiaotong University, Beijing 100044, China; bbai@bjtu.edu.cn

Soil pollution and disposal technology is currently a hot topic in geo-environmental engineering that involves the interaction mechanisms, migration processes, and treatment measures of various types of pollutants (e.g., heavy metals, organic pollutants, acid or alkali substances, and radioactive materials) with geotechnical media, as well as heat flow processes and thermal damage. Application areas include industrial pollutant treatment in shallow seepage, groundwater exploitation, geothermal resource development, thermal energy storage, waste disposal in metal mining, and landfill leachate barriers.

This Special Issue on *Advances in Soil Pollution and the Geotechnical Environment* addresses the most recent developments in soil pollution and restoration, contaminant hydrology, and ground disturbance to stimulate fruitful technical and scientific interactions between professionals.

A total of thirteen papers in various fields of soil pollution and the geotechnical environment, including soil pollution, soil restoration, and heat transfer in soils, are presented in this Special Issue. To comprehend the effect of tidal actions on the nitrogen cycle in silty-clay riparian hyporheic zones, Cai et al. [1] carried out the synchronous monitoring of water level and water quality along a test transect during a spring tidal period and measured the permeability and chemical composition of soil samples from drilled holes. Wang et al. [2] presented a systemic laboratory experimental investigation on the liquid–plastic limit, moisture retention, hydraulic conductivity, and gas diffusion barrier properties of compacted clay amended with attapulgite and diatomite to control desiccation cracks and the migration of water and volatile organic compounds. Tian et al. [3] proposed a calculation method for thermal pore water pressure while considering the overconsolidation effect of saturated clay, which was verified by the relevant experimental data. Zhang et al. [4] explored the effect and mechanism of xanthan gum treatment on the water retention and shear strength characteristics of silt during the wetting process. Wu et al. [5] proposed a novel subgrade using a capillary barrier to reduce the different settlements and stabilities based on seepage theory for unsaturated soils. Qu et al. [6] investigated the migration, adsorption, and desorption characteristics of Pb^{2+} on fine, medium, and coarse sand in a water table fluctuation zone using several laboratory methods, including the kinetic aspects of Pb^{2+} adsorption/desorption and water table fluctuation experiments. Li et al. [7] carried out physical experiments on the nitrogen migration and transformation processes in a groundwater level fluctuation zone and constructed a numerical model for nitrogen migration in a vadose zone and a saturated zone using the software HydrUS-1D. Yang et al. [8] conducted a long-term F–T study of S/S Pb–Zn–Cd composite HM-contaminated soil under six conditions (0, 3, 7, 14, 30, and 90 cycles), with each F–T cycle process lasting 24 h. Kuang et al. [9] simulated the nanoscale elastic properties of hydrated Na-, Cs-, and Ca-MMT with unconstrained system atoms using a molecular dynamics (MD) method. Yu et al. [10] discussed the soil–water characteristic curve and microstructure evolution of unsaturated expansive soil improved by microorganisms in Nanning, Guangxi by means of a filter paper method and scanning electron microscope imaging (SEM). Liu et al. [11] investigated the removal effect of nitrobenzene in an aquifer through a series of two-dimensional sandbox experiments with different stratigraphic structures. Wu et al. [12] proposed a

Citation: Bai, B. Special Issue on Advances in Soil Pollution and the Geotechnical Environment. *Appl. Sci.* **2022**, *12*, 12000. <https://doi.org/10.3390/app122312000>

Received: 19 November 2022

Accepted: 23 November 2022

Published: 24 November 2022

Publisher's Note: MDPI stays neutral with regard to jurisdictional claims in published maps and institutional affiliations.



Copyright: © 2022 by the author. Licensee MDPI, Basel, Switzerland. This article is an open access article distributed under the terms and conditions of the Creative Commons Attribution (CC BY) license (<https://creativecommons.org/licenses/by/4.0/>).

sedimentation ratio calculation method through the analysis of the settlement load ratio to calculate the roadbed replacement thickness. Chen et al. [13] investigated a contaminated site in Xinxiang City, Henan Province and collected 92 groundwater samples from the site to identify the groundwater chemical characteristics of the sites and their control mechanisms for the remediation of pollutants.

Although the submissions for this Special Issue have been closed, more in-depth research in the field of soil pollution and the geotechnical environment continues to address the challenges we face today, such as soil pollution mechanisms, pollutant migration, and the remediation efficiency of pollutants [14].

Funding: This research received no external funding.

Acknowledgments: Thanks to all the authors and peer reviewers for their valuable contributions to this Special Issue *Advances in Soil Pollution and the Geotechnical Environment*. I would also like to express my gratitude to all the staff and people involved with this Special Issue.

Conflicts of Interest: The author declares no conflict of interest.

References

1. Cai, Y.; Xing, J.; Huang, R.; Ruan, X.; Zhou, N.; Yi, D. Occurrence Characteristics of Inorganic Nitrogen in Groundwater in Silty-Clay Riparian Hyporheic Zones under Tidal Action: A Case Study of the Jingzi River in Shanghai, China. *Appl. Sci.* **2022**, *12*, 7704. [[CrossRef](#)]
2. Wang, M.; Wen, J.; Zhuang, H.; Xia, W.; Jiang, N.; Du, Y. Screening Additives for Amending Compacted Clay Covers to Enhance Diffusion Barrier Properties and Moisture Retention Performance. *Appl. Sci.* **2022**, *12*, 7341. [[CrossRef](#)]
3. Tian, G.; Zhang, Z. A Calculation Method of Thermal Pore Water Pressure Considering Overconsolidation Effect for Saturated Clay. *Appl. Sci.* **2022**, *12*, 6325. [[CrossRef](#)]
4. Zhang, J.; Meng, Z.; Jiang, T.; Wang, S.; Zhao, J.; Zhao, X. Experimental Study on the Shear Strength of Silt Treated by Xanthan Gum during the Wetting Process. *Appl. Sci.* **2022**, *12*, 6053. [[CrossRef](#)]
5. Wu, Y.; Zhou, X.; Liu, J. Long-Term Performance of the Water Infiltration and Stability of Fill Side Slope against Wetting in Expressways. *Appl. Sci.* **2022**, *12*, 5809. [[CrossRef](#)]
6. Qu, J.; Yan, T.; Zhang, Y.; Li, Y.; Tian, R.; Guo, W.; Jiang, J. An Experimental Study on the Migration of Pb in the Groundwater Table Fluctuation Zone. *Appl. Sci.* **2022**, *12*, 3870. [[CrossRef](#)]
7. Li, Y.; Wang, L.; Zou, X.; Qu, J.; Bai, G. Experimental and Simulation Research on the Process of Nitrogen Migration and Transformation in the Fluctuation Zone of Groundwater Level. *Appl. Sci.* **2022**, *12*, 3742. [[CrossRef](#)]
8. Yang, Z.; Chang, J.; Li, X.; Zhang, K.; Wang, Y. The Effects of the Long-Term Freeze–Thaw Cycles on the Forms of Heavy Metals in Solidified/Stabilized Lead–Zinc–Cadmium Composite Heavy Metals Contaminated Soil. *Appl. Sci.* **2022**, *12*, 2934. [[CrossRef](#)]
9. Kuang, L.; Zhu, Q.; Shang, X.; Zhao, X. Molecular Dynamics Simulation of Nanoscale Elastic Properties of Hydrated Na-, Cs-, and Ca-Montmorillonite. *Appl. Sci.* **2022**, *12*, 678. [[CrossRef](#)]
10. Yu, X.; Xiao, H.; Li, Z.; Qian, J.; Luo, S.; Su, H. Experimental Study on Microstructure of Unsaturated Expansive Soil Improved by MICP Method. *Appl. Sci.* **2022**, *12*, 342. [[CrossRef](#)]
11. Liu, R.; Yang, X.; Xie, J.; Li, X.; Zhao, Y. Experimental Investigation on the Effects of Ethanol-Enhanced Steam Injection Remediation in Nitrobenzene-Contaminated Heterogeneous Aquifers. *Appl. Sci.* **2021**, *11*, 12029. [[CrossRef](#)]
12. Wu, Y.; Liu, H.; Liu, J. Use of Foamed Cement Banking for Reducing Expressways Embankment Settlement. *Appl. Sci.* **2021**, *11*, 11959. [[CrossRef](#)]
13. Chen, W.; Zhang, Y.; Shi, W.; Cui, Y.; Zhang, Q.; Shi, Y.; Liang, Z. Analysis of Hydrogeochemical Characteristics and Origins of Chromium Contamination in Groundwater at a Site in Xinxiang City, Henan Province. *Appl. Sci.* **2021**, *11*, 11683. [[CrossRef](#)]
14. Bai, B.; Bai, F.; Li, X.; Nie, Q.; Jia, X.; Wu, H. The remediation efficiency of heavy metal pollutants in water by industrial red mud particle waste. *Environ. Technol. Innov.* **2022**, *28*, 102944. [[CrossRef](#)]

Article

Occurrence Characteristics of Inorganic Nitrogen in Groundwater in Silty-Clay Riparian Hyporheic Zones under Tidal Action: A Case Study of the Jingzi River in Shanghai, China

Yi Cai ^{1,2,*}, Jingwen Xing ¹, Ruoyao Huang ¹, Xike Ruan ¹, Nianqing Zhou ^{1,*} and Dongze Yi ¹

¹ Department of Hydraulic Engineering, College of Civil Engineering, Tongji University, Shanghai 200092, China; 2032262@tongji.edu.cn (J.X.); 2032261@tongji.edu.cn (R.H.); xkruan007@163.com (X.R.); 2132630@tongji.edu.cn (D.Y.)

² The Yangtze River Water Environment Key Laboratory of the Ministry of Education, Tongji University, Shanghai 200092, China

* Correspondence: caiyi@tongji.edu.cn (Y.C.); nq.zhou@tongji.edu.cn (N.Z.)

Abstract: For comprehending the effect of tidal action on nitrogen cycle in silty-clay riparian hyporheic zones, the synchronous monitoring of water level and water quality was carried out along a test transect during a spring tidal period from 21 to 23 October 2021. Moreover, the permeability and chemical composition of soil samples from drilled holes were measured. Subsequently, the spatiotemporal variation of inorganic nitrogen concentrations in the groundwater in the riparian hyporheic zone was investigated during the study period, and the potential reason was discussed. It is shown that the delayed response time of groundwater level in the silty-clay riparian zone to the tide-driven fluctuation of the river stage increased with distance from the shore and reached 3.0 h at the position 3.83 m away from the shore. The continuous infiltration of the river water under tide action contributed to the aerobic and neutral riparian hyporheic zone conducive to nitrification. Within 4 m away from the bank, the dominant inorganic nitrogen form changed from NO_3^- -N to NH_4^+ -N, upon increasing the distance from the bank. Additionally, the removal of nitrogen could occur in the riparian hyporheic zone with aerobic and neutral environment under the conjoint control of nitrification, microbial assimilation, and aerobic denitrification.

Keywords: tidal action; silty-clay soil; riparian hyporheic zone; inorganic nitrogen; occurrence characteristics; influencing factors

Citation: Cai, Y.; Xing, J.; Huang, R.; Ruan, X.; Zhou, N.; Yi, D. Occurrence Characteristics of Inorganic Nitrogen in Groundwater in Silty-Clay Riparian Hyporheic Zones under Tidal Action: A Case Study of the Jingzi River in Shanghai, China. *Appl. Sci.* **2022**, *12*, 7704. <https://doi.org/10.3390/app12157704>

Academic Editor: Bing Bai

Received: 20 May 2022

Accepted: 28 July 2022

Published: 30 July 2022

Publisher's Note: MDPI stays neutral with regard to jurisdictional claims in published maps and institutional affiliations.



Copyright: © 2022 by the authors. Licensee MDPI, Basel, Switzerland. This article is an open access article distributed under the terms and conditions of the Creative Commons Attribution (CC BY) license (<https://creativecommons.org/licenses/by/4.0/>).

1. Introduction

In order to ensure the security of the global food supply, a large amount of nitrogen fertilizer has been utilized in the past few decades. For example, the average nitrogen utilization has achieved the rate of 305 kg/hm² in China [1]. Excessive bioavailable nitrogen such as nitrate nitrogen (NO_3^-) and ammonia nitrogen (NH_4^+) in rivers will lead to water eutrophication and, consequently, damage the ecological balance of river systems. Particularly in coastal areas, nitrogen pollution in rivers is generally serious due to dense population and active industry and agriculture production. If it cannot be maintained under effective control, the excessive nitrogen will continue to enter the ocean and further affect the health of the coastal ecosystem and the sustainable utilization of marine resources.

Hyporheic zones of river ecosystem are water-saturated sediment (known as aquifer) below the riverbed and extending to the riparian areas on both sides. It is not only a key area for water exchange and solute migration between river and groundwater, but also an important place for microbial growth and metabolism. Mass exchange and energy transfer are frequent and biogeochemical reactions are complex within a hyporheic zone, which is of great significance to the structure, function, and health of river ecosystem [2–4]. Nitrogen

is transported between rivers and their riparian zones through hyporheic exchange and transformed between different chemical forms (e.g., NH_4^+ , NO_3^- , nitrite nitrogen (NO_2^-), and N_2) through biogeochemical reactions [5]. Therefore, to realize the effective control of nitrogen pollution in rivers, it is necessary to fully comprehend nitrogen migration and transformation in groundwater in hyporheic zones.

Nitrogen in groundwater in a hyporheic zone varies geographically, and its form changes temporally, which forms a complex dynamic cycle [6–9]. Some hydrological events (e.g., rainstorm, flooding, reservoir discharge, and tidal action) can change the recharge relationship between river water and groundwater, consequently influencing nitrogen migration in hyporheic zones [10–13]. Shibata et al. carried out onsite monitoring to study the water exchange and the change in nitrogen concentration in the hyporheic zone during the rainstorm. It was found that the increase in nitrogen concentration in the hyporheic zone was mainly caused by the rainwater infiltration through the overlying unsaturated zone rather than the lateral seepage from the river [14]. The research conducted by Singh et al. indicated that the flood process extended the mixing range of surface water and groundwater and had a significant impact on the mass cycle in the riverbed hyporheic zone [15]. Sawyer et al. studied the impact of the reservoir operation on the lateral hyporheic exchange, and the results showed that the impact range could extend to 1–5 m away from the shore [16]. Unlike the hydrological events mentioned above, tides exhibit periodicity, and the tidal period is usually about 12 or 24 h. This makes the hyporheic exchange more frequent and the biogeochemical process in the hyporheic zone more complex [17]. In recent years, there has been growing concern over the hyporheic zones of tidal rivers. Musial et al. quantified the tide-driven hyporheic exchange fluxes across the bank and the bed and deduced that the tidal bank storage in the sandy hyporheic zone might remove nutrients from rivers [18]. The geochemical measurements and numerical simulation performed by Barnes et al. showed that it was possible that the hyporheic zone with permeable sediment and low organic matter content could be a source of nitrate to the tidal river [19].

Hydrogeological conditions and ecological factors could affect the nitrogen cycle in hyporheic zones [20–22]. McGarr et al. investigated the hyporheic exchange process in a sand–gravel mixed riverbed and pointed it out that the pore water flowed preferentially through the sediment of high-permeability, which affected nitrogen transport pathways [23]. The sediment heterogeneity could result in the existence of tiny anoxic blocks within the aerobic zone near the shore, thus affecting nitrogen processing [24]. The retention time of river water is usually extended in the low-permeability riverbed sediment, which is beneficial to the full reaction between nitrogen and dissolved oxygen (DO) [25]. In addition, the migration ability of NH_4^+ in the hyporheic zone may be limited to a certain extent due to the electrostatic attraction by soil particles [26]. Eco-environmental factors mainly include the reactant concentration, redox potential (Eh), temperature (T), and pH [27–29]. The nitrogen-related biogeochemical reactions such as nitrification and denitrification are greatly governed by DO concentration and Eh in hyporheic zones [30]. Dissolved organic carbon (DOC) is another key factor controlling the nitrogen cycle, and increasing DOC concentration could promote denitrification [31]. Zarnetske et al. found that DOC and DO could be preferentially consumed in the near-shore hyporheic zone [32]. Additionally, temperature could affect the microbial activity, reaction rate, and DO concentration, consequently influencing the process of nitrogen cycle in the hyporheic zone [33,34]. Some studies demonstrated that pH showed a positive correlation with NO_3^- concentration and a negative one with NH_4^+ concentration [35].

Although the nitrogen cycle in hyporheic zones has been extensively studied, there is little work aiming at the case of low-permeability riparian hyporheic zones of tidal rivers. At present, the mechanism underlying how tides drive nitrogen migration and transformation in riparian hyporheic zones with low permeability sediment is not very clear. The main objective of the study was to characterize the spatiotemporal variations of various inorganic nitrogen concentrations in groundwater in poorly permeable hyporheic

zones of tidal rivers and discuss the potential reason why such variations existed. A representative transect was chosen to carry out the drilling, monitoring, and sampling. By means of onsite monitoring and lab analysis, the response of the riparian groundwater level to the tide-driven fluctuation of the river stage was studied, the spatiotemporal variations of inorganic nitrogen concentrations in the groundwater in the riparian hyporheic zone were analyzed, and the potential influencing factors were discussed. The results are expected to enrich the theory of river hyporheic zones and provide a scientific basis for nitrogen pollution treatment of tidal rivers.

2. Methodology

2.1. Field Monitoring

The test site was located on the riverbank of the Jingzi River, a tributary of the Huangpu River in Shanghai, China, as illustrated in Figure 1. The Huangpu River, with a total length of approximately 114 km, is the last tributary of the Yangtze River before it empties into the East China Sea. The Huangpu River estuary forms a medium-tidal shallow-water environment where the tides are of irregular semidiurnal features. The tides can penetrate up to the Dianshan Lake and the provincial boundary between Zhejiang and Shanghai. On an average, the tidal period is about 12.5 h, where 4.5 h involves flooding and the remainder involves ebbing [36]. At the Wusong tide gauge station, the average tidal prism is about $5.8 \times 10^7 \text{ m}^3$, the flood current velocity is up to $1.2 \times 10^4 \text{ m}^3/\text{s}$, and the mean tidal range is about 2.27 m [37]. The test site was located about 29 km upstream of the Wusong tide gauge station. According to the preliminary research, there was a good response relationship between the river stages at the test site and the sea levels at Wusong station. The flooding at the test site was about 2.5 h behind that at Wusong station. Furthermore, the fluctuation range of the river stage at the site was up to approximately 0.5 m.

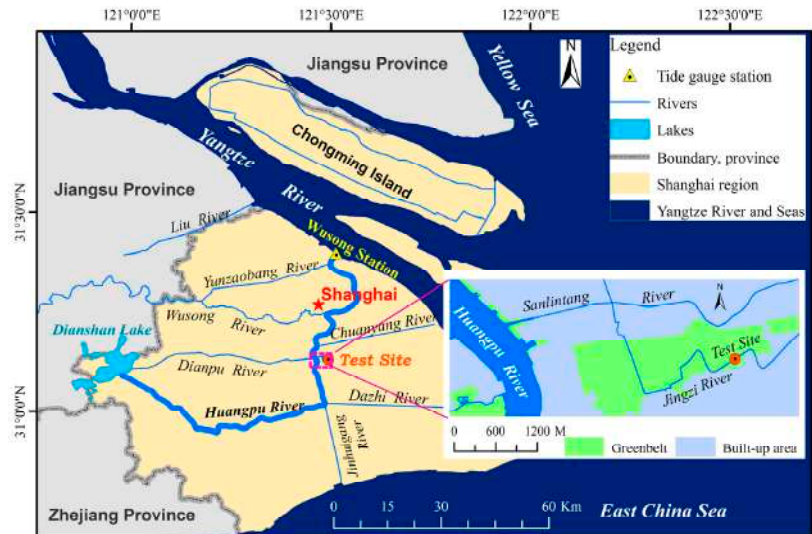


Figure 1. Location of the test site.

The land use is mainly green field and residential in the surrounding area of the test site. The green field is unused and covered with bushes and stunted trees. The Jingzi River flows through the greenbelt, serving as a sewage channel of the vicinity. The terrain around the test site is relatively flat, and the slope degree of the bank is less than 9° . The riverbed sediment and the shallow aquifer materials at the site consist of silty-clay soils extensively distributed on the floodplain of the Huangpu River. The site with gentle slope, poorly permeable sediment, and less interference was considered suitable for the investigation.

The site was instrumented with a perpendicular transect of observation wells and sampling points, as shown in Figure 2. One observation well marked as WR0 was set in the river channel, and four other wells (i.e., WB1, WB2, WB3, and WB4) were laid on the riverbank, 0.71 m, 1.11 m, 2.43 m, and 3.85 m away from the shore, respectively (Figure 2a). The well pipes, made of polyvinyl chloride (PVC) material, were equipped with pipe covers at both ends. A hole punch was employed to make scattered tiny holes with a diameter of about 5 mm in the wall of the pipes. A nylon cloth with a mesh size of 0.15–0.20 mm was wrapped around each pipe. The wells on the riverbank were 200 cm in length and 11 cm in diameter, while WR0 was 80 cm in length and 6 cm in diameter. Each well tube was inserted vertically into the sediment. A high-precision GPS (Z-Survey i70, Manufacturer: CHCNAV Co. Ltd., Shanghai, China) and a leveling instrument (B30, Manufacturer: SOKKIA Co. Ltd., Tokyo, Japan) were used to survey the top elevation of each well. One water-level sensor (HOBO Kit-D-U20-04, Manufacturer: ONSET Co. Ltd., Bourne, Cape Cod, Centerville, MA, USA) was installed at the bottom of each well, with a data collection interval of 5 min.

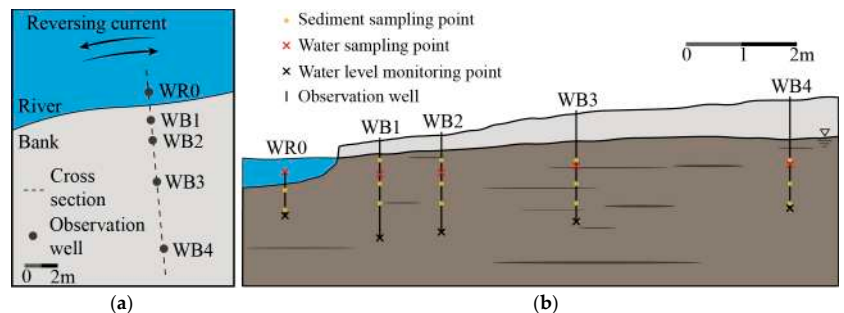


Figure 2. The transect for monitoring and sampling: (a) the top view; (b) the cross-section.

According to the preliminary work, the fluctuation range of the Jingzi River stage was mostly less than 0.5 m, and the change in groundwater table could not be observed as the river stage fluctuation was smaller than 10 cm (usually occurred during neap tides). Thus, a spring tide period without rain should be chosen to focus on the impact of tides. According to the tide prediction table and the weather forecast information released in Shanghai, the 3 day spring tide period from 21 to 23 October 2021 was selected to carry out the monitoring of water level and water quality. The data recorded by the water-level sensors were exported and processed through atmospheric pressure correction. A portable dissolved oxygen meter (LDO™, Manufacturer: HACH Co. Ltd., Loveland, CO, USA) and a portable multiparameter water quality analyzer (sensION+ MM156, Manufacturer: HACH Co. Ltd., Loveland, CO, USA) were employed to synchronously determine DO concentration, temperature, and pH in the river channel and the four riparian wells.

2.2. Sample Collection

During the drilling of five wells, 14 columnar sediment samples with a diameter of 70 mm and height of 200 mm were collected using a stainless-steel soil sampler. The riverbed sediment samples were collected at the depths of 10–30 cm and 40–60 cm below the riverbed at WR0. Considering the depth distribution of the groundwater table in the riparian zone, the riparian sediment samples were individually collected at the depth of 40–120 cm below the surface at WB1, at the depth of 50–130 cm below the surface at WB2, at the depth of 100–180 cm below the surface at WB3, and at the depth of 120–200 cm below the surface at WB4. The three sediment samples were collected from each riparian borehole at equal intervals. All sediment samples were stored in the separate bags in a cooling box keeping the temperature below 5 °C and then taken back to the lab for testing within 24 h. Sediment samples collected were divided into two aliquots: one for determining

the contents of total nitrogen (TN) and total carbon (TC), and the other for analyzing permeability coefficient (K), particle size, and sediment type.

Water samples were collected from the river and the four wells using a liquid sampling tube with a total capacity of 500 mL. Water sampling was carried out at 2 h intervals from 6:00 a.m. to 6:00 p.m. on any particular day of 21–23 October 2021. The water sampling points were 50 cm below the free water table. Figure 2b presents the positions of the sediment and water sampling points. The tube was cleaned with deionized water before sampling to avoid cross-contamination between water samples [38]. Water discharged from the tube was stored in both polyethylene vials of 200 mL and amber glass vials of 20 mL. The former vials were used for the concentration analysis of inorganic nitrogen (NH_4^+ , NO_3^- , and NO_2^-), while the latter vials were used for the DOC determination. All water samples were stored in the cooling box and subsequently taken back to the lab for testing within 24 h. Each water sample was filtered through a 0.45 μm filter membrane before testing.

2.3. Sample Analysis

TN content in each sediment sample was determined using a continuous flow analyzer (QuAAtro 39, Manufacturer: SEAL Co. Ltd., Norderstedt, Germany), while TC content was determined using a total organic carbon analyzer (TOC-VCPN, Manufacturer: Shimadzu Co. Ltd., Kyoto, Japan). Particle size was analyzed using a laser particle size meter (Mastersizer 3000, Manufacturer: Malvern Instrument Co. Ltd., Malvern, UK) with the measurement range of 0.01–3500 μm , after larger grains were removed through sieving. On the basis of the data from particle size analysis, the sediment type was determined. The sediment density (ρ) was quantified by the cutting ring method, and the permeability coefficient (K) was determined through the consolidation test.

For any water sample, NH_4^+ concentration was determined using a continuous flow analyzer (QuAAtro 39, Manufacturer: SEAL Co. Ltd., Norderstedt, Germany) with a quantification limit of 0.02 mg/L, NO_3^- concentration was determined using an ion chromatograph (ICS-90, Manufacturer: DIONEX Co. Ltd., Sunnyvale, CA, USA) with a quantification limit of 0.02 mg/L, NO_2^- concentration was determined using a spectrophotometer (U-3010, Manufacturer: HITACHI Co. Ltd., Tokyo, Japan) with a quantification limit of 0.002 mg/L, and DOC concentration was determined using a total organic carbon analyzer (TOC-VCPN, Manufacturer: Shimadzu Co. Ltd., Kyoto, Japan).

2.4. Determination of Periodicity and Response Time of Water-Level Fluctuation

2.4.1. Periodicity

The frequency analysis of the river stage and the riparian groundwater level was carried out using the fast Fourier transform algorithm (FFT) in MATLAB. FFT is applied to transform signals from time domain to frequency domain for quickly analyzing the frequency characteristics of stationary or nonstationary signals. FFT is an optimization algorithm of discrete Fourier transform (DFT). The DFT value $X(k)$ can be defined as follows [39]:

$$X(k) = \sum_{n=0}^{N-1} x(n)W_N^{nk}, \quad (k = 0, 1, 2, \dots, N-1), \quad (1)$$

where $x(n)$ is the value in the n -th place of a sampled timeseries, N is the length of the series, W_N is the rotation factor equal to $\exp(-j2\pi/N)$, and j is the imaginary unit, $j^2 = -1$.

Through the DFT mentioned above, spectrum values can be calculated, and the spectrum sequence can be obtained. In order to optimize the calculation efficiency, a sampled timeseries with the length of N is usually divided into two subsequences with the length of $N/2$ according to the symmetry and periodicity of W_N . As a result, a pair of DFT units can reduce the computation amount from N^2 to $N \log_2 N$, which is the reason why FFT is performed quickly. After the FFT calculation, the spectrum diagram can be plotted with signal frequency as the horizontal axis and amplitude $X(k)$ as the vertical axis. The dominant oscillation frequency of the river stage or the groundwater level corresponded to the maximum spectrum value in the diagram; accordingly, the dominant period could be determined.

2.4.2. Delayed Response Time and Correlation

The response of the groundwater level to the rise and fall of the river stage was analyzed using the cross-correlation analysis method. Through cross-correlation analysis, the response relationship between the two timeseries could be estimated, and the time shift could be quantified. For two discrete timeseries signals $Y_1(m)$ and $Y_2(m)$, their cross-correlation function $R(\tau)$ is expressed in Equation (2) [40].

$$R(\tau) = \sum_{m=0}^M Y_1(m) \cdot Y_2(m + \tau), \quad (2)$$

where m is the moment, M is the length of the timeseries, τ is the delayed time, and $Y_1(m)$ and $Y_2(m)$ are the timeseries of the river water level and the groundwater level, respectively. A larger $R(\tau)$ value indicates a greater correlation between the two sequences. If $Y_1(m)$ is equal to $Y_2(m)$, then $R(\tau)$ represents the self-correlation function value of the two sequences at τ . Normalization is usually performed on $R(\tau)$, so that the self-correlation is equal to one at the delayed time of zero. The delayed response time of groundwater level to the rise and fall of the river stage corresponded to the maximum $R(\tau)$.

2.5. Statistical Analysis of Water Quality Parameters Data

The seven water quality parameters (NH_4^+ , NO_3^- , NO_2^- , DO, DOC, pH, and temperature) were analyzed using analysis of variance (ANOVA) test and Welch's test. Levene's test was employed initially to determine whether the data met the hypothesis of homogeneity of variance. If the result rejected the hypothesis, Welch's test was chosen to analyze the significance of differences in various water quality parameters of the groundwater among different riparian observation wells. Otherwise, the ANOVA test was used. The level of significance was set to $p < 0.05$ for both Welch's test and the ANOVA test.

3. Results

3.1. Variation and Hysteresis of Groundwater Table in the Riparian Hyporheic Zone under Tidal Effect

The river stage fluctuated twice a day and was of irregular semidiurnal characteristics (Figure 3). During the monitoring period, the mean tidal duration was about 12.2 h. The maximum level was 1.196 m a.s.l., and the minimum level was 0.850 m a.s.l., which contributed to a fluctuation range of 34.6 cm.

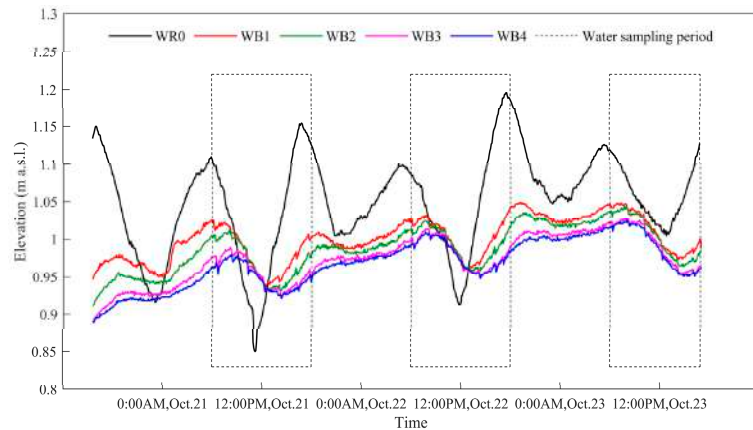


Figure 3. Fluctuation curve of water level in the river channel (WR0) and the four riparian observation wells (WB1–WB4) during the monitoring period from 21 to 23 October 2021.

The groundwater level in any riparian well fluctuated twice a day, just like the river water stage (Figure 3). Regardless of the river channel or the riparian wells, the dominant oscillation period of the water level time series was 12.2 h. The fluctuation range of the water

level gradually decreased upon increasing the distance from the shore on any monitoring day, as shown in Table 1. Over the 3 day study period, the fluctuation range of the daily mean river stage declined from 22.7 to 12.9 cm, while that of the daily mean groundwater level in each riparian well changed a little. Furthermore, the groundwater level in the riparian hyporheic zone exhibited a slow response to the rise and fall movement of the river stage. The delayed response time extended from 90 to 180 min, and the correlation coefficient decreased from 0.75 to 0.52, when the distance increased from 0.71 to 3.85 m away from the shore.

Table 1. Fluctuations and the response relationship of the river stage and the groundwater level during the monitoring period from 21 to 23 October 2021.

Observation Well	Mean Water Level Fluctuation Range (cm)			Time Period (h)	Response to the River Stage	
	21 October	22 October	23 October		Delayed Time (min)	Correlation Coefficient
WR0	22.7	17.9	12.9	12.2	—	—
WB1	6.4	5.8	5.2	12.2	90	0.75
WB2	5.6	4.9	5.2	12.2	135	0.66
WB3	4.3	4.0	4.4	12.2	175	0.56
WB4	3.7	3.5	4.3	12.2	180	0.52

During most of the monitoring period, the river stage was higher than the groundwater level and, hence, the river water continued to penetrate into the riparian hyporheic zone under such a hydraulic gradient. As a result, the groundwater level showed an overall upward trend (Figure 3). The daily mean groundwater levels in different riparian wells showed upward trends with the increase of 3.1–3.9 cm over the monitoring period (Figure 4a). Since the temperature of the river water was lower than that of the groundwater during the study period, the infiltration of the river water to the groundwater contributed to the drop in groundwater temperature. Although the river water temperature increased, the groundwater temperature in the riparian hyporheic zone declined (Figure 4b). Moreover, the decline range had a negative correlation with the distance from the shore. In view of the variations in water level and temperature of the groundwater at WB4, the migration range of water moisture and heat in the riparian hyporheic zone could reach 4 m away from the shore during the study period.

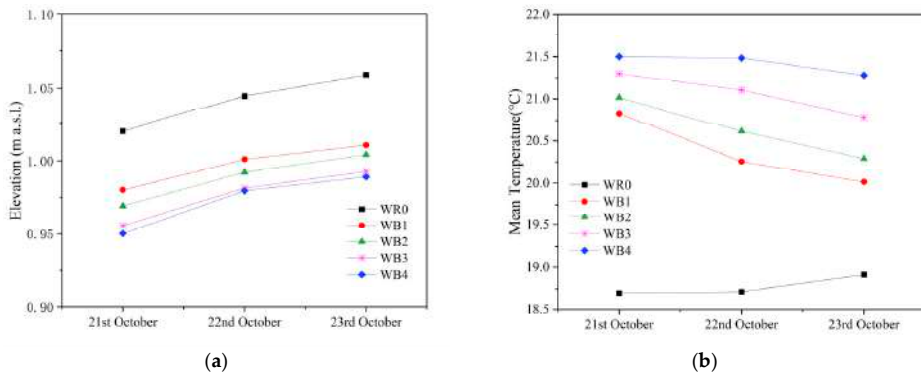


Figure 4. Variations in (a) daily mean water level and (b) daily mean temperature of the river water and the groundwater over the monitoring period from 21 to 23 October 2021.

3.2. Spatial Distribution of Inorganic Nitrogen in the Riparian Hyporheic Zone

According to the statistical analysis, the concentration of three species of inorganic nitrogen (NH_4^+ , NO_3^- , and NO_2^-) in the groundwater showed significant differences among

different riparian wells ($p < 0.001$). The mean NH_4^+ concentration was 0.540 mg/L in the river channel, while those in the riparian observation wells ranged from 0.085 to 0.247 mg/L. This indicated that the NH_4^+ concentration in the river water was higher than that in the riparian groundwater (Figure 5a). The mean NH_4^+ concentrations in the groundwater in WB1, WB2, WB3, and WB4 were 0.085, 0.099, 0.247, and 0.105 mg/L, respectively. It is, thus, clear that the NH_4^+ concentration in the groundwater in the riparian hyporheic zone was lower in the near-shore zone where WB1 and WB2 existed than in the offshore zone where WB3 and WB4 existed.

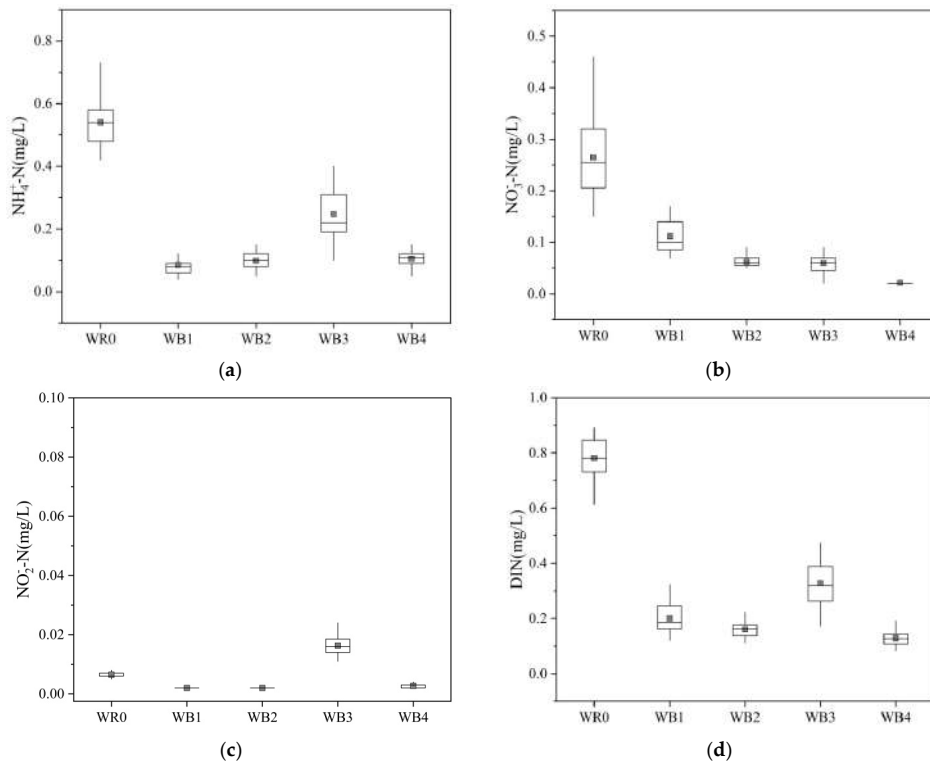


Figure 5. Boxplots of the observed concentrations of inorganic nitrogen in the river water and the riparian groundwater during the study period from 21 to 23 October 2021: (a) ammonia nitrogen, NH_4^+ ; (b) nitrate nitrogen, NO_3^- ; (c) nitrite nitrogen, NO_2^- ; (d) dissolved inorganic nitrogen, DIN.

The mean NO_3^- concentration was 0.265 mg/L in the river water and varied from 0.022 to 0.112 mg/L in the groundwater in the riparian wells (Figure 5b). This implies that the NO_3^- concentration in the river water was higher than that in the groundwater in the riparian hyporheic zone. The mean NO_3^- concentrations in the groundwater were 0.112, 0.062, 0.060, and 0.022 mg/L in WB1, WB2, WB3, and WB4, respectively. The mean NO_3^- concentrations in the riparian groundwater decreased gradually with increasing distance from the shore. The mean NO_2^- concentrations in both the river water and the groundwater in the four wells were below 0.02 mg/L (Figure 5c). This was mainly due to its chemical instability.

Dissolved inorganic nitrogen (DIN) was approximate to the sum of the concentrations of NH_4^+ , NO_3^- , and NO_2^- . The mean DIN concentration was 0.782 mg/L in the river water and varied from 0.129 to 0.327 mg/L in the groundwater in the riparian wells (Figure 5d). The DIN concentration in the river water was higher than that in the riparian

groundwater, and the offshore groundwater had a higher DIN concentration than the near-shore groundwater.

The content of NO_3^- in the groundwater accounted for about 56% of the total DIN content at WB1 on average and decreased with increasing distance from the shore (Figure 6). In contrast, the mean NH_4^+ proportion gradually increased from 43% at WB1 to 81% at WB4. For any riparian well, the mean NO_2^- proportion kept the low value less than 5%.

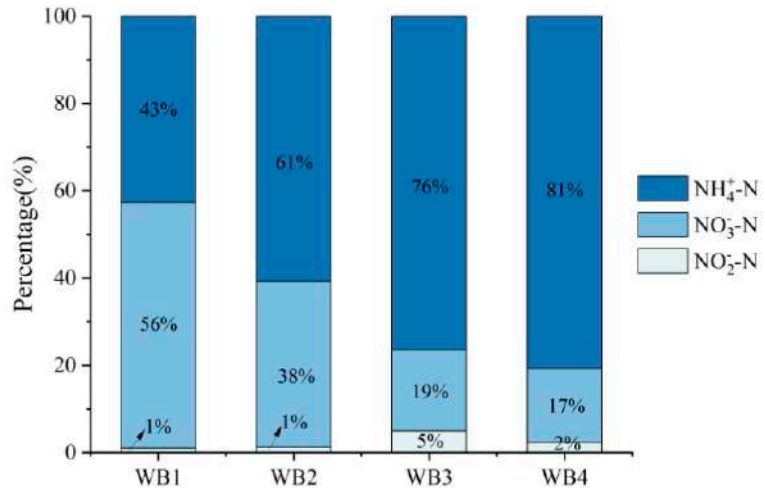


Figure 6. Mean proportions of different forms of inorganic nitrogen in the groundwater in the riparian observation wells during the study period from 21 to 23 October 2021.

3.3. Temporal Variation of Inorganic Nitrogen Concentrations in the Riparian Hyporheic Zone

Over the study period, the daily mean NH_4^+ concentration in the groundwater increased from 0.070 to 0.106 mg/L at WB1 and rose from 0.087 to 0.114 mg/L at WB2 (Figure 7a). In contrast, it decreased from 0.337 to 0.193 mg/L at WB3 and fell from 0.110 to 0.097 mg/L at WB4. It is distinctly clear that the daily mean NH_4^+ concentration showed an upward trend in the near-shore zone and a downward one in the offshore zone.

Meanwhile, the daily mean NO_3^- concentration in the groundwater increased from 0.106 to 0.120 mg/L at WB1 and rose from 0.057 to 0.068 mg/L at WB2 (Figure 7b). However, it changed little in the offshore groundwater. The daily mean NO_2^- concentration in the riparian groundwater showed little change (Figure 7c). This is mainly due to the NO_2^- concentration having a very low concentration in both the river water and the riparian groundwater.

The daily mean DIN concentration increased from 0.178 to 0.228 mg/L at WB1 and ascended from 0.146 to 0.185 mg/L at WB2 (Figure 7d). It decreased from 0.408 to 0.271 mg/L at WB3 and fell from 0.132 to 0.123 mg/L at WB4. It is clear that the variation of the DIN concentration was roughly the same as that of the NH_4^+ concentration in the groundwater; hence, NH_4^+ was generally the dominant form of inorganic nitrogen in the riparian hyporheic zone within 4 m from the shore.

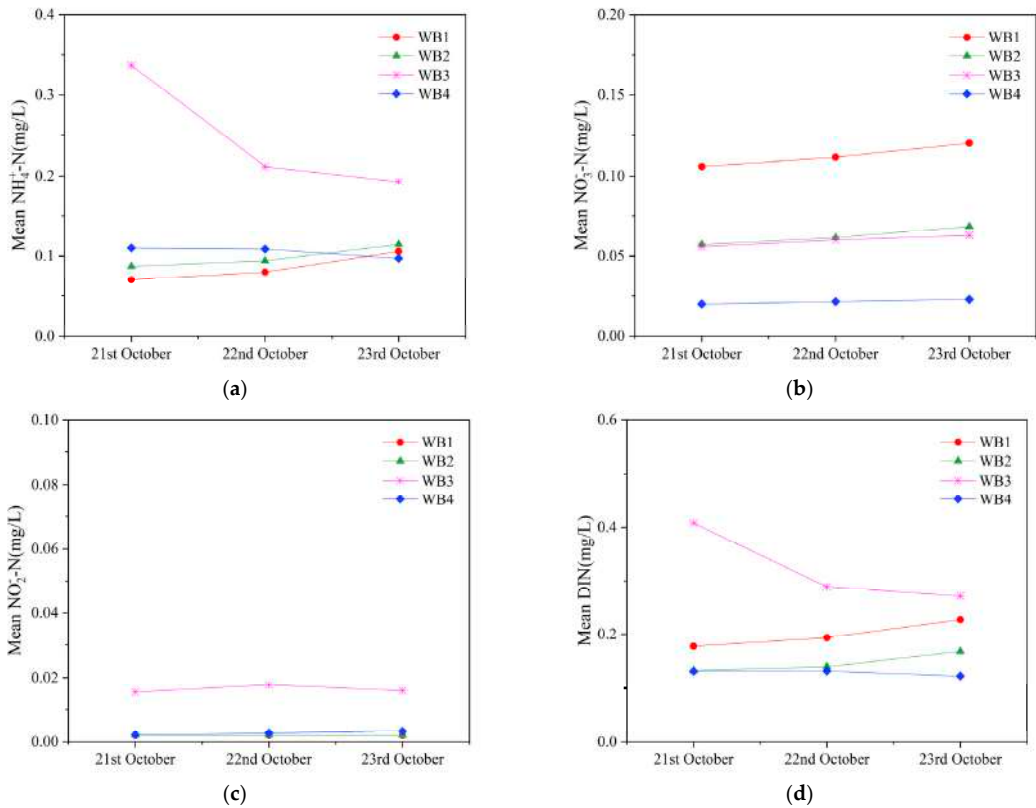


Figure 7. Variations in daily mean inorganic nitrogen concentrations in the river water and the riparian groundwater over the study period from 21 to 23 October 2021: (a) ammonia nitrogen, NH_4^+ ; (b) nitrate nitrogen, NO_3^- ; (c) nitrite nitrogen, NO_2^- ; (d) dissolved inorganic nitrogen, DIN.

3.4. Physicochemical Characteristics of Sediment and Water in the River Channel and the Riparian Hyporheic Zone

There was a great difference between the horizontal and vertical permeability coefficients of the sediment in the riparian hyporheic zone (Table 2). For the sediment at any specific position, the horizontal permeability coefficient was 10 times higher than the vertical one, which implied that the lateral migrations of both the hyporheic flow and the solutes were dominant along the transect. According to the grain size distribution, the riparian sediment was determined as silty-clay soil.

Table 2. Physical properties of the sediment in the riparian hyporheic zone.

Observation Well	Density (g/cm^3)	Coefficient of Permeability (cm/s)				Granularity Content (%)		Soil Type
		Horizontal		Vertical		Clay ($d < 0.005 \text{ mm}$)	Silt ($0.005 \text{ mm} \leq d \leq 0.075 \text{ mm}$)	
		Average	Standard Deviation	Average	Standard Deviation			
WB1	1.89–1.97	4.40×10^{-6}	6.26×10^{-7}	8.71×10^{-8}	0.98×10^{-9}	27–31	53–57	Silty-clay
WB2	1.92–1.97	4.19×10^{-6}	5.78×10^{-7}	9.14×10^{-8}	0.67×10^{-9}	32–34	54–58	Silty-clay
WB3	1.97–1.99	3.11×10^{-6}	8.37×10^{-7}	8.13×10^{-8}	1.05×10^{-8}	34–41	53–59	Silty-clay
WB4	1.94–1.96	3.97×10^{-6}	2.42×10^{-7}	8.44×10^{-8}	1.13×10^{-8}	32–35	55–57	Silty-clay

Both the TN and the TC contents of the sediments gradually increased with depth, and the low contents of TN and TC appeared within the extent (0.9–1.05 m a.s.l.) where the riparian groundwater fluctuated (Figure 8). This could provide a clue that the extent where the groundwater level varied might be the hotspot of biogeochemical reactions in the riparian hyporheic zone, since large amounts of organic mass such as organic nitrogen and organic carbon were consumed in the course of the reactions involving micro-organisms. Furthermore, the mean TN content of the sediment at WB3 was the highest at 674 mg/kg, compared with that at the three other riparian wells.

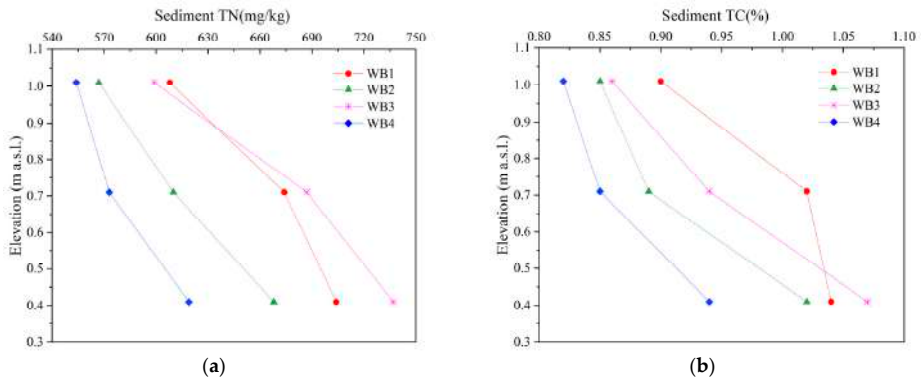


Figure 8. Vertical distribution of the nitrogen and carbon contents of the riparian sediments: (a) total nitrogen, TN; (b) total carbon, TC.

The DO concentration in the groundwater showed a significant difference among different riparian wells ($p < 0.05$). The mean DO concentration in the river water was 6.24 mg/L, higher than that in the riparian groundwater (Figure 9a). Moreover, the mean DO concentration in the riparian groundwater decreased gradually with an increase in distance from the shore. The DO concentration of the riparian groundwater ranged from 5.2 to 6.8 mg/L. The difference of the DOC concentration in the groundwater was not significant among the riparian wells ($p > 0.05$). The data distribution range of the DOC concentration in the river water was less than that in the riparian groundwater (Figure 9b). This implies that the river water was not the only source of the DOC in the riparian groundwater.

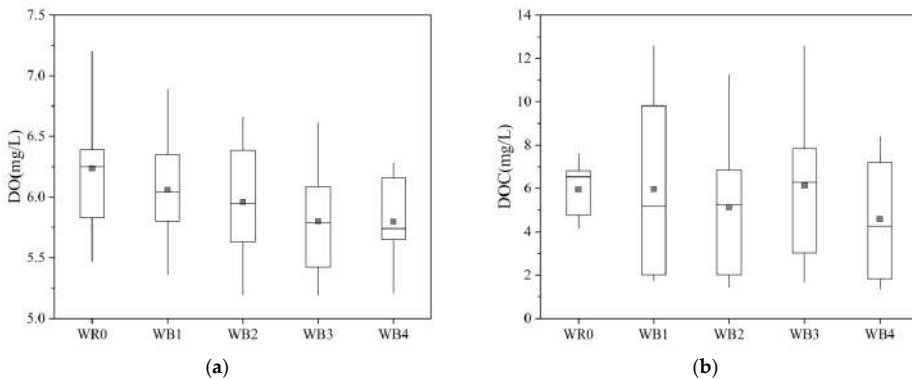


Figure 9. Cont.

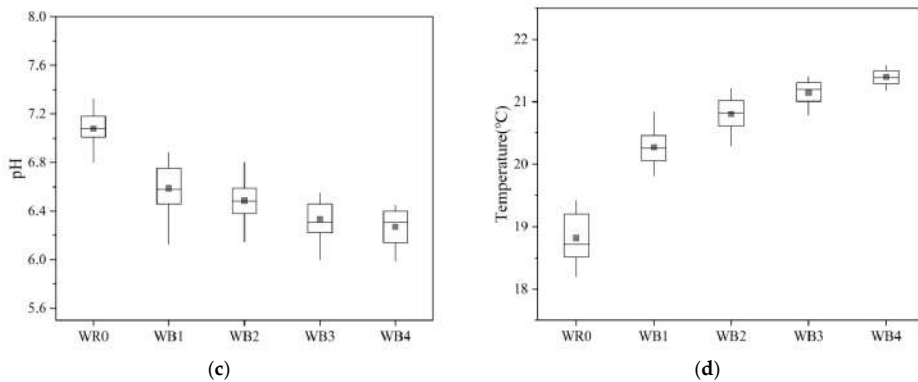


Figure 9. Spatial variations of eco-environmental factors along the transect: (a) dissolved oxygen, DO; (b) dissolved organic carbon, DOC; (c) pH; (d) temperature.

There were significant differences in both the pH and the temperature in the groundwater among different riparian wells ($p < 0.001$). The mean pH of the river water was about 7.08 (Figure 9c), higher than that of the groundwater in any riparian well (ranging from 6.27 to 6.59). Along the transect, the pH decreased with increasing the distance from the shore. The mean temperature of the river water was 18.8 °C, while that of the groundwater in the riparian wells, ranging from 20.3 to 21.4 °C, increased gradually with an increase in distance from the shore (Figure 9d).

4. Discussion

During the study period, the pH and the DO concentrations in the groundwater in the four riparian wells varied from 6.27 to 6.59 (neutral environment) and from 5.2 to 6.8 mg/L, respectively. It is generally considered that an environment is aerobic if DO concentration is greater than 3 mg/L [41]. Thus, the riparian hyporheic zone within 4 m from the bank was an aerobic and neutral environment in favor of nitrification. In past studies, denitrification was regarded as an anaerobic process, and it was considered that denitrification would no longer occur if DO concentration was greater than 4.5 mg/L [42,43]. However, recent research results showed that denitrification could also occur in aerobic zones in soils due to the existence of aerobic denitrifying bacteria which could live in the environment with a DO concentration of 3–9 mg/L and a neutral pH [44–46]. It was, therefore, deduced that aerobic denitrification and nitrification might coexist in the riparian hyporheic zone studied, and the combination of these two effects was conducive to the removal of nitrogen from the riparian zone.

In the investigation, the NH_4^+ concentration in the near-shore groundwater was lower than that in the offshore groundwater, and the lowest value found at WB1 closest to the bank. It was reported by Pan et al. that the NH_4^+ concentration in the riparian groundwater decreased with increasing the distance from the bank of the nitrogen-rich river [47]. This is inconsistent with the results of our research. By comparison, it was found that there were significant differences in NH_4^+ concentration in the river water and type of the sediment. The NH_4^+ concentration in the river water was 0.9–1.5 mg/L, and the sediment mainly consisted of coarse sand in their research, while the former was 0.4–0.7 mg/L and the latter was silty-clay soil in our research. Some studies indicated that a low permeability of the sediment could reduce flow velocity of the pore water and, consequently, prolong the solute residence time, which provided the sufficient reaction time for nitrogen in the hyporheic zone [48,49]. Thus, the lower-permeability sediment and the river water with the lower nitrogen concentration contributed to more consumption and less recharge of the NH_4^+ in the near-shore groundwater, respectively. This could explain why groundwater with less NH_4^+ was observed in the near-shore hyporheic zone. However, upon increasing

the distance from the bank, the DO concentration in the groundwater decreased gradually. The decline in DO concentration could lower the intensity of nitrification [50]. Furthermore, the mean TN content in the sediment at WB3 was highest among the four observation wells. The higher TN content could promote ammoniation, which is an important pathway for recharging the NH_4^+ in the groundwater in hyporheic zones [51,52]. The greater recharge and lower consumption resulted in more NH_4^+ existing in the groundwater in the offshore hyporheic zone.

The NO_3^- concentration in the riparian groundwater showed a downward trend as the distance from the bank increased along the test transect. This matches with the work of Zhang et al. [53]. Due to the strong nitrification reactions and the recharge from the river water, the NO_3^- was enriched in the near-shore groundwater. However, in the offshore hyporheic zone with the poorly permeable sediment, the recharge of NO_3^- from the river water was very slow and could take several hours or even more according to the delayed response time of the groundwater level to the river stage in the study. Moreover, due to the decline in DO concentration, a lower amount of the NO_3^- in the groundwater was produced by nitrification. Additionally, the riparian zone beyond 2 m away from the bank was covered with undisturbed shrubs. According to the research conducted by Stark and Hart, the microbial communities in the soil under undisturbed forest ecosystems had the capacity to assimilate most of the NO_3^- produced by nitrification [54]. Hence, the microbial assimilation of NO_3^- could be considered as a reason for the NO_3^- in the offshore groundwater being lower than that in the near-shore groundwater.

During most of the study period, the river stage remained higher than the riparian groundwater level under tide action, which led to a continuous infiltration of river water into the riverbank. As the river water steadily flowed into the hyporheic zone, the NH_4^+ and NO_3^- in the near-shore groundwater were continuously recharged; thus, the NH_4^+ and NO_3^- concentrations showed overall upward trends in the near-shore zone over the 3 day study period. Accompanied by the seepage process, the riparian groundwater level had an uplift which made part of the oxygen in the upper vadose zone enter the groundwater [55]. Thus, the DO concentration in the riparian groundwater increased due to the lateral recharge from the river, as well as the vertical recharge from the upper soil, which contributed to a whole aerobic environment within 4 m from the bank. The increase in DO concentration in the offshore groundwater promoted nitrification [56]. Meanwhile, the fine particles of the silty clay sediment had strong adsorption capacity, which restricted the further migration of the NH_4^+ in the near-shore groundwater to some extent [57]. For these reasons, the NH_4^+ concentration in the offshore groundwater decreased over the study period. Although the further migration of the NO_3^- in the near-shore groundwater and nitrification could have caused an increase in NO_3^- concentration in the offshore groundwater, little change was actually observed. This might be due to the fact that the microbial assimilation of NO_3^- was considerable in the offshore hyporheic zone under the shrubs.

The variation range of the DOC concentration in the groundwater in each riparian well was significantly larger than that in the river. The DOC in the riparian groundwater mainly depended on the dissolution of particulate organic carbon (POC) in the sediment rather than the infiltration of the river water, which is consistent with the research of Peyrard et al. [58]. Some previous studies reported the effect of DOC, pH, and temperature on the nitrogen cycle in the hyporheic zone. The DOC could play an important role in denitrification processes [59]. The reaction rate of nitrogen could be inhibited in an acidic environment ($\text{pH} < 5.5$), but there is an insignificant impact on nitrogen cycle in a neutral environment [60,61]. The nitrification rate in soils gradually increases with temperature within the range of 15–35 °C [62]. However, in our research, there was an insignificant difference in DOC concentration in the riparian groundwater. Moreover, the pH remained neutral, and the temperature had a small change of 1–2 °C in the riparian hyporheic zone. Hence, DOC concentration, pH, and temperature may not be the dominant factors causing the spatiotemporal difference in inorganic nitrogen concentration in the groundwater in the riparian zone studied.

Additionally, it should be noted that the time period involved in the research was a spring tidal period in October, and recharging the riparian aquifers from the river water was dominant during the period. However, the tide-driven hyporheic exchange process varies with tide strength and season. Since the hyporheic exchange greatly influences the nitrogen occurrence, the findings of the study have to be seen in light of some limitations. Future research will be performed to analyze nitrogen occurrence in groundwater in silty-clay hyporheic zones under the action of tides of different strength and its seasonal variation. Moreover, the variations of nitrogen forms and the influencing factors with depth will need to be investigated to reveal the vertical nitrogen cycle in hyporheic zones of tidal rivers.

5. Conclusions

It was confirmed from the study that the groundwater level in the silty-clay riparian zone presented a slow response to the tide-driven fluctuation of the river stage. The delayed response time reached a few hours within 1–4 m away from the bank, which could help to extend the hydraulic and solute retention time. The continuous infiltration of the river water under tide action contributed to the aerobic and neutral riparian hyporheic zone conducive to nitrification. Within 4 m away from the bank, the dominant inorganic nitrogen form changed from NO_3^- -N to NH_4^+ -N, upon increasing the distance from the bank. In addition, the removal of nitrogen could occur in the riparian hyporheic zone with an aerobic and neutral environment under the joint control of nitrification, microbial assimilation, and aerobic denitrification. It is important to consider that nitrogen occurrence in riparian hyporheic zones of tidal rivers is governed by many factors including tidal strength, permeability and chemical compositions of sediments, DO concentration, vegetation coverage, and even nitrogen concentration in river water.

Author Contributions: Conceptualization, Y.C. and J.X.; methodology, Y.C. and J.X.; software, J.X.; validation, J.X.; formal analysis, Y.C. and J.X.; investigation, Y.C., J.X., N.Z., R.H., X.R. and D.Y.; resources, Y.C. and J.X.; data curation, J.X., R.H. and X.R.; writing—original draft preparation, Y.C. and J.X.; writing—review and editing, Y.C. and N.Z.; funding acquisition, Y.C. and N.Z. All authors have read and agreed to the published version of the manuscript.

Funding: This research was financially supported by the National Natural Science Foundation of China (Grant No. 42077176) and the Natural Science Foundation of Shanghai (Grant No. 20ZR1459700).

Institutional Review Board Statement: Not applicable.

Informed Consent Statement: Not applicable.

Data Availability Statement: Data are contained within the article.

Acknowledgments: The authors specially thank the Shanghai Institute of Geological Survey for providing assistance with sample testing.

Conflicts of Interest: The authors declare no conflict of interest.

References

1. Wang, Y.C.; Lu, Y.L. Evaluating the potential health and economic effects of nitrogen fertilizer application in grain production systems of China. *J. Clean. Prod.* **2020**, *264*, 121635. [[CrossRef](#)]
2. Liang, D.; Song, J.X.; Xia, J.; Chang, J.B.; Kong, F.H.; Sun, H.T.; Wu, Q.; Cheng, D.D.; Zhang, Y.X. Effects of heavy metals and hyporheic exchange on microbial community structure and functions in hyporheic zone. *J. Environ. Manag.* **2022**, *303*, 114201. [[CrossRef](#)] [[PubMed](#)]
3. Ward, A.S. The evolution and state of interdisciplinary hyporheic research. *Wiley Interdiscip. Wiley Interdiscip. Rev. Water* **2016**, *3*, 83–103.
4. Cai, Y.; Shi, T.; Yao, J.L.; Liu, S.G.; Ruan, X.K.; Xu, J. Advance in field monitoring research of hydrodynamic process of hyporheic exchange in rivers. *Adv. Water Sci.* **2021**, *32*, 638–648. (In Chinese)
5. Bernal, S.; Lupon, A.; Ribot, M.; Sabater, F.; Marti, E. Riparian and in-stream controls on nutrient concentrations and fluxes in a headwater forested stream. *Biogeosciences* **2015**, *12*, 1941–1954. [[CrossRef](#)]

6. Lamontagne, S.; Cosme, F.; Minard, A.; Holloway, A. Nitrogen attenuation, dilution and recycling in the intertidal hyporheic zone of a subtropical estuary. *Hydrol. Earth Syst. Sci.* **2018**, *22*, 4083–4096. [[CrossRef](#)]
7. Hampton, T.B.; Zarnetske, J.P.; Briggs, M.A.; Singha, K.; Harvey, J.W.; Day-Lewis, F.D.; Dehkordy, F.M.; Lane, J.W. Residence time controls on the fate of nitrogen in flow-through lakebed sediments. *J. Geophys. Res.-Biogeosci.* **2019**, *124*, 689–707. [[CrossRef](#)]
8. Naranjo, R.C.; Niswonger, R.G.; Davis, C.J. Mixing effects on nitrogen and oxygen concentrations and the relationship to mean residence time in a hyporheic zone of a riffle-pool sequence. *Water Resour. Res.* **2015**, *51*, 7202–7217. [[CrossRef](#)]
9. Zhou, N.Q.; Zhao, S.; Shen, X.P. Nitrogen cycle in the hyporheic zone of natural wetlands. *Chin. Sci. Bull.* **2014**, *59*, 2945–2956. [[CrossRef](#)]
10. Wen, H.; Perdrial, J.; Abbott, B.W.; Bernal, S.; Dupas, R.; Godsey, S.E.; Harpold, A.; Rizzo, D.; Underwood, K.; Adler, T.; et al. Temperature controls production but hydrology regulates export of dissolved organic carbon at the catchment scale. *Hydrol. Earth Syst. Sci.* **2020**, *24*, 945–966. [[CrossRef](#)]
11. Ledesma, J.L.J.; Ruiz-Perez, G.; Lupon, A.; Poblador, S.; Futter, M.N.; Sabater, F.; Bernal, S. Future changes in the Dominant Source Layer of riparian lateral water fluxes in a subhumid Mediterranean catchment. *J. Hydrol.* **2021**, *595*, 126014. [[CrossRef](#)]
12. Newcomer, M.E.; Hubbard, S.S.; Fleckenstein, J.H.; Maier, U.; Schmidt, C.; Thullner, M.; Ulrich, C.; Flipo, N.; Rubin, Y. Influence of hydrological perturbations and riverbed sediment characteristics on hyporheic zone respiration of CO₂ and N₂. *J. Geophys. Res.-Biogeosci.* **2018**, *123*, 902–922. [[CrossRef](#)]
13. Cai, Y.; Xing, J.W.; Ruan, X.K.; Zhong, N.Q.; Huang, R.Y.; Yi, D.Z. Advances in the numerical simulation of the migration and transformation of nitrogen in hyporheic zones of rivers. *Water Resour. Prot.* **2022**. Available online: <http://kns.cnki.net/kcms/detail/32.1356.TV.20220419.1738.004.html> (accessed on 20 April 2022). (In Chinese).
14. Shibata, H.; Sugawara, O.; Toyoshima, H.; Wondzell, S.M.; Nakamura, F.; Kasahara, T.; Swanson, F.J.; Sasa, K. Nitrogen dynamics in the hyporheic zone of a forested stream during a small storm, Hokkaido, Japan. *Biogeochemistry* **2004**, *69*, 83–103. [[CrossRef](#)]
15. Singh, T.; Wu, L.W.; Gomez-Velez, J.D.; Lewandowski, J.; Hannah, D.M.; Krause, S. Dynamic hyporheic zones: Exploring the role of peak flow events on bedform-induced hyporheic exchange. *Water Resour. Res.* **2019**, *55*, 218–235. [[CrossRef](#)]
16. Sawyer, A.H.; Cardenas, M.B.; Bomar, A.; Mackey, M. Impact of dam operations on hyporheic exchange in the riparian zone of a regulated river. *Hydrol. Process* **2009**, *23*, 2129–2137. [[CrossRef](#)]
17. Bernhardt, E.S.; Blaszczak, J.R.; Ficken, C.D.; Fork, M.L.; Kaiser, K.E.; Seybold, E.C. Control points in ecosystems: Moving beyond the hot Spot hot moment concept. *Ecosystems* **2017**, *20*, 665–682. [[CrossRef](#)]
18. Musial, C.T.; Sawyer, A.H.; Barnes, R.T.; Bray, S.; Knights, D. Surface water-groundwater exchange dynamics in a tidal freshwater zone. *Hydrol. Process* **2016**, *30*, 739–750. [[CrossRef](#)]
19. Barnes, R.T.; Sawyer, A.H.; Tight, D.M.; Wallace, C.D.; Hastings, M.G. Hydrogeologic controls of surface water-groundwater nitrogen dynamics within a tidal freshwater zone. *J. Geophys. Res.-Biogeosci.* **2019**, *124*, 3343–3355. [[CrossRef](#)]
20. Wallace, C.D.; Sawyer, A.H.; Soltanian, M.R.; Barnes, R.T. Nitrate removal within heterogeneous riparian aquifers under tidal influence. *Geophys. Res. Lett.* **2020**, *47*, e2019GL085699. [[CrossRef](#)]
21. Wallace, C.D.; Sawyer, A.H.; Barnes, R.T.; Soltanian, M.R.; Gabor, R.S.; Wilkins, M.J.; Moore, M.T. A model analysis of the tidal engine that drives nitrogen cycling in coastal riparian aquifers. *Water Resour. Res.* **2020**, *56*, e2019WR025662. [[CrossRef](#)]
22. Pryshlak, T.T.; Sawyer, A.H.; Stonedahl, S.H.; Soltanian, M.R. Multiscale hyporheic exchange through strongly heterogeneous sediments. *Water Resour. Res.* **2015**, *51*, 9127–9140. [[CrossRef](#)]
23. McGarr, J.T.; Wallace, C.D.; Ntarlagiannis, D.; Sturmer, D.M.; Soltanian, M.R. Geophysical mapping of hyporheic processes controlled by sedimentary architecture within compound bar deposits. *Hydrol. Process* **2021**, *35*, e14358. [[CrossRef](#)]
24. Briggs, M.A.; Day-Lewis, F.D.; Zarnetske, J.P.; Harvey, J.W. A physical explanation for the development of redox microzones in hyporheic flow. *Geophys. Res. Lett.* **2015**, *42*, 4402–4410. [[CrossRef](#)]
25. Krause, S.; Tecklenburg, C.; Munz, M.; Naden, E. Streambed nitrogen cycling beyond the hyporheic zone: Flow controls on horizontal patterns and depth distribution of nitrate and dissolved oxygen in the upwelling groundwater of a lowland river. *J. Geophys. Res.-Biogeosci.* **2013**, *118*, 54–67. [[CrossRef](#)]
26. Zhao, L.; Li, Y.L.; Wang, S.D.; Wang, X.Y.; Meng, H.Q.; Luo, S.H. Adsorption and transformation of ammonium ion in a loose-pore geothermal reservoir: Batch and column experiments. *J. Contam. Hydrol.* **2016**, *192*, 50–59. [[CrossRef](#)] [[PubMed](#)]
27. Shan, J.; Yang, P.P.; Shang, X.X.; Rahman, M.M.; Yan, X.Y. Anaerobic ammonium oxidation and denitrification in a paddy soil as affected by temperature, pH, organic carbon, and substrates. *Biol. Fertil. Soils* **2018**, *54*, 341–348. [[CrossRef](#)]
28. Bai, B.; Jiang, S.C.; Liu, L.L.; Li, X.; Wu, H.Y. The transport of silica powders and lead ions under unsteady flow and variable injection concentrations. *Powder Technol.* **2021**, *387*, 22–30. [[CrossRef](#)]
29. Helton, A.M.; Ardon, M.; Bernhardt, E.S. Thermodynamic constraints on the utility of ecological stoichiometry for explaining global biogeochemical patterns. *Ecol. Lett.* **2015**, *18*, 1049–1056. [[CrossRef](#)]
30. Pescimoro, E.; Boano, F.; Sawyer, A.H.; Soltanian, M.R. Modeling influence of sediment heterogeneity on nutrient cycling in streambeds. *Water Resour. Res.* **2019**, *55*, 4082–4095. [[CrossRef](#)]
31. Zarnetske, J.P.; Haggerty, R.; Wondzell, S.M.; Baker, M.A. Labile dissolved organic carbon supply limits hyporheic denitrification. *J. Geophys. Res.-Biogeosci.* **2011**, *116*, G04036. [[CrossRef](#)]
32. Zarnetske, J.P.; Haggerty, R.; Wondzell, S.M.; Baker, M.A. Dynamics of nitrate production and removal as a function of residence time in the hyporheic zone. *J. Geophys. Res.-Biogeosci.* **2011**, *116*, G01025. [[CrossRef](#)]

33. Herrman, K.S.; Bouchard, V.; Moore, R.H. Factors affecting denitrification in agricultural headwater streams in Northeast Ohio, USA. *Hydrobiologia* **2008**, *598*, 305–314. [[CrossRef](#)]
34. Bai, B.; Nie, Q.K.; Zhang, Y.K.; Wang, X.L.; Hu, W. Cotransport of heavy metals and SiO₂ particles at different temperatures by seepage. *J. Hydrol.* **2021**, *597*, 125771. [[CrossRef](#)]
35. Zhao, S.; Zhou, N.Q.; Shen, X.P. Driving mechanisms of nitrogen transport and transformation in lacustrine wetlands. *Sci. China-Earth Sci.* **2016**, *59*, 464–476. [[CrossRef](#)]
36. Zong, H.C.; Zhang, W.S.; Zhang, J.S. Study on influence of sea level rise on storm tidal levels of Huangpu River. *Yangtze River* **2014**, *45*, 1–3. (In Chinese)
37. Huang, X.Y. Hydrological characteristics of Shanghai area. *J. China Hydrol.* **1987**, *32*, 43–46. (In Chinese)
38. Harvey, J.W.; Bohlke, J.K.; Voytek, M.A.; Scott, D.; Tobias, C.R. Hyporheic zone denitrification: Controls on effective reaction depth and contribution to whole-stream mass balance. *Water Resour. Res.* **2013**, *49*, 6298–6316. [[CrossRef](#)]
39. Marcotte, D. Fast variogram computation with FFT. *Comput. Geosci.* **1996**, *22*, 1175–1186. [[CrossRef](#)]
40. Qian, W.M.; Liang, H.Y.; Yang, G.Q. *Applied Stochastic Processes*, 1st ed.; Higher Education Press: Beijing, China, 2014; pp. 101–109. (In Chinese)
41. Anderson, T.H.; Taylor, G.T. Nutrient pulses, plankton blooms, and seasonal hypoxia in western Long Island Sound. *Estuaries* **2001**, *24*, 228–243. [[CrossRef](#)]
42. Xue, D.M.; Botte, J.; De Baets, B.; Accoe, F.; Nestler, A.; Taylor, P.; Van Cleemput, O.; Berglund, M.; Boeckx, P. Present limitations and future prospects of stable isotope methods for nitrate source identification in surface- and groundwater. *Water Res.* **2009**, *43*, 1159–1170. [[CrossRef](#)]
43. Patureau, D.; Bernet, N.; Delgenes, J.P.; Moletta, R. Effect of dissolved oxygen and carbon-nitrogen loads on denitrification by an aerobic consortium. *Appl. Microbiol. Biotechnol.* **2000**, *54*, 535–542. [[CrossRef](#)] [[PubMed](#)]
44. Huang, T.L.; Zhou, S.L.; Zhang, H.H.; Bai, S.Y.; He, X.X.; Yang, X. Nitrogen removal characteristics of a newly isolated indigenous aerobic denitrifier from oligotrophic drinking water reservoir, Zoogloeasp N299. *Int. J. Mol. Sci.* **2015**, *16*, 10038–10060. [[CrossRef](#)] [[PubMed](#)]
45. Kim, M.; Jeong, S.Y.; Yoon, S.J.; Cho, S.J.; Kim, Y.H.; Kim, M.J.; Ryu, E.Y.; Lee, S.J. Aerobic denitrification of pseudomonas putida AD-21 at different C/N ratios. *J. Biosci. Bioeng.* **2008**, *106*, 498–502. [[CrossRef](#)] [[PubMed](#)]
46. Hu, J.A.; Yang, X.Y.; Deng, X.Y.; Liu, X.M.; Yu, J.X.; Chi, R.; Xiao, C.Q. Isolation and nitrogen removal efficiency of the heterotrophic nitrifying-aerobic denitrifying strain K17 from a rare earth element leaching site. *Front. Microbiol.* **2022**, *13*, 905409. [[CrossRef](#)]
47. Pan, J.; Li, R.F.; Meng, X.T.; Ye, M.X. Biogeochemical characteristics of nitrogen migration and transformation in subsurface flow belt driven by river collection. *Environ. Eng.* **2021**, *39*, 62–68. (In Chinese)
48. Yabusaki, S.B.; Wilkins, M.J.; Fang, Y.L.; Williams, K.H.; Arora, B.; Bargar, J.; Beller, H.R.; Bouskill, N.J.; Brodie, E.L.; Christensen, J.N.; et al. Water table dynamics and biogeochemical cycling in a shallow, variably-saturated floodplain. *Environ. Sci. Technol.* **2017**, *51*, 3307–3317. [[CrossRef](#)]
49. Krause, S.; Blume, T.; Cassidy, N.J. Investigating patterns and controls of groundwater up-welling in a lowland river by combining Fibre-optic Distributed Temperature Sensing with observations of vertical hydraulic gradients. *Hydrol. Earth Syst. Sci.* **2012**, *16*, 1775–1792. [[CrossRef](#)]
50. Zarnetske, J.P.; Haggerty, R.; Wondzell, S.M.; Bokil, V.A.; Gonzalez-Pinzon, R. Coupled transport and reaction kinetics control the nitrate source-sink function of hyporheic zones. *Water Resour. Res.* **2012**, *48*, W11508.
51. Marumoto, T.; Anderson, J.P.E.; Domsch, K.H. Decomposition of ¹⁴C- and ¹⁵N-labelled microbial cells in soil. *Soil Biol. Biochem.* **1982**, *14*, 461–467. [[CrossRef](#)]
52. Weatherill, J.J.; Krause, S.; Ullah, S.; Cassidy, N.J.; Levy, A.; Drijfhout, F.P.; Rivett, M.O. Revealing chlorinated ethene transformation hotspots in a nitrate-impacted hyporheic zone. *Water Res.* **2019**, *161*, 222–231. [[CrossRef](#)]
53. Zhang, Y.; Yang, P.H.; Wang, J.L.; Xie, S.Y.; Chen, F.; Zhan, Z.J.; Ren, J.; Zhang, H.Y.; Liu, D.W.; Meng, Y.K. Geochemical characteristics of lateral hyporheic zone between the river water and groundwater, a case study of Maanxi in Chongqing. *Environ. Sci.* **2016**, *37*, 2478–2486. (In Chinese)
54. Stark, J.M.; Hart, S.C. High rates of nitrification and nitrate turn-over in undisturbed coniferous forests. *Nature* **1997**, *385*, 61–64. [[CrossRef](#)]
55. Williams, M.D.; Ostrom, M. Oxygenation of anoxic water in a fluctuating water table system: An experimental and numerical study. *J. Hydrol.* **2000**, *230*, 70–85. [[CrossRef](#)]
56. Covatti, G.; Grischek, T. Sources and behavior of ammonium during riverbank filtration. *Water Res.* **2021**, *191*, 116788. [[CrossRef](#)]
57. Wu, F.; Wang, Y.; Yan, X.; Xia, C.; Xiao, Y.; Huo, J.; Zhou, X. Adsorption characteristics of suspended sediment to ammonia nitrogen in Lanzhou section of the Yellow River. *China J. Environ. Eng.* **2014**, *8*, 3201–3207.
58. Peyrard, D.; Delmotte, S.; Sauvage, S.; Namour, P.; Gerino, M.; Vervier, P.; Sanchez-Perez, J.M. Longitudinal transformation of nitrogen and carbon in the hyporheic zone of an N-rich stream: A combined modelling and field study. *Phys. Chem. Earth* **2011**, *36*, 599–611. [[CrossRef](#)]

59. Bohlke, J.K.; Antweiler, R.C.; Harvey, J.W.; Laursen, A.E.; Smith, L.K.; Smith, R.L.; Voytek, M.A. Multi-scale measurements and modeling of denitrification in streams with varying flow and nitrate concentration in the upper Mississippi River basin, USA. *Biogeochemistry* **2009**, *93*, 117–141. [[CrossRef](#)]
60. Lehtovirta-Morley, L.E.; Stoecker, K.; Vilcinskas, A.; Prosser, J.I.; Nicol, G.W. Cultivation of an obligate acidophilic ammonia oxidizer from a nitrifying acid soil. *Proc. Natl. Acad. Sci. USA* **2011**, *108*, 15892–15897. [[CrossRef](#)]
61. Kemmitt, S.J.; Wright, D.; Goulding, K.W.T.; Jones, D.L. pH regulation of carbon and nitrogen dynamics in two agricultural soils. *Soil Biol. Biochem.* **2006**, *38*, 898–911. [[CrossRef](#)]
62. Hu, R.; Wang, X.P.; Pan, Y.X.; Zhang, Y.F.; Zhang, H. The response mechanisms of soil N mineralization under biological soil crusts to temperature and moisture in temperate desert regions. *Eur. J. Soil Biol.* **2014**, *62*, 66–73. [[CrossRef](#)]

Article

Screening Additives for Amending Compacted Clay Covers to Enhance Diffusion Barrier Properties and Moisture Retention Performance

Min Wang ¹, Jiaming Wen ², Heng Zhuang ¹, Weiyi Xia ³, Ningjun Jiang ¹ and Yanjun Du ^{1,*}¹ Jiangsu Key Laboratory of Urban Underground Engineering & Environmental Safety,

Institute of Geotechnical Engineering, Southeast University, Nanjing 210096, China;

wang-min@seu.edu.cn (M.W.); zhuangheng@seu.edu.cn (H.Z.); jiangn@seu.edu.cn (N.J.)

² Zijin (Changsha) Engineering Technology Co., Ltd., Changsha 410006, China; wenjiaming@seu.edu.cn³ Jiangsu Environmental Engineering Technology Co., Ltd., Nanjing 210019, China; xiaweiyi@seu.edu.cn

* Correspondence: duyanjun@seu.edu.cn

Featured Application: The dual-additives-amended compacted clay covers in this article could apply to the cover system of industrial contaminated sites, municipal solid waste landfill, and industrial solid waste landfill. The dual-additives could enhance the anti-cracking, moisture retention, gas barrier, and hydraulic performance of compacted clay covers.

Abstract: The cover systems in contaminated sites have some problems, including desiccation cracks, which would lead to degradation of the barrier performance. This study presented a systemic laboratory experimental investigation on the liquid–plastic limit, moisture retention, hydraulic conductivity (k), and gas diffusion barrier properties of amended compacted clay by attapulgite and diatomite for controlling desiccation cracks and migration of water and volatile organic compounds (VOCs). The results showed that the attapulgite could enhance the moisture retention and liquid limit of amended compacted clay. Diatomite could reduce the gas diffusion coefficient (D_{θ}) significantly. The compacted clay amended by the dual-additives component of attapulgite and diatomite could enhance the liquid limit, moisture retention percent, gas barrier property, and hydraulic performance compared with the unamended clay. Based on the experimental data obtained, the dosage of additives was targeted to be 5%. The moisture retention percent of dual-additives (attapulgite 4% and diatomite 1%) amended clay increased by 82%, the k decreased by 25%, and the D_{θ} decreased by 42% compared with unamended clay. Scanning electron microscopy (SEM), BET-specific surface area test method (BET), Mercury Intrusion Porosimetry (MIP), and thermogravimetric analysis (TGA) indicated the enhancement mechanism of additives-amended compacted clay.

Keywords: additives; compacted clay cover; moisture retention; gas diffusion barrier; hydraulic conductivity

Citation: Wang, M.; Wen, J.; Zhuang, H.; Xia, W.; Jiang, N.; Du, Y.

Screening Additives for Amending Compacted Clay Covers to Enhance Diffusion Barrier Properties and Moisture Retention Performance. *Appl. Sci.* **2022**, *12*, 7341. <https://doi.org/10.3390/app12147341>

Academic Editor: Bing Bai

Received: 9 June 2022

Accepted: 18 July 2022

Published: 21 July 2022

Publisher's Note: MDPI stays neutral with regard to jurisdictional claims in published maps and institutional affiliations.



Copyright: © 2022 by the authors. Licensee MDPI, Basel, Switzerland. This article is an open access article distributed under the terms and conditions of the Creative Commons Attribution (CC BY) license (<https://creativecommons.org/licenses/by/4.0/>).

1. Introduction

The cover system, including compacted clay cover (CCC) and geomembrane (GM), applied in contaminated sites could prevent the migration of volatile or semi-volatile organic compounds (VOCs/SVOCs) and limit the movement of precipitation into the underlying waste [1–5]. However, the published literature [6–8] have shown that the cover system has some problems, including geomembrane defects, and desiccation cracks of the CCC, which would lead to the degradation of the barrier performance (Figure 1). Rowe et al. [6] presented that the geomembrane defects are inevitable. The monitoring results of 205 sites show that the percent of complete geomembrane is less than 30%. In addition, more than 50 percent of geomembranes have more than five loopholes per ha. The barrier performance of the cover system would be degraded by geomembrane defects. Then,

the CCC contributes to the role of VOCs/SVOCs and the precipitation barrier. However, desiccation cracks in CCC act as preferential flow paths and affect the barrier performance of CCC, eventually breaking through the cover system [9]. There are various issues resulting in cracks of CCC [7,10], including differential settlements, extreme drought [11], and dry-wet cycle [9]. The resistance to cracking, i.e., the tensile strength or fracture toughness of the soil, also changes upon drying. Finally, the adhesion at interfaces, which is essential in providing the restraint for desiccation cracks to form, changes with moisture content [12,13]. Omid et al. [8] showed that the hydraulic conductivity increases nearly two orders of magnitude due to the desiccation cracks of CCC, which would have a great impact on the cover system. Albrecht and Benson [14] presented that the hydraulic conductivity of cracked soils is typically several orders of magnitude greater than that of intact soils.

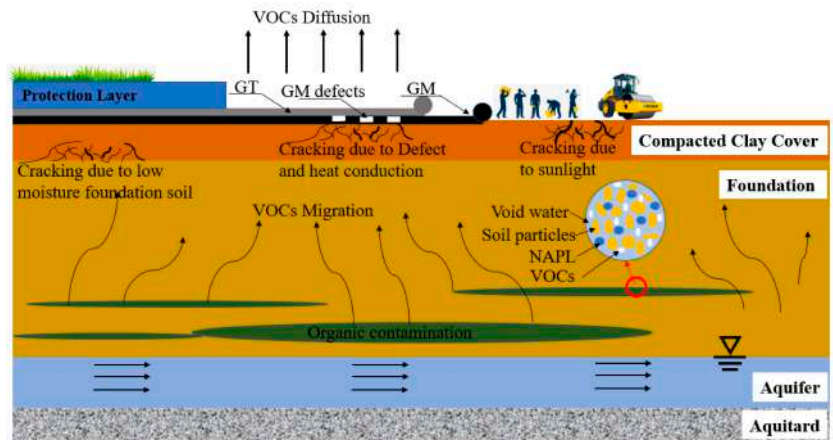


Figure 1. Problems of compacted clay cover desiccation and possible migration of VOCs [6–14].

To restrain the desiccation cracks of CCC, moisture retention additives were added to the soil to improve its moisture retention and desiccation cracks inhibition performance. Moisture retention additives could inhibit moisture evaporation and regulate soil temperature by adsorbing water hundreds or even thousands of times its weight [15]. According to different synthetic materials, the moisture retention additives can be divided into four kinds: modified starch, synthetic polymer, modified cellulose, and other natural compounds and their derivatives, blends, and composites [16]. It is cumbersome to prepare the synthetic polymer moisture retention additives. In addition, it is not suitable for practical engineering because the synthetic polymer would be completely degraded in soil within some years [17]. Therefore, natural materials and their derivatives could be selected as amended materials, namely attapulgite, diatomite, and zeolite. However, the natural zeolite cannot meet the requirements due to its small pore size and being easy to block [18]. Finally, attapulgite and diatomite are proposed as additives for amending CCC.

Usually, the migration modes of gases in the soil included advection and diffusion [5]. Conant et al. [19] found that diffusion is the main migration mode of trichloroethylene (TCE) vapor through a detailed, field-scale analysis of the transport behavior of solvent vapors within the unsaturated zone. The unsaturated zone at the site is approximately 3.5 m thick and comprises the upper portion of the sequence of glaciolacustrine sands and silts of the Borden aquifer. You et al. [20] found that although the transient advective flux can be greater than the diffusive flux; under most of the field conditions the net contribution of the advective flux is one to three orders of magnitude less than the diffusive flux. The advective flux contributes comparably with the diffusive flux only when the gas-filled porosity is less than 0.05. The advective transport of VOCs can be induced by the discrepancy in density between gas phase VOCs and clean air [21–23], water table fluctuation at

coastal sites [21,23–25], and atmospheric pressure fluctuation [26,27]. Therefore, in most non-coastal sites and unsaturated zones with low permeability, the VOCs' migration mode in the organic contaminated sites is mainly diffusion [28–30]. Rowe [31] found that the gas barrier should not only prevent water migration, but also the organic contaminants transmission. Therefore, the development of amended CCC with excellent moisture retention and VOCs/SVOCs diffusion barrier performance is significant.

A systematic study of the moisture retention, hydraulic conductivity, and gas barrier properties of amended CCC was investigated through laboratory experiments. In this paper, the optimal dosage and ratio of dual-additives of the amended CCC were studied through the laboratory test. The hydraulic conductivity and gas barrier properties of amended CCC with optimal dosage and ratio were evaluated. Then, the mechanism behind the phenomenon was demonstrated through SEM, BET, MIP, and TGA test analyses.

2. Materials and Methods

2.1. Preparation of Amended Compacted Clay

Three types of amended compacted clay were prepared in this study: (1) the compacted clay amended by attapulgite with the dosage of 0%, 1%, 3%, 5%, and 10% (dry weight of attapulgite to dry weight of mixture powder); (2) the compacted clay amended by diatomite with the dosage of 0%, 1%, 3%, 5%, and 10% (dry weight of attapulgite to dry weight of mixture powder); and (3) the compacted clay amended by attapulgite and diatomite, here referred to as dual-additives, with the ratio of 4, 2, 1, 0.5, and 0.25 (dry weight of attapulgite to dry weight of diatomite); the dosage of dual-additives was attapulgite 4% and diatomite 1%, attapulgite 3.3% and diatomite 1.7%, attapulgite 2.5% and diatomite 2.5%, attapulgite 1.7% and diatomite 3.3%, and attapulgite 1% and diatomite 4% (dry weight of dual-additives to dry weight of mixture powder). The powdered clay used was obtained from Jining (Shandong, China), the powdered attapulgite and diatomite were manufactured by Zhengzhou (Henan, China). The optimum moisture content (w_{op}) and maximum dry density (ρ_{dmax}) were obtained by compaction test as per JTG E40 T0131-2007. This laboratory compaction method was used to determine the compaction curve compacted in a 152 mm diameter mold with a 45 N rammer dropped from a height of 450 mm, producing a compactive effort of 2677 kN-m/m³ with 3 layers and 98 blows per layer. While, the ASTM D1557 compaction method was used to determine the compaction curve compacted in a 152.4 mm diameter mold with a 44.48 N rammer dropped from a height of 457.2 mm, producing a compactive effort of 2700 kN-m/m³ with 5 layers and 56 blows per layer. The compaction curve of clay and dual-additives (attapulgite 4% and diatomite 1%)-amended clay are shown in Figure 2. The physical properties and main oxide content of these constituent materials used to prepare amended compacted clay are shown in Tables 1 and 2, respectively. The powdered materials used in this study were air dried and passed through a No. 200 (0.075 mm) sieve as specified in ASTM D 698 [32]. The initial moisture content of the specimens was determined to be 30% (weight of water to dry weight of solid). The liquid–plastic limit test and specific gravity test were conducted as per ASTM D 4318 [33] and ASTM D 854 [34], respectively, using distilled water.

Table 1. The physical properties of constituent materials used for preparing amended compacted clay.

Property	Standard	Constituent Material		
		Clay	Attapulgite	Diatomite
Specific gravity, G_s	ASTM D854 (2014)	2.73	-	-
Liquid limit, LL (%)	ASTM D4318 (2018)	54	197	121
Plasticity index, PI (%)	ASTM D2487 (2018)	26	105	35
Classification	ASTM D2487 (2018)	CH	MH	MH
Optimum moisture content, w_{op} (%)	JTG E40 T0131-2007	27.6	-	-
Maximum dry density, ρ_{dmax} (g/cm ³)		1.7	-	-

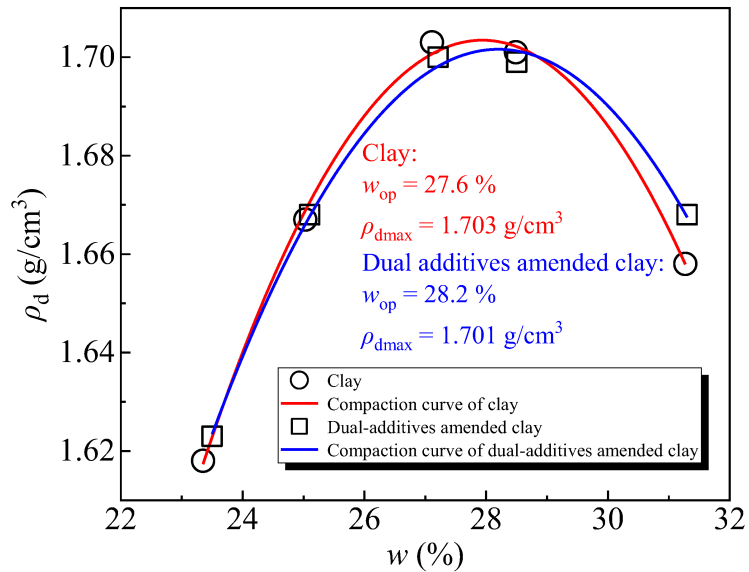


Figure 2. Compaction curve of the clay and dual-additives-amended clay.

Table 2. The main oxide content of attapulgite and diatomite.

Component	SiO ₂	Al ₂ O ₃	Fe ₂ O ₃	Na ₂ O	K ₂ O	CaO	MgO	MnO	TiO ₂	Loss
Content (%) Attapulgite	58.05	9.55	6.2	0.14	1.13	1.18	11.02	0.61	0.47	11.65
Diatomite	90.2	3.4	1.2	0.5	0.5	0.4	0.4	0.61	0.2	2.59

The amended compacted clay in this study was prepared by mixing predetermined amounts of powdered clay, attapulgite, and diatomite directly. The dosage and ratio (dry weight basis) of additives are shown in Table 3. Then, the specimens were prepared by (1) mixing the air-dried clay, attapulgite, and diatomite thoroughly to prepare the dry mixture (Table 3); (2) adding predetermined amounts of tap water incrementally to the dry mixture, then mixing thoroughly and sealing for 24 h to assure homogeneity; (3) compacting by hydraulic pressure and sealing for 14 d until the specimens reached moisture balance. The number of parallel specimens was three. The coefficient of compaction was targeted to be 85%. The diameter of the specimens in the moisture retention and flexible-wall hydraulic conductivity test was set as 50 mm and the height was 50 mm. While, the diameter of the specimens in the gas diffusion test was set as 61.88 mm and the height was 20 mm.

Table 3. The experimental scheme of the moisture retention, liquid limit, and gas diffusion.

Specimens	The Initial Moisture Content	The Additives Dosage	Ratio (Attapulgite: Diatomite)	Test Parameter
Attapulgite-amended	30%	0%, 1%, 3%, 5%, 10%	-	Moisture retention percent (W_t);
Diatomite-amended		0%, 1%, 3%, 5%, 10%	-	Liquid limit (LL); Plastic limit (PL);
Dual-additives-amended		5%	4, 2, 1, 0.5, 0.25	Gas diffusion coefficient (D_θ)

2.2. Moisture Retention Test

In the moisture retention test, the effects of attapulgite dosage, diatomite dosage, and dual-additives ratio on the moisture retention capacity of amended compacted clay were studied respectively. It was characterized by its moisture retention percent, as shown in Equation (1).

$$W_t = \frac{m_{wt}}{m_{w0}} \cdot 100\% = \frac{m_s \cdot w_0 - m_0 - m_t}{m_s \cdot w_0} \cdot 100\% \quad (1)$$

where, W_t is the moisture retention percent of the specimens at time t ; m_{wt} is the mass of moisture in the samples at time t ; m_{w0} is the mass of moisture in the specimens at the initial time; m_s is the total mass of soil during specimens preparation; w_0 is the initial moisture content during specimens preparation; m_0 is the total mass of the specimens at the initial time; m_t is the total mass of the specimens at time t .

The detailed test scheme of the moisture retention test is shown in Table 3. The dosage and ratio of dual-additives were determined through the orthogonal test. The test was conducted according to the following procedure: (1) placing the specimens in a 70×55 mm perforated aluminum box after sealing for 14 d; (2) placing the specimens in the oven, the temperature was targeted to be 60°C , recording the mass change per three hours, and calculating the moisture retention percent of the specimens according to Equation (1) [35–38].

2.3. Gas Diffusion Testing Procedures and Apparatus

In the gas diffusion test, the effects of the attapulgite dosage, the diatomite dosage, and the ratio of dual-additives on the gas diffusion barrier performance of the amended compacted clay were conducted. Oxygen was used in this study, because when the gas dissolves easily in water or reacts with the components in the soil, the measured gas diffusion coefficient of the soil was low, resulting in the test error. The gas barrier performance of amended compacted clay was characterized by gas diffusion coefficient (D_θ) per the research results of Taylor et al. [39–41]. D_θ was calculated based on the first Fick's law and the change rate of oxygen concentration in the diffusion chamber with time:

The first Fick's law is Equation (2):

$$\frac{dq}{dt} = -D_\theta \cdot A \cdot \frac{\Delta C_t}{h_s} \quad (2)$$

where: q is the volume of gas diffusing into the chamber, cm^3 ; t is the diffusion time, s ; A is the diffusion area of specimens, 30 cm^2 in this study; h_s is the height of specimens, 2 cm in this study; D_θ is the gas diffusion coefficient of specimens, cm^2/s ; ΔC_t is the gas concentration gradient of both ends of specimens, g/cm^3 .

The rate of gas diffusion volume into the chamber with time can be also presented as Equation (3):

$$\frac{dq}{dt} = \frac{d(\Delta C_t)}{dt} \cdot h_c \cdot A' \quad (3)$$

where: h_c is the height of the chamber, 15 cm in this study; A' is the diffusion area of the chamber, 133 cm^2 in this study.

Then, Equation (4) is obtained by combining Equations (2) and (3).

$$-D_\theta \cdot A \cdot \frac{\Delta C_t}{h_s} = \frac{d(\Delta C_t)}{dt} \cdot h_c \cdot A' \quad (4)$$

At the initial time ($t = 0$), the oxygen concentration in the diffusion chamber is 0, in the atmosphere is C_0 , ΔC_0 was the difference between the oxygen concentration in the atmosphere and the diffusion chamber before the test, $\Delta C_0 = C_0$. With initial condi-

tions $t = 0$, $\Delta C_t = \Delta C_0 = C_0$, Equation (4) is integrated from 0 to t , obtaining results as Equation (5):

$$\ln\left(\frac{\Delta C_t}{\Delta C_0}\right) = -\frac{D_\theta}{h_s \cdot h_c} \cdot \frac{A}{A'} \cdot t \quad (5)$$

ΔC_0 , h_s , h_c , A , and A' are the constants. Therefore, D_θ can be calculated through the relationship of ΔC_t and t .

The optimal dosage and ratio of additives were determined through the orthogonal test. The test scheme of the gas diffusion test is shown in Table 3. The gas diffusion test was conducted as per the single chamber method recommended by Taylor et al. [39–41]. The testing schematic apparatus used for this study is shown in Figure 3. The apparatus consisted of a gas diffusion chamber, an oxygen transducer (KE-25, HELM AG., Hamburg, Germany), and a data acquisition (NL-115, HELM AG., Hamburg, Germany).

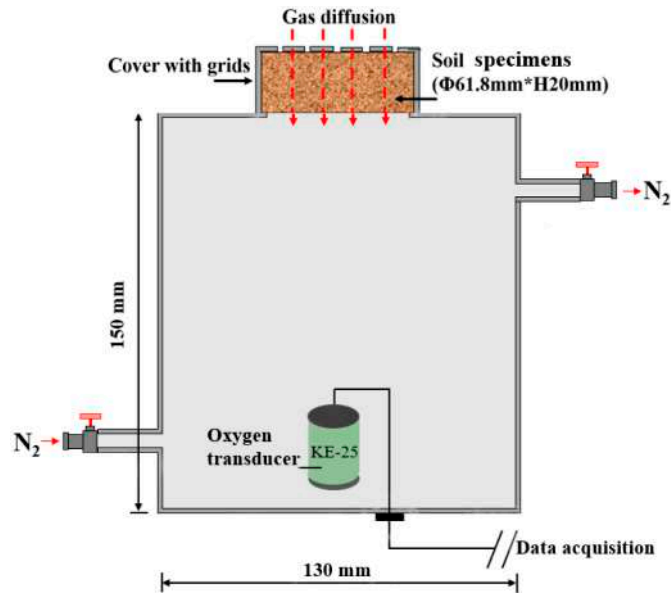


Figure 3. The chamber of soil gas diffusion test.

All experiments were conducted at a room temperature of 25 ± 1 °C and relative humidity of $64\% \pm 2\%$ as per the following procedures: (1) The vacuum grease was applied to the inner wall of the cover (with 85% grids on the top) and outer wall of chamber top for lubrication and sealing. Then the prepared specimens were placed on the top of the chamber, and capped with the cover. (2) The inlet valve connected with the nitrogen cylinder and outlet valve was opened. It was deemed that the air in the chamber was discharged completely by nitrogen until oxygen concentration in the chamber decreased to 0.3–0.6%. Then, the inlet and outlet valves were closed after continuing to supply nitrogen for 10–15 s. (3) The data acquisition and oxygen transducer were used to automatically collect and record the oxygen concentration (C_t) in the chamber per 5 min until the oxygen concentration in the chamber was the same as the atmosphere (C_0) and reached the stable state ($C_t = C_0$). Combining the C_t and C_0 obtained from the above, the gas diffusion coefficient D_θ was calculated based on Equation (5).

2.4. Flexible-Wall Hydraulic Conductivity Test

The unamended, attapulgite-amended, diatomite-amended, and dual-additives (attapulgite 4% and diatomite 1%)-amended compacted clay were prepared with moisture

content of 30% and additives dosage of 5%. The degree of compaction was set as 85%. The specimens of 50 mm in diameter and 50 mm in height were prepared, assembled in a flexible-wall permeameter, and saturated using deaired tap water. Hydraulic conductivity test was conducted in the permeameter using the constant head method as per ASTM D 5084 [42]. All hydraulic conductivity tests in the study were conducted under hydraulic gradients (i) of 40 and effective confining stress of 36.7 kPa calculated by Equation (6) as follows [43–45].

$$\sigma_c' = \sigma_3 - \frac{1}{3}(p_2 + 2p_1) \quad (6)$$

where σ_c' = average effective confining stress; σ_3 = cell pressure (50 kPa in this study); p_1 = bottom seepage pressure (20 kPa in this study); p_2 = top seepage pressure (0 kPa in this study).

2.5. Scanning Electron Microscopy (SEM) and Mercury Intrusion Porosimetry (MIP) Tests

Image analyses using SEM (SIGMA 500, ZEISS-Tech, Jena, Germany) and pore size distribution using MIP (AutoPore V 9620, Micromeritics Instrument Corporation, Atlanta, America) were performed on the amended compacted clay specimens to evaluate the microstructural-amended mechanism. First, the attapulgite-amended, diatomite-amended, dual-additives-amended, and unamended compacted clay specimens were cut into 1 cm³ pieces, the dosages of additives were all 5% (dry weight basis), and the ratio of dual-additives was 4 (dry weight of attapulgite 4% to dry weight of diatomite 1%). Then, the SEM and MIP specimens were frozen using liquid nitrogen for 5 min at a temperature of −120 °C. Sublimation of water was conducted at a temperature of −80 °C for 24 h in a vacuum freeze-drying unit at −18 N (Nanjing Xianou Instruments Manufacture Co., Ltd., Nanjing, China). After freeze-drying, the frozen SEM specimens were cut into small blocks with a natural fracture surface area of approximately 0.25 cm², and these blocks were coated with a thin gold layer and then subjected to SEM analyses. The freeze-dried MIP specimens were subjected to MIP analyses in compliance with ASTM D 4404-18.

2.6. BET Specific Surface Area Test Method (BET) and Thermogravimetric Analysis (TGA)

To evaluate the mechanisms of additives treatment, BET and TGA (DSC200F3, NETZSCH-Gerätebau GmbH, Germany), analyses were conducted on attapulgite-amended, diatomite-amended, dual-additives-amended, and unamended compacted clay specimens. The specimens were prepared according to the procedures as follows. First, the attapulgite-amended, diatomite-amended, dual-additives-amended, and unamended clay powders were mixed thoroughly to prepare the dry mixture. The dosages of additives were all designed as 5% (dry weight basis) and the ratio of dual-additives was 4 (dry weight of attapulgite 4% to dry weight of diatomite 1%). Then, the powder mixtures were frozen using liquid nitrogen for 5 min at a temperature of −120 °C. Sublimation of water was conducted at a temperature of −80 °C for 24 h in a vacuum freeze-drying unit at −18 N (Nanjing Xianou Instruments Manufacture Co., Ltd., Nanjing, China). Then, the specimens were subjected to BET and TG analyses, respectively.

3. Results and Discussion

3.1. Liquid–Plastic Limit and Moisture Retention Tests Results

Figure 4 presents the plasticity chart of the clay amended by additives with different dosages and ratios. The dosage of dual-additives-amended compacted clay was 5%. As the dosage of attapulgite increased from 0% to 10%, the plastic limit of attapulgite-amended specimens increased from 28% to 41%, and the liquid limit increased from 54% to 74%. Its liquid limit increased by 36% compared with unamended clay. With the dosage of diatomite increasing from 0% to 10%, the plastic limit of clay increased from 28% to 29%, and the liquid limit increased from 54% to 57%. Its liquid limit increased by about 5% compared with the unamended clay. The effect of diatomite on the liquid limit of amended

compacted clay was not significant. When the mass ratio of attapulgite to diatomite was 0.25, the plastic limit of the dual-additives-amended compacted clay decreased from 32% to 30%, and the liquid limit decreased from 64% to 60% compared with the mass ratio of 4. The decreasing ranges of plastic limit and liquid limit were 9% and 6% respectively. When the dosage is 5%, the liquid limit of the compacted clay amended by attapulgite and dual-additives (ratio of 4) were 62% and 64% respectively.

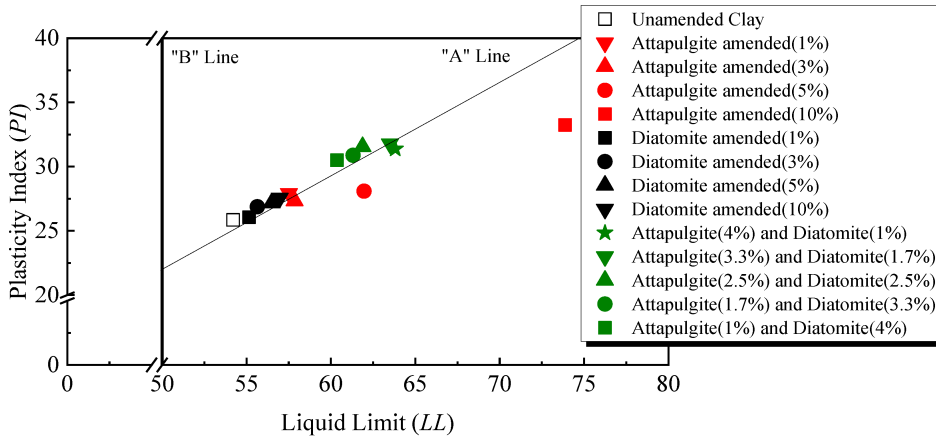


Figure 4. The plasticity chart of the clay amended by additives with different dosages and ratios.

Figure 5 shows how moisture retention percent varies with the dosage of additives. In general, the moisture retention percent increases with the dosage of the attapulgite increasing, while the dosage of diatomite has little effect on its moisture retention percent. The moisture retention percent with the 10% dosage of attapulgite was similar to 5%. When the attapulgite dosage was 5%, the moisture retention percent was about 66% higher than that of unamended clay. Attapulgite could effectively increase the liquid limit of clay and enhance its moisture retention capacity. When the diatomite dosage was 5%, the moisture retention percent was the largest, which was 7% higher than that of unamended clay. Therefore, the dosage of attapulgite and diatomite was found to be 5% considering the cost.

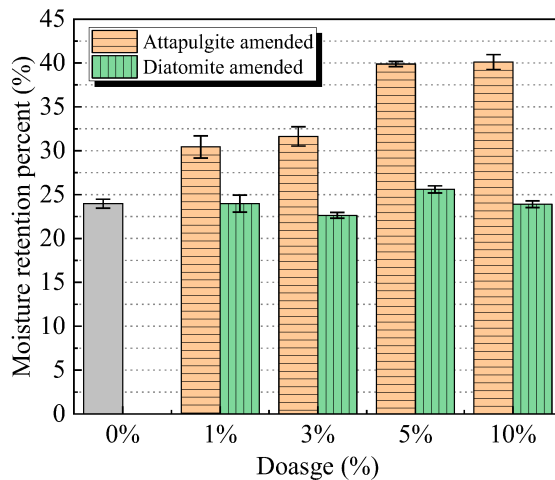


Figure 5. The moisture retention percent with different dosages of attapulgite and diatomite.

Figure 6 presents the variation of moisture retention percent of the dual-additives-amended clay with the ratio of attapulgite to diatomite. The moisture retention capacity of dual-additives-amended compacted clay was the best when the dry weight of attapulgite to the dry weight of diatomite was 4, which was 82% higher than that of unamended clay. It shows that the dual-additives have a great effect on enhancing the moisture retention capacity of amended compacted clay. The liquid limit of compacted clay amended by dual-additives was 3% higher than attapulgite with the dosage of 5%. The moisture retention percent of compacted clay amended by dual-additives (ratio of 4) was 9% higher than attapulgite with the dosage of 5%. Therefore, the increase in the liquid limit of compacted clay amended by additives is one of the reasons for the improvement of its moisture retention capacity.

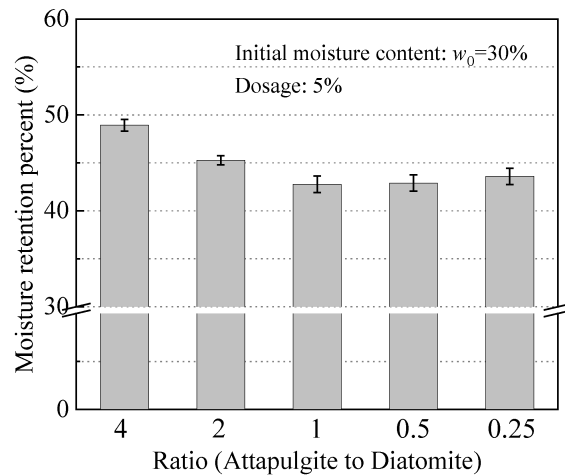


Figure 6. The moisture retention percent with different ratios of attapulgite to diatomite.

The results showed that the attapulgite could greatly increase the moisture retention percent, whereas the diatomite has a limited effect. It is attributed to the molecule's structure [46–48]. There are a lot of pores in the crystal of attapulgite, which could adsorb most cations, water molecules, and organic molecules of a certain size with the Van der Waals Forces, similar to a "zeolite molecular sieve". At the same time, the crystalline water molecules combined with Mg^{2+} at the edge could form a hydrogen bond, which belonged to the synergistic effect of physical adsorption and chemical adsorption. Whereas, the adsorption mechanism of diatomite is mainly chemical adsorption [49–51]. It could adsorb water molecules due to the hydrogen bonds which are combined with the water molecules and the hydroxyl belonged to the Silanol group and silanediol group. However, it has a limited effect on enhancing the moisture retention percent of clay due to the weak chemical adsorption. Therefore, attapulgite could be screened as an additive to enhance the moisture retention capacity.

3.2. Gas Diffusion Test Results

The results of the gas diffusion test of the compacted clay amended by attapulgite or diatomite are shown in Figure 7. The oxygen concentration in the diffusion chamber increased with the time of all dosages. At which time the oxygen concentrations inside and outside the chamber were the same, it reached equilibrium. Figure 7 presents that the D_{θ} decreased with the increase of attapulgite dosage and its gas barrier performance gradually improved. With the increase in dosage of diatomite, the diffusion rate of oxygen decreased. It shows that diatomite has a good effect on gas barrier performance. It also indicates that diatomite could reduce the D_{θ} of clay better.

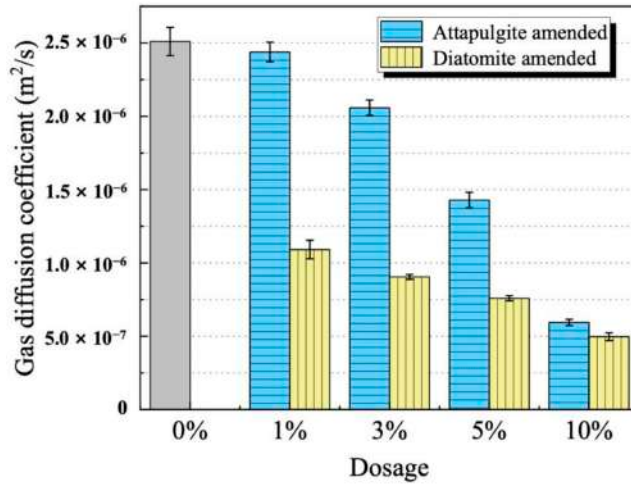


Figure 7. The gas diffusion coefficient with different dosages of attapulgit and diatomite.

The results of the gas diffusion test with different ratios of dual-additives are shown in Figure 8. The initial moisture content was 30% and the dosage of dual-additives was 5% of all the specimens. Among that, the D_{θ} of the amended clay was the lowest at $4.4 \times 10^{-7} \text{ m}^2/\text{s}$ when the ratio was 1. After considering the economic cost, the dosage of diatomite should be reduced as much as possible. Therefore, it is suggested that the mass ratio of attapulgit to diatomite be 4, the dosage 5%, and the D_{θ} of the amended compacted clay $8.5 \times 10^{-7} \text{ m}^2/\text{s}$, reduced by about 42% compared with the unamended clay.

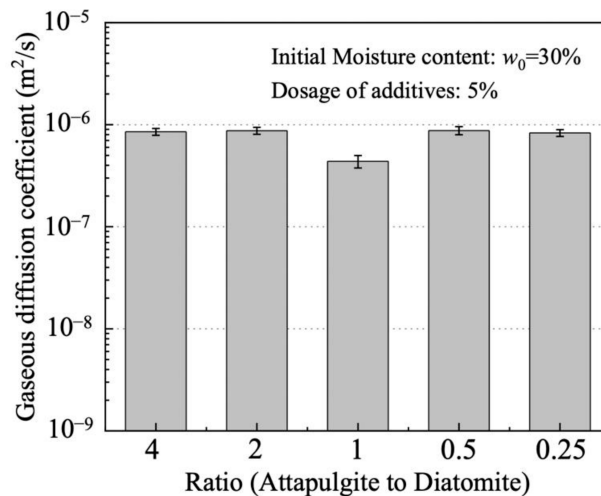


Figure 8. The effect of ratios of additives on the gas diffusion coefficient.

Comparing the gas diffusion test results of the clay amended by attapulgit and diatomite, it can be obtained that the effect of diatomite on the gas barrier performance of the clay is more obvious compared with that of attapulgit, which can be attributed to those crystal structures. Nevertheless, the attapulgit crystals are chain structures or fibrous structures [48], meaning the gas could still migrate through the gap of fibrous or chain structure between the crystals after mixing and compaction. While diatomite, as a porous

layered siliceous rock of biological genesis, is composed of diatom wall shells, which are distributed with microporous structure [49–51]. There are few and complex channels for gas migration owing to its wall shells. Therefore, diatomite could be screened as one of the additives to improve the gas barrier performance of amended compacted clay.

In conclusion, it is apparent that the optimal dosage of dual-additives was determined to be 5% and the mass ratio of attapulgite to diatomite 4, based on the experimental results of moisture retention percent and gas diffusion coefficient. In addition, the economic cost is also a factor to be considered.

3.3. Flexible-Wall Hydraulic Conductivity Test Results

Figure 9 shows the results of hydraulic conductivity of amended compacted clay. During permeation with tap water, the k of the unamended, attapulgite amended, diatomite amended, and dual-additives-amended compacted clay were 8.3×10^{-9} m/s, 6.3×10^{-9} m/s, 7.4×10^{-9} m/s, and 5.9×10^{-9} m/s, respectively. Importantly, the k of compacted clay amended by attapulgite, diatomite, and dual-additives were lower than unamended compacted clay, which decreased by 25%, 11%, and 29%, respectively. These results indicate that the dual-additives-amended clay possessed better hydraulic performance than unamended clay.

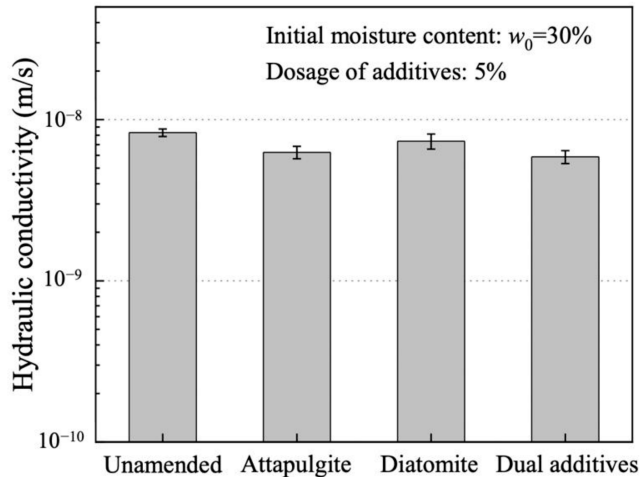


Figure 9. The flexible wall penetration test results of amended compacted clay.

3.4. SEM, BET, MIP, and TGA Tests Results

SEM images for the compacted clay specimens (a) Unamended; (b) Attapulgite-amended; (c) Diatomite-amended; and (d) Dual-additives-amended are shown in Figure 10. It is seen from Figure 10a that the flaky, unamended compacted clay particles polymerize to form agglomerates. There are gaps between adjacent agglomerates for gas and water molecules to pass through. Figure 10b shows that the acicular attapulgite particles attached to the surface of the clay and filled the gaps, which reduced the gaps between clay particles and increased the water retention percent. Figure 10c presents that the size of diatomite particles with micropores was larger than clay particles. The pores between the clay particles decreased, and the micropores on the surface of the diatomite made the gas migration path more complex. However, the microporous structure was larger than those of “zeolite molecular sieve”, which had a limited effect on moisture molecules adsorption. Therefore, it had a limited effect on the enhancement of moisture retention performance. Figure 10d shows that the dual-additives filled and decreased the pores between clay particles and the micropores structure made the gas migration more complex and difficult.

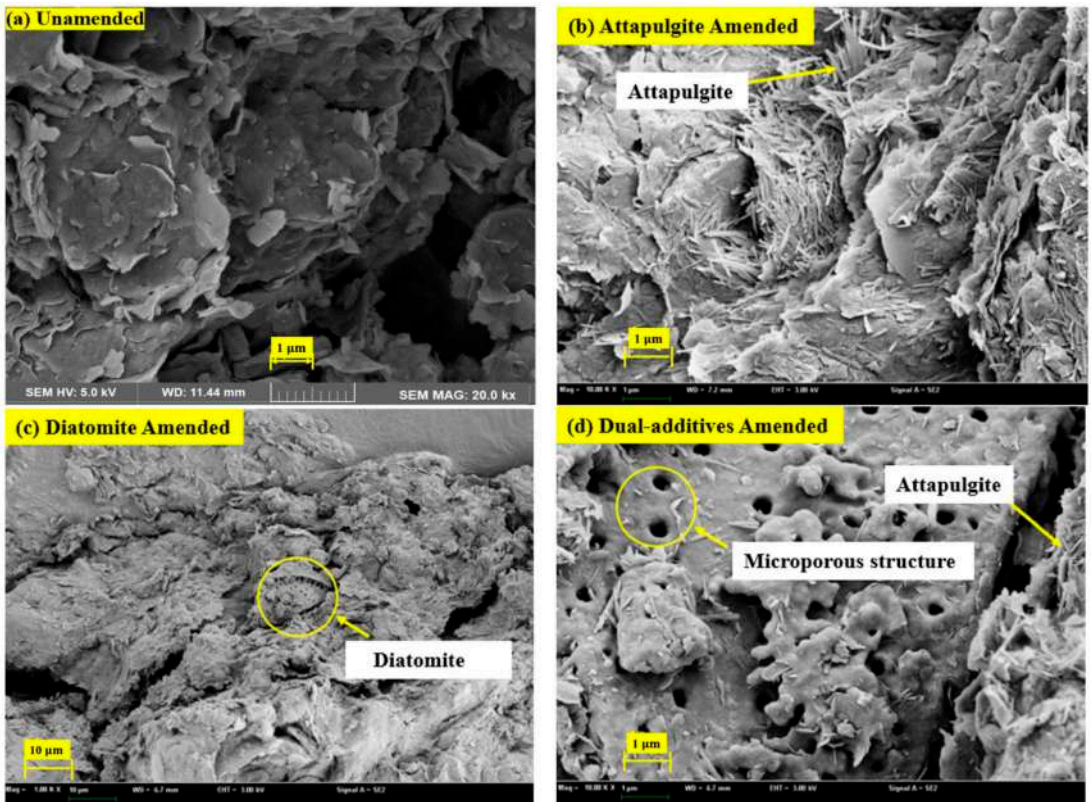


Figure 10. SEM images of compacted clay specimens.

Figure 11 shows the cumulative intruded pore volume and incremental intruded pore volume vs. pore size diameter (PSD) of amended compacted clay specimens with different additives (dosage 5%). The distribution is shown for a diameter range of 3 nm to 425 μm and a pressure range of 0.1 pasi to 61,000 pasi. The average PSD of specimens amended by dual-additives, attapulgite, diatomite, and unamended were 30.6, 31.19, 35.02, and 47.28 nm respectively. Porosities were 19.4%, 21.5%, 27.2%, and 47.3% respectively. The average PSD and porosity of dual-additives-amended compacted clay decreased by 55% and 144% respectively compared with unamended ones. Figure 11a presents that the cumulative intruded pore volume of all amended specimens was lower than unamended ones, regardless of PSD. The cumulative intruded pore volume of dual-additives-amended was the lowest, which decreased by 60% at PSD of 5 nm compared with unamended. It illustrates that the dual-additives filled the gaps and pores of compacted clay significantly. Figure 11b shows that the incremental intruded pore volume of unamended compacted clay increased significantly at a PSD of 100 nm. The peak of curves of amended compacted clay were in the range of 5–100 nm, especially at 15 and 40 nm. The incremental intruded pore volume of all specimens was almost zero in the range of 500–100,000 nm. It indicates that almost all of the pores in amended compacted clay had a diameter range of 5–500 nm. Therefore, the dual-additives could enhance moisture retention and gas barrier performance by decreasing the gaps and pores of compacted clay.

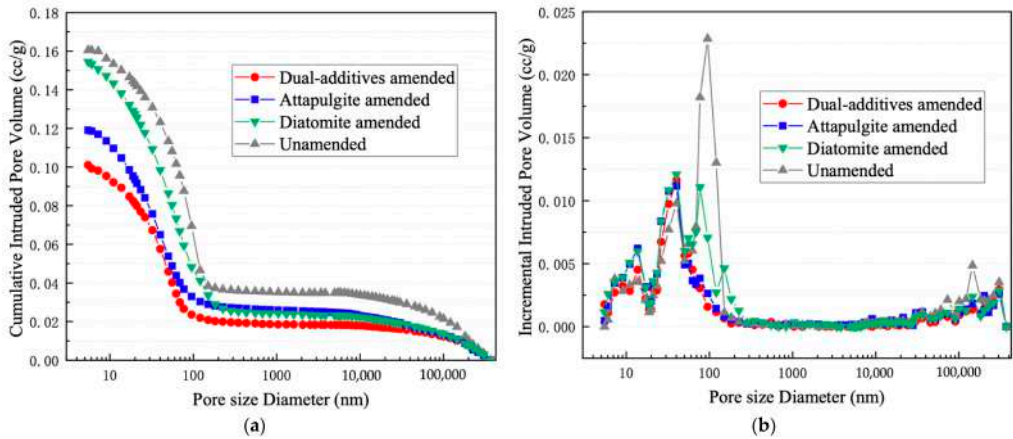


Figure 11. MIP results of amended compacted clay specimens: (a) cumulative intruded pore volume vs. pore size diameter; and (b) incremental intruded pore volume.

The BET test results of clay powder amended by different additives are shown in Figure 12. The PSDs of less than 2 nm, 2–50 nm, and larger than 50 nm were defined as microporous, mesoporous, and macroporous respectively. It is seen that the microporous amount of amended clay increased significantly compared with unamended clay, and the mesoporous and microporous volume increases were not significant. The microporous volume of attapulgite-amended, diatomite-amended, and dual-additives-amended clay were $0.00721 \text{ cm}^3/\text{g}\cdot\text{nm}$, $0.00707 \text{ cm}^3/\text{g}\cdot\text{nm}$, and $0.00724 \text{ cm}^3/\text{g}\cdot\text{nm}$ respectively when the pore size diameter was 2 nm, increases of 9%, 7%, and 9% respectively compared with unamended clay. So, the dual-additives could enhance the moisture retention performance of compacted clay. The specific surface area and Density Functional Theory (DFT) pore distribution results are presented in Table 4. It was seen that the specific surface area of clay amended by additives increased 13–15% compared with unamended clay. The volume of microporous and mesoporous attapulgite and dual-additives-amended clay increased significantly. Therefore, the dual-additives decreased the microporous size diameter of clay powder and increased its specific surface area.

Table 4. The BET test results.

Specimens	Dosage	Ratio (Attapulgite to Diatomite)	Specific Surface Area (m^2/g)	DFT Pore Distribution (cm^3/g)		Average Microporous Size Diameter (nm)
				Less than 1.863 nm	Less than 19.577 nm	
Unamended	-	-	43.5843	0.01119	0.05508	0.7847
Attapulgite-amended	5%	-	49.7271	0.01284	0.07191	0.7829
Diatomite-amended	5%	-	45.4255	0.01201	0.05729	0.7803
Dual-additives-amended	5%	4	49.3243	0.01284	0.06779	0.7811

The TGA test results of clay amended by different additives are shown in Figure 13. The water in the clay was classified into tightly bound water (TBW) connected with clay minerals by hydrogen bond, loosely bound water (LBW) connected with clay minerals by molecular force [52,53], and free water; the limit of water decomposition temperature was 120–230 °C, 75–120 °C, and 25–75 °C respectively [54]. The DTG curve was obtained from the differentiation of the TG curve. Each minimum point at the valley on the DTG curve represents the water decomposition point. Figure 13a shows that the temperature limits of TBW, LBW, and free water of unamended clay were 29.4 °C, 101.55 °C, and 184.41 °C respectively. The LBW temperature limit of attapulgite-amended clay was 106.68 °C, an increase of 5.05% compared with unamended clay, and its TBW temperature limit was 210.46 °C, an increase of 14%. The LBW temperature limit of diatomite-amended clay was

105.10 °C, an increase of 3.5%, and that of dual-additives-amended clay increased by 8.9%. The TBW and free water have no relationship with the moisture retention performance of clay. The LBW is double-diffuse layers (DDLs) of clay minerals [55,56], which is the critical factor in the moisture retention performance of clay. Figures 4,5 and 13, present that the trend of the temperature limit of clay amended by different additives is consistent with the results of moisture retention percent and liquid limit. It illustrates that the moisture retention percent of amended clay increases with the increasing the temperature limit of LBW. That is attributed to the fact that the thermal energy required to lose the same amount of LBW is greater with the increasing temperature limit; therefore, its moisture retention performance is enhanced at the same temperature (60 °C).

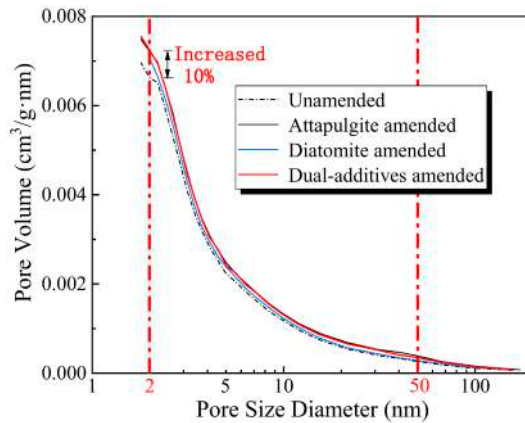


Figure 12. BET tests results of clay specimens amended by attapulgite, diatomite, dual-additives, and unamended.

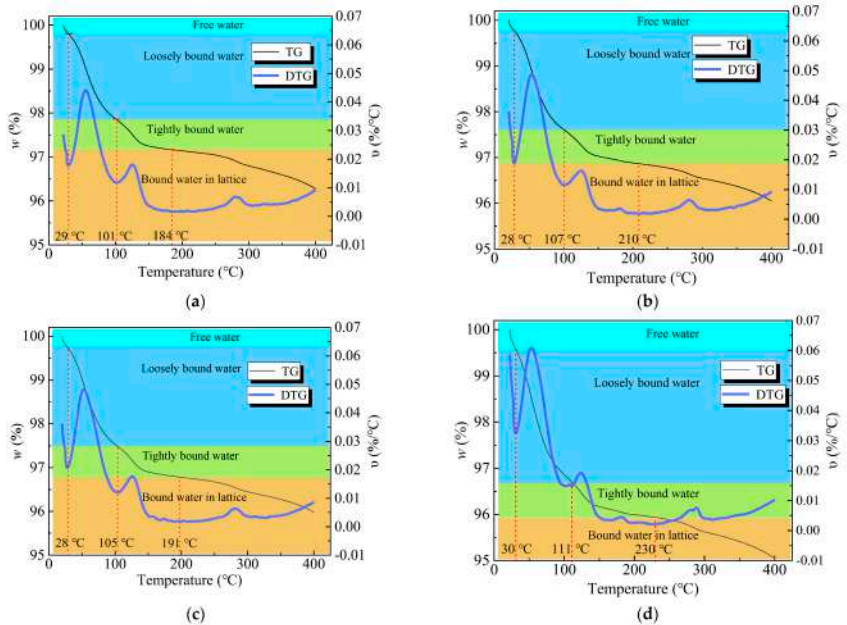


Figure 13. TG tests results of specimens: (a) Unamended; (b) Attapulgite-amended; (c) Diatomite-amended; and (d) Dual-additives-amended.

4. Conclusions

The optimum dosage and ratio of additives for amending compacted clay were screened and determined through moisture retention and gas diffusion test. The principal reason for the enhancement of its moisture retention capacity was investigated by the liquid–plastic limit test. Subsequently, the hydraulic performance of the compacted clay amended by additives and unamended was conducted. Based on the results, the following conclusions can be drawn:

1. The attapulgite could enhance the moisture retention performance of the clay, but its effect on gas barrier performance was limited. When its dosage was 5%, its moisture retention percent was 66% higher than that of unamended clay. The enhancement mechanism behind the phenomenon is attributed to increasing the liquid limit of clay;
2. The diatomite could effectively decrease the gas diffusion coefficient of clay, while it had a limited effect on the moisture retention performance. As its dosage was 5%, the moisture retention percent of clay only increased by 7%;
3. Considering the moisture retention capacity, gas barrier performance, and cost, the optimal dosage of dual-additives was targeted to be 5%, and the optimal ratio of attapulgite to diatomite was 4. The moisture retention percent of the dual-additives-amended compacted clay increased by 82%, and the gas diffusion coefficient decreased by 42% compared with unamended clay. The k of enhanced compacted clay amended by attapulgite and dual-additives was 6.3×10^{-9} m/s and 5.9×10^{-9} m/s respectively, decreases of 25% and 29% compared with the unamended clay;
4. The SEM and MIP analyses presented that dual-additives effectively filled the intergranular pores of the amended clay and micropore structure increased the gas migration path. The BET test results showed that dual-additives increased the amount of microporous to enhance the moisture retention performance of amended clay. Meanwhile, the dual-additives increased the specific surface area and decreased the average PSD. The TGA results demonstrated that dual-additives increased the temperature limit of loosely bound water to enhance the moisture retention performance of amended clay.

Author Contributions: Conceptualization, M.W., J.W. and Y.D.; methodology, M.W., Y.D. and J.W.; software, M.W.; validation, M.W. and N.J.; formal analysis, M.W. and J.W.; investigation, M.W., J.W. and H.Z.; resources, M.W.; data curation, M.W. and J.W.; writing—original draft preparation, M.W., J.W., H.Z. and W.X.; writing—review and editing, M.W., Y.D., H.Z. and N.J.; visualization, M.W.; supervision, M.W., Y.D. and W.X.; project administration, Y.D.; funding acquisition, Y.D. All authors have read and agreed to the published version of the manuscript.

Funding: Financial support for this project was provided by the National Key R&D Program of China (Grant No. 2018YFC1803100), the National Natural Science Foundation of China (Grant Nos. 41877248, 42177133, and 41902276).

Data Availability Statement: Some or all data, models, or code that support the findings of this study are available from the corresponding author upon reasonable request.

Conflicts of Interest: The authors declare that they have no known competing financial interests or personal relationships that could have appeared to influence the work reported in this paper.

References

1. Chen, Z.; Kamchoom, V.; Chen, R. Landfill gas emission through compacted clay considering effects of crack pathway and intensity. *Waste Manag.* **2022**, *143*, 215–222. [PubMed]
2. Albright, W.H.; Benson, C.H.; Gee, G.W.; Abichou, T.; McDonald, E.V.; Tyler, S.W.; Rock, S.A. Field performance of a compacted clay landfill final cover at a humid site. *J. Geotech. Geoenviron. Eng.* **2006**, *132*, 1393–1403.
3. Ng, C.W.W.; Chen, Z.K.; Coe, J.L.; Chen, R.; Zhou, C. Gas breakthrough and emission through unsaturated compacted clay in landfill final cover. *Waste Manag.* **2015**, *44*, 155–163. [PubMed]
4. Mahmoodlu, M.G.; Hassanizadeh, S.M.; Hartog, N.; Raoof, A.; van Genuchten, M.T. Evaluation of a horizontal permeable reactive barrier for preventing upward diffusion of volatile organic compounds through the unsaturated zone. *J. Environ. Manag.* **2015**, *163*, 204–213.

5. Verginelli, I.; Capobianco, O.; Hartog, N.; Baciocchi, R. Analytical model for the design of in situ horizontal permeable reactive barriers (HPRBs) for the mitigation of chlorinated solvent vapors in the unsaturated zone. *J. Contam. Hydrol.* **2017**, *197*, 50–61.
6. Rowe, R.K.; Brachman, R.W.I. Assessment of equivalence of composite liners. *Geosynth. Int.* **2004**, *11*, 273–286.
7. Hewitt, P.J.; Philip, L.K. Problems of clay desiccation in composite lining systems. *Eng. Geol.* **1999**, *53*, 107–113.
8. Omid, G.H.; Thomas, J.C.; Brown, K.W. Effect of desiccation cracking on the hydraulic conductivity of a compacted clay liner. *Water Air Soil Pollut.* **1996**, *89*, 91–103.
9. Julina, M.; Thyagaraj, T. Combined effects of wet-dry cycles and interacting fluid on desiccation cracks and hydraulic conductivity of compacted clay. *Eng. Geol.* **2020**, *267*, 105505.
10. Aldaeef, A.A.; Rayhani, M.T. Hydraulic performance of compacted clay liners under simulated daily thermal cycles. *J. Environ. Manag.* **2015**, *162*, 171–178.
11. Tang, C.S.; Shi, B.; Liu, C.; Suo, W.B.; Gao, L. Experimental characterization of shrinkage and desiccation cracking in thin clay layer. *Appl. Clay Sci.* **2011**, *52*, 69–77.
12. Amarasiri, A.L.; Kodikara, J.K.; Costa, S. Numerical modelling of desiccation cracking. *Int. J. Numer. Anal. Methods Geomech.* **2011**, *35*, 82–96.
13. Kodikara, J.K.; Choi, X. A simplified analytical model for desiccation cracking of clay layers in laboratory tests. In *Unsaturated Soils, Proceedings of the UNSAT 2006 Conference, Carefree, AZ, USA, 2–6 April 2006*; Miller, G.A., Zapata, C.E., Houston, S.L., Fredlund, D.G., Eds.; ASCE Geotechnical Special Publication: Carefree, AZ, USA, 2006; Volume 2, pp. 2558–2567.
14. Albrecht, B.A.; Benson, C.H. Effect of desiccation on compacted natural clays. *J. Geotech. Geoenviron. Eng.* **2001**, *127*, 67–75.
15. Kabiri, K.; Omidian, H.; Zohuriaan-Mehr, M.J.; Doroudiani, S. Superabsorbent hydrogel composites and nanocomposites: A review. *Polym. Compos.* **2011**, *32*, 277–289.
16. Farrell, C.; Ang, X.Q.; Rayner, J.P. Water-retention additives increase plant available water in green roof substrates. *Ecol. Eng.* **2013**, *52*, 112–118.
17. Polman, E.M.; Gruter, G.J.M.; Parsons, J.R.; Tietema, A. Comparison of the aerobic biodegradation of biopolymers and the corresponding bioplastics: A review. *Sci. Total Environ.* **2021**, *753*, 141953.
18. Florez, C.; Restrepo-Baena, O.; Tobon, J.I. Effects of calcination and milling pre-treatments on natural zeolites as a supplementary cementitious material. *Constr. Build. Mater.* **2021**, *310*, 125220.
19. Conant, B.H.; Gillham, R.W.; Mendoza, C.A. Vapor transport of trichloroethylene in the unsaturated zone: Field and numerical modeling investigations. *Water Resour. Res.* **1996**, *32*, 9–22.
20. You, K.; Zhan, H. Comparisons of diffusive and advective fluxes of gas phase volatile organic compounds (VOCs) in unsaturated zones under natural conditions. *Adv. Water Resour.* **2013**, *52*, 221–231.
21. Li, H.; Jiao, J.J. One-dimensional airflow in unsaturated zone induced by periodic water table fluctuation. *Water Resour. Res.* **2005**, *41*, 1–10. [[CrossRef](#)]
22. Li, J.; Zhan, H.; Huang, G.; You, K. Tide-induced airflow in a two-layered coastal land with atmospheric pressure fluctuations. *Adv. Water Resour.* **2011**, *34*, 649–658.
23. You, K.; Zhan, H. Can atmospheric pressure and water table fluctuations be neglected in soil vapor extraction? *Adv. Water Resour.* **2012**, *35*, 41–54.
24. Jiao, J.J.; Li, H. Breathing of coastal vadose zone induced by sea level fluctuations. *Geophys. Res. Lett.* **2004**, *31*, L11502. [[CrossRef](#)]
25. Guo, H.P.; Jiao, J.J. Numerical study of airflow in the unsaturated zone induced by sea tides. *Water Resour. Res.* **2008**, *44*, W06402. [[CrossRef](#)]
26. You, K.; Zhan, H.; Li, J. A new solution and data analysis for gas flow to a barometric pumping well. *Adv. Water Resour.* **2010**, *33*, 1444–1455.
27. You, K.; Zhan, H.; Li, J. Gas flow to a barometric pumping well in a multilayer unsaturated zone. *Water Resour. Res.* **2011**, *47*, W05522. [[CrossRef](#)]
28. Choi, J.W.; Smith, J.A. Geoenvironmental factors affecting organic vapor advection and diffusion fluxes from the unsaturated zone to the atmosphere under natural conditions. *Environ. Eng. Sci.* **2005**, *22*, 95–108.
29. Smith, J.A.; Chiou, C.T.; Kammer, J.A.; Kile, D.E. Effect of soil moisture on the sorption of trichloroethene vapor to vadose-zone soil at Picatinny Arsenal, New Jersey. *Environ. Sci. Technol.* **1990**, *24*, 676–683.
30. Batterman, S.A.; McQuown, B.C.; Murthy, P.N.; McFarland, A.R. Design and evaluation of a long-term soil gas flux sampler. *Environ. Sci. Technol.* **1992**, *26*, 709–714.
31. Rowe, R.K. Environmental Geotechnics: Past, Present and Future? In *Proceedings of the 8th International Congress on Environmental Geotechnics, Hangzhou, China, 28 October–1 November 2018*; Springer: Singapore, 2018.
32. *ASTM D 698*; Standard Test Methods for Laboratory Compaction Characteristics of Soil Using Standard Effort (12,400 ft-lbf/ft³ (600 kN-m/m³)). ASTM: West Conshohocken, PA, USA, 2012.
33. *ASTM D 4318*; Standard Test Methods for Liquid Limit, Plastic Limit, and Plasticity Index of Soils. ASTM: West Conshohocken, PA, USA, 2018b.
34. *ASTM D 854*; Standard Test Methods for Specific Gravity of Soil Solids by Water Pycnometer. ASTM: West Conshohocken, PA, USA, 2014b.
35. Sun, L.P.; Du, Y.M.; Shi, X.W.; Chen, X.; Yang, J.H.; Xu, Y.M. A new approach to chemically modified carboxymethyl chitosan and study of its moisture-absorption and moisture-retention abilities. *J. Appl. Polym. Sci.* **2006**, *102*, 1303–1309.

36. Barajas-Ledesma, R.M.; Wong, V.N.; Little, K.; Patti, A.F.; Garnier, G. Carboxylated nanocellulose superabsorbent: Biodegradation and soil water retention properties. *J. Appl. Polym. Sci.* **2022**, *139*, 51495.
37. Mi, Y.; Miao, Q.; Cui, J.; Tan, W.; Guo, Z. Novel 2-Hydroxypropyltrimethyl Ammonium Chitosan Derivatives: Synthesis, Characterization, Moisture Absorption and Retention Properties. *Molecules* **2021**, *26*, 4238. [[CrossRef](#)]
38. Wang, J.; Jin, W.; Hou, Y.; Niu, X.; Zhang, H.; Zhang, Q. Chemical composition and moisture-absorption/retention ability of polysaccharides extracted from five algae. *Int. J. Biol. Macromol.* **2013**, *57*, 26–29. [[PubMed](#)]
39. Taylor, S.A. Oxygen diffusion in porous media as a measure of soil aeration. *Soil Sci. Soc. Am. J.* **1950**, *14*, 55–61.
40. Currie, J.A. Gaseous diffusion in porous media Part 1. A non-steady state method. *Br. J. Appl. Phys.* **1960**, *11*, 314–317.
41. Su, Z.; Wu, B.; Gong, Y. Determination of gas diffusion coefficient in soils with different porosities. *Trans. Chin. Soc. Agric. Eng.* **2015**, *31*, 108–113.
42. *ASTM D5084*; Standard Test Methods for Measurement of Hydraulic Conductivity of Saturated Porous Materials Using a Flexible Wall Permeameter. ASTM: West Conshohocken, PA, USA, 2016.
43. Malusis, M.A.; McKeehan, M.D. Chemical compatibility of model soil-bentonite backfill containing multiswellable bentonite. *J. Geotech. Geoenviron. Eng.* **2013**, *139*, 189–198.
44. Bohnhoff, G.L.; Shackelford, C.D. Hydraulic conductivity of polymerized bentonite-amended backfills. *J. Geotech. Geoenviron. Eng.* **2014**, *140*, 04013028.
45. Yang, Y.L.; Reddy, K.R.; Du, Y.J.; Fan, R.D. Short-term hydraulic conductivity and consolidation properties of soil-bentonite backfills exposed to CCR-impacted groundwater. *J. Geotech. Geoenviron. Eng.* **2018**, *144*, 04018025.
46. Boudriche, L.; Calvet, R.; Hamdi, B.; Balard, H. Effect of acid treatment on surface properties evolution of attapulgite clay: An application of inverse gas chromatography. *Colloid. Surf.* **2011**, *392*, 45–54.
47. Duan, Z.; Zhao, Q.; Wang, S.; Yuan, Z.; Zhang, Y.; Li, X.; Wu, Y.; Jiang, Y.; Tai, H. Novel application of attapulgite on high performance and low-cost humidity sensors. *Sens. Actuators B Chem.* **2020**, *305*, 127534.
48. Liu, D.B.; Li, Y.; Xiao, H.F.; Xu, L.D.; Zhou, Y.Z.; Han, W.Y.; Li, H.R.; Jiang, Y.M.; Qiu, Y.S. Attapulgite Clay and Its Application in Radionuclide Treatment: A Review. *Sci. Adv. Mater.* **2018**, *10*, 1529–1542.
49. de Namor, A.F.D.; El Gamouz, A.; Frangie, S.; Martinez, V.; Valiente, L.; Webb, O.A. Turning the volume down on heavy metals using tuned diatomite. A review of diatomite and modified diatomite for the extraction of heavy metals from water. *J. Hazard. Mater.* **2012**, *241*, 14–31.
50. Sun, M.; Zou, C.; Xin, D. Pore structure evolution mechanism of cement mortar containing diatomite subjected to freeze-thaw cycles by multifractal analysis. *Cem. Concr. Compos.* **2020**, *114*, 103731.
51. Zheng, J.; Shi, J.; Ma, Q.; Dai, X.; Chen, Z. Experimental study on humidity control performance of diatomite-based building materials. *Appl. Therm. Eng.* **2017**, *114*, 450–456.
52. Li, Y.L.; Wang, T.H.; Su, L.J. Determination of bound water content of loess soils by isothermal adsorption and thermogravimetric analysis. *Soil Sci.* **2015**, *180*, 90–96.
53. Li, S.; Wang, C.; Zhang, X.; Zou, L.; Dai, Z. Classification and characterization of bound water in marine mucky silty clay. *J. Soils Sediments* **2019**, *19*, 2509–2519.
54. Wang, Y.; Lu, S.; Ren, T.; Li, B. Bound water content of air-dry soils measured by thermal analysis. *Soil Sci. Soc. Am. J.* **2011**, *75*, 481–487.
55. Fu, X.L.; Shen, S.Q.; Reddy, K.R.; Yang, Y.L.; Du, Y.J. Hydraulic Conductivity of Sand/Biopolymer-Amended Bentonite Backfills in Vertical Cutoff Walls Permeated with Lead Solutions. *J. Geotech. Geoenviron. Eng.* **2022**, *148*, 04021186.
56. Zhuang, H.; Wang, J.; Gao, Z. Anisotropic and Noncoaxial Behavior of Soft Marine Clay under Stress Path Considering the Variation of Principal Stress Direction. *Int. J. Geomech.* **2022**, *22*, 04022062.

Article

A Calculation Method of Thermal Pore Water Pressure Considering Overconsolidation Effect for Saturated Clay

Gailei Tian and Zhihong Zhang *

Key Laboratory of Urban Security and Disaster Engineering of China Ministry of Education, Beijing University of Technology, Beijing 100124, China; tiangailei@emails.bjut.edu.cn

* Correspondence: zhangzh2002@bjut.edu.cn

Abstract: With the increase of soil consolidation degree, the pore water pressure induced by thermal loading drops dramatically. To conveniently and quickly calculate the thermal pore water pressure inside the soil under different overconsolidation states and quantify overconsolidation effect on thermal pore water pressure, a calculation method of thermal pore water pressure considering overconsolidation effect for saturated clay is proposed. The method is verified by the relevant experimental data, and good agreements were achieved. Through analyzing the influence mechanism of *OCR* on the thermal pore water pressure, three important findings were captured. (1) For overconsolidated clay, thermal pore water pressure decreases nonlinearly with the increase of *OCR*. (2) There is a critical threshold of *OCR* 4.3; when $1 < OCR \leq 4.3$ (slightly overconsolidated state), the ratio of compression line slope to recompression line slope (λ) of overconsolidated clay is consistent with that of the normally consolidated clay, while when $OCR > 4.3$ (highly overconsolidated state), the value of λ is smaller than that of normally consolidated clay. (3) For highly overconsolidated clay ($OCR > 4.3$), considering the reducing of λ with *OCR*, the prediction accuracy of the thermal pore pressure calculation method has been greatly improved; especially when *OCR* equals 30, the prediction accuracy improves by 92.7% as temperature change achieves 35 °C.

Keywords: overconsolidation effect; thermal pore water pressure; calculation method; saturated clay

Citation: Tian, G.; Zhang, Z. A Calculation Method of Thermal Pore Water Pressure Considering Overconsolidation Effect for Saturated Clay. *Appl. Sci.* **2022**, *12*, 6325. <https://doi.org/10.3390/app12136325>

Academic Editor: Bing Bai

Received: 20 May 2022

Accepted: 19 June 2022

Published: 21 June 2022

Publisher's Note: MDPI stays neutral with regard to jurisdictional claims in published maps and institutional affiliations.



Copyright: © 2022 by the authors. Licensee MDPI, Basel, Switzerland. This article is an open access article distributed under the terms and conditions of the Creative Commons Attribution (CC BY) license (<https://creativecommons.org/licenses/by/4.0/>).

1. Introduction

During the service period of buffer materials for nuclear waste repository [1–3], thermal prefabricated vertical drains [4,5], geothermal energy piles [6], and buried cables and pipelines [7], the temperature of the surrounding soil may change significantly. However, when the soil temperature changes, thermal pore water pressure will be generated in the soil due to the difference of thermal expansion characteristics between the pore fluid and soil particles. In case of geological formations with low hydraulic conductivity, the thermal pore water can cause the loss of effective stress. Furthermore, with the dissipation of thermal pore water pressure, the soil will produce additional thermal volume change. It is found that the magnitude of thermal pore water pressure mainly depends on the stress history. Knowledge of the volume change of saturated soil under different stress states, which is a key factor that needs to be considered in design of thermo-active structures, must accurately estimate the thermal pore water pressure with different degrees of overconsolidation.

A series of studies have investigated the thermal response of saturated clay soils. To explore the evolution law of thermal pore water pressure under undrained conditions, Campanella and Mitchell [8], Ghaaowd et al. [9], Abuel-Naga et al. [10], and Ghabezloo et al. [11] carried out related experimental investigations. These experimental studies found that the magnitude of thermal pore water pressure depends on the compressibility of the soil, the physicochemical coefficient of structural volume change, initial void ratio, initial effective stress, the change in temperature, and thermal expansion coefficients of pore water and soil particles. Furthermore, Abuel-Naga et al. [10], Ghabezloo et al. [11],

Burghignoli et al. [12], and McCartney [13] explored the thermally induced volume change of soil by conducting drainage heating tests. Among them, Abuel-Naga et al. [10] used the theoretical microstructure mechanism to explain the thermally induced volume change behavior under different stresses. Based on the principle of particle rearrangement in porous granular materials undergoing thermodynamic process, Bai et al. [14,15] established a thermo-hydro-mechanical constitutive model. This model can accurately describe the irreversible consolidation of normally consolidated saturated soils induced under thermal loading and the aging effect caused by cyclic thermal loading. Subsequently, under the framework of granular thermodynamics, Bai et al. [16] derived a generalized effective stress principle, which can automatically consider the influence of the stress path, temperature path, and soil structure.

It should be noted that both the magnitude of thermal pore water pressure and the sign of the thermally induced volume change are affected by the degree of overconsolidation [10,12,14,17]. With the dissipation of the thermal pore water pressure, normally consolidated clays will exhibit irreversible volume shrinkage, highly overconsolidated clays will undergo elastic thermal expansion, and slightly overconsolidated clays will show a volume change trend that expands first and then shrinks [13,18–20]. Meanwhile, for overconsolidated clays, there is a transition temperature. When the soil temperature exceeds the transition temperature, soil deformation will change from expansion to contraction [18,21–23]. The reason for the different deformation laws of soils with different overconsolidation degrees may be due to the difference in thermal pore water pressure [21]. To explore the effect of overconsolidation ratio on the changes of thermal pore water pressure and thermal volume, constitutive models that can consider the influence of stress history are established based on the Cambridge model or modified Cambridge model [3,10,24,25]. However, because the yield caused by temperature and stress is considered, many parameters are involved in these constitutive models, which makes the solution process extremely cumbersome. Furthermore, these constitutive models cannot obtain an explicit expression of thermal pore water pressure [26], which makes engineering applications very inconvenient. To conveniently and quickly predict the thermal pore water pressure, Campanella and Mitchell [8] proposed a thermo-porous-mechanical model by using concepts of thermoelasticity and linear elasticity. However, for highly overconsolidated soils, the thermo-porous-mechanical model may no longer be applicable. Based on the unified hardening model established by Yao and Zhou [25], Wang et al. [26] established a calculation method of thermal pore water pressure including *OCR*, but when the soil is in highly overconsolidated state, there is a large gap between the prediction results and the experimental results. In addition, the acquisition of thermal parameters in this calculation method requires additional thermal tests.

In summary, various methods for calculating thermal pore water pressure have been developed. However, the overconsolidation effect has not been well explored. To conveniently and quickly predict the thermal pore water pressure in overconsolidated clay and quantify overconsolidation effect on the thermal pore water pressure, by introducing the parameter Λ affected by *OCR* and the nonlinear relationship between *OCR* and the thermal pore water pressure, a calculation method of thermal pore water pressure considering overconsolidation effect for saturated clay is proposed. In addition, the calculation method is applied to predict the thermal pore water pressure, and the predicted results are compared with experimental data.

2. Calculation Method of Thermal Pore Water Pressure with Different *OCR*

Campanella and Mitchell [8] developed a calculation model of thermal pore water pressure in saturated clay during an undrained heating test:

$$\Delta u_T = \frac{n(\alpha_w - \alpha_s) + \alpha_s T}{m_v} \Delta T \quad (1)$$

in which Δu_T (kPa) is the change of pore pressure caused by thermal loading, n is the porosity, m_v (kPa^{-1}) is the compressibility of soil skeleton, ΔT ($^{\circ}\text{C}$) is the change in temperature, α_{sT} ($^{\circ}\text{C}^{-1}$) is the physicochemical coefficient of structural volume change, and α_w ($^{\circ}\text{C}^{-1}$) and α_s ($^{\circ}\text{C}^{-1}$) are the volumetric expansion coefficients of pore water and soil particles, respectively.

Under undrained heating conditions, saturated soil will expand along the secondary compression curve, and the compressibility of soil skeleton can be estimated by the isotropic recompression curve and written as

$$m_v \approx (m_v)_r = \frac{1}{1 + e_0} \frac{\kappa}{p'} \tag{2}$$

in which e_0 is the initial void ratio, κ is the slope of the isotropic recompression line, p' is the mean effective stress, and $(m_v)_r$ is the compressibility of the soil skeleton determined from the recompression curves.

Substituting Equation (2) into Equation (1) results in

$$\Delta u_T = \frac{n(\alpha_w - \alpha_s) + \alpha_{sT}(1 + e_0)p'\Delta T}{\kappa} \tag{3}$$

For most soils, the values of α_w and α_s are usually taken as 1.7×10^{-4} ($^{\circ}\text{C}^{-1}$) and 3.5×10^{-5} ($^{\circ}\text{C}^{-1}$), respectively [8,9,12,27].

Since the change of porosity during undrained heating tests is generally negligible and has little effect on the thermal pore water pressure, the porosity (n) is approximately equal to the initial porosity (n_0) [9,28].

The physicochemical coefficient α_{sT} is often used to characterize the volume change caused by soil structural rearrangement under unit thermal loading, which is not straightforward to obtain [8,9]. In fact, α_{sT} can be estimated from experimental data of Δu_T at a given ΔT , and the relationship is rearranged as [9]

$$\alpha_{sT} = \left[\frac{\Delta u_T}{p'_0} \frac{\kappa}{1 + e_0} \frac{1}{\Delta T} \right] - n(\alpha_w - \alpha_s) \tag{4}$$

where p'_0 (kPa) is the initial mean effective stress.

Because Equation (4) needs to know the experimental data of Δu_T , the undrained heating test must be carried out. To avoid complicated heating tests, Ghaaowd et al. [9] proposed an empirical expression for the physicochemical coefficient of normally consolidated clay, which can be written as

$$\alpha_{sT} = 1.0 \times 10^{-4} e^{-0.014I_p} \tag{5}$$

where I_p is soil plasticity index and e is the Napierian base.

In addition, through undrained heating tests, Wang et al. [26] found that the thermal pore water pressure of normally consolidated and overconsolidated soil meets

$$\Delta u_{Tocr} = \ln\left(1 + \frac{1.717}{OCR}\right)\Delta u_T \tag{6}$$

where Δu_{Tocr} is the thermal pore water pressure of the overconsolidated soil.

Substituting Equation (3) into Equation (6) results in

$$\Delta u_{Tocr} = \ln\left(1 + \frac{1.717}{OCR}\right) \frac{n(\alpha_w - \alpha_s) + \alpha_{sT}(1 + e_0)p'\Delta T}{\kappa} \tag{7}$$

According to Equation (7), it can be seen that κ is a key parameter for estimating thermal pore water pressure. However, compared to the slope of the isotropic recompression line, the slope of the isotropic compression line (λ) is more commonly adopted in studies

to calculate thermal pore water pressure. Therefore, the value of Λ is used to estimate κ . Meanwhile, according to the Cam-Clay model, it can be known that the compression index, C_c , and Λ , and the rebound index, C_s , and κ satisfy, respectively,

$$\kappa = 0.434C_s \tag{8}$$

$$\Lambda = 0.434C_c \tag{9}$$

Assuming that the ratio of Λ and κ is Λ , the below equation can be obtained:

$$\Lambda = \frac{\Lambda}{\kappa} = \frac{C_c}{C_s} \tag{10}$$

For normally consolidated clays, Λ is generally constant, and the range of Λ is about 4.8~10 [9,29–31]. However, the stress history can affect the value of Λ [32–34] and then change the magnitude of the thermal pore water pressure. In order to better reflect the influence of stress history on thermal pore water pressure, the relationship between rebound index C_s and OCR is introduced [32]:

$$C_s = 0.0213\ln(OCR) + 0.0288 \tag{11}$$

Substituting Equation (10) into Equation (7) results in

$$\Delta u_{Tocr} = \ln\left(1 + \frac{1.717}{OCR}\right) \frac{n(\alpha_w - \alpha_s) + \alpha_s T}{\Lambda} (1 + e_0) \Lambda p' \Delta T \tag{12}$$

Equation (12) is the final calculation method of thermal pore water pressure applicable to both normally consolidated and overconsolidated clays. This calculation method can not only consider the direct weakening effect of OCR, but also the influence of the variation Λ with OCR on thermal pore water pressure.

3. Validation of the Calculation Method

The calculation method of thermal pore water pressure, which can consider overconsolidation effect, was applied to predict the variation of thermal pore water pressure, and the predicted results are compared with the experimental data.

3.1. Comparison with the Experimental Data in Undrained Heating Test of Wang et al. (2017)

To investigate the influence of OCR on thermal pore water pressure under undrained conditions, Wang et al. [26] used a temperature-controlled GDS triaxial testing apparatus to conduct undrained heating tests on normally consolidated and overconsolidated kaolin clays. During the test, saturated kaolin clay was consolidated at a pressure of 300 kPa. After consolidation was completed, the consolidation pressure was unloaded to 150 kPa, 100 kPa, 75 kPa, 37.5 kPa, 30 kPa, and 10 kPa to obtain soil samples with OCR of 1, 2, 3, 4, 8, 10, and 30. Subsequently, the obtained soil samples were used to carry out undrained heating tests. Furthermore, the physical parameters of kaolin clay are shown in Table 1.

Table 1. Physical parameters of kaolin clay obtained from the test of Wang et al. (2017).

θ (%)	S_r	G_s	I_p	Λ	κ	n_0
59–61	98	2.72	27	0.17	0.026	0.63

Through calculation, it has been found that when the clay is in slightly overconsolidated state ($1 < OCR \leq 4.3$), the Λ obtained by Equations (10) and (11) is larger than that of normally consolidated clay. In this case, the value of Λ adopts that of normally consolidated clay. However, for highly overconsolidated clays ($OCR > 4.3$), the values of Λ are different from those of normally consolidated clays, and when OCR of soil is 8, 10, and 30, the calculated values of Λ are 5.4, 5.0, and 3.8, respectively. Thus, it can be seen

that for saturated clays, there is a critical threshold of OCR that determines whether the stress history will change the calculated value of Λ , thereby reducing the thermal pore water pressure. In this paper, the critical threshold of OCR is taken as 4.3. Subsequently, Λ is brought into Equation (12) to predict the thermal pore water pressure. The predicted results and their comparison with the experimental results of Wang et al. [26] are presented in Figure 1.

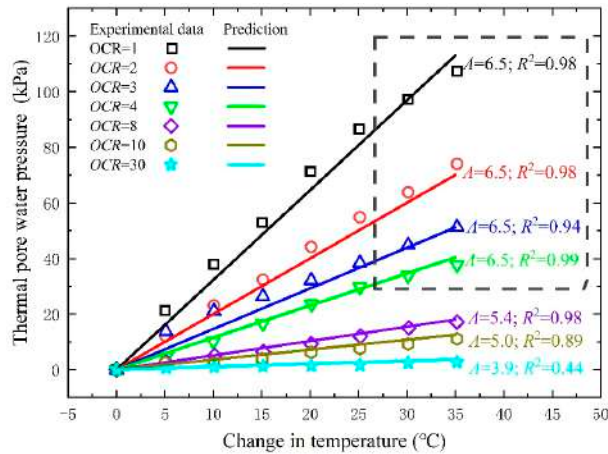


Figure 1. Comparison of predicted thermal pore water pressure against the results of Wang et al. (2017).

It can be seen from Figure 1 that all experimental data points are basically on the predicting lines. Meanwhile, through calculation, it has been found that except for the predicted results with OCR equal to 30, the coefficients of determination (R^2) of other predicted results are all greater than or equal to 0.89. Moreover, it should be noted that when OCR is equal to 30, although the coefficient of determination of the predicted results is only 0.44, the maximum difference between the predicted results and the experimental data is within 1 kPa, which is acceptable in engineering. Therefore, it can be concluded that the calculation method established in this paper can accurately predict the undrained thermal pore water pressure for both normally consolidated and overconsolidated clays.

3.2. Comparison with the Experimental Data in Undrained Heating Test of Abuel-Naga et al. (2007)

Using modified oedometer and triaxial test apparatus, Abuel-Naga et al. [10] carried out undrained heating tests on soft Bangkok clay to study the thermal pore water pressures under different stress conditions. To obtain soils with different overconsolidation ratios, the consolidation pressure of 200 kPa was unloaded to 100 kPa and 50 kPa. The physical parameters of soft Bangkok clay are shown in Table 2. Meanwhile, although Λ was not reported in this undrained heat test, Ghaaowd et al. [9] found that when $\Lambda = 10$, their model-predicted results and the experimental results of Abuel-Naga et al. [10] fit best, so the value of Λ was taken as 10. Furthermore, since the maximum OCR is 4 and the critical threshold is not reached, the influence of stress history on Λ is ignored.

Table 2. Physical parameters of soft Bangkok clay obtained from Abuel-Naga et al. (2007).

θ (%)	S_r	G_s	I_p	Λ	n_0
90–95	98	2.68	60	0.46	0.63

The predicted results of Equation (12) are compared with the experimental results of Abuel-Naga et al. [10], and the comparison results are shown in Figure 2.

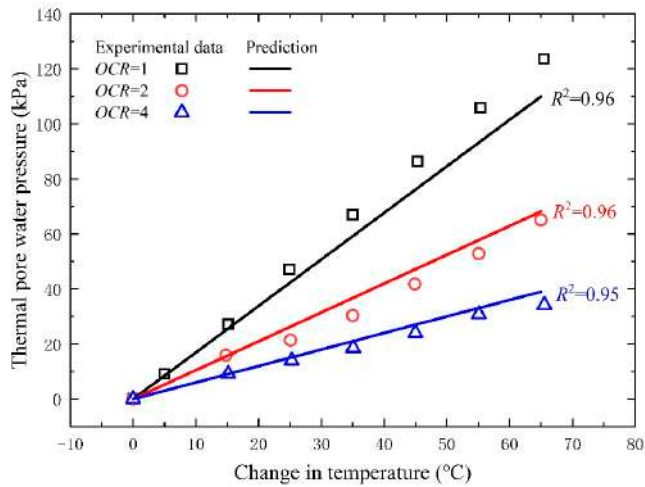


Figure 2. Comparison of predicted thermal pore water pressure against the results of Abuel-Naga et al. (2007).

From Figure 2, it can be observed that all experimental data points are around the predicting lines. In addition, through calculation, it was found that the coefficients of determination (R^2) of all predicted results are 0.95 or above, which indicates that the predicted results are highly consistent with the experimental results. The consistency between the predicted results and the experimental results ensures the accuracy of the calculation method established in this paper.

4. Application of the Calculation Method

In this section, the calculation method is applied to investigate the influence of over-consolidation effect on thermal pore water pressure using MATLAB software. The consolidation pressure is fixed at 300 kPa, and thermal loadings are taken as 35 °C, 50 °C, 65 °C, and 80 °C, respectively. Furthermore, the required parameters for numerical calculation are the same as those in Table 1. The evolution law of thermal pore water pressure with OCR under different thermal loadings is shown in Figure 3.

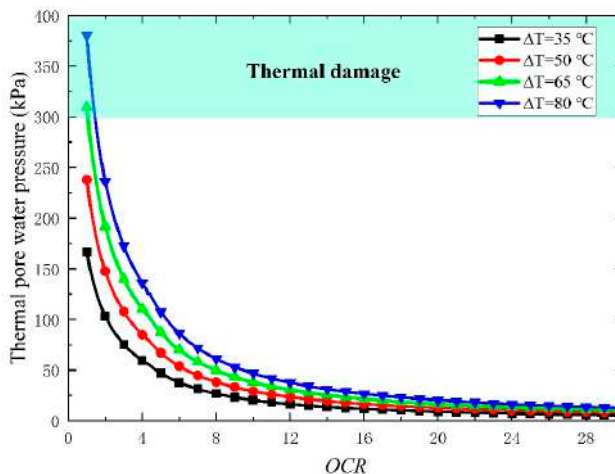


Figure 3. Evolution of the thermal pore water pressure with OCR under different thermal loadings.

From Figure 3, it can be observed that the value of thermal pore water pressure drops sharply with increasing OCR. Meanwhile, the difference of thermal pore water pressure under different thermal loadings also decreases gradually. This is mainly because the thermal pore water pressure is generated by the difference in thermal expansion characteristics of soil particles and pore water, and the degree of overconsolidation of soil can reduce this difference of thermal expansion. In addition, it can be found from Figure 3 that when thermal loading is large and OCR is small, the value of thermal pore water pressure can exceed the effective stress of the soil. In other words, the soil may suffer thermal damage. In this case, if OCR is properly increased, the thermal pore water pressure will be significantly reduced, thus avoiding the occurrence of thermal damage.

5. Discussion

As mentioned above, OCR can not only directly reduce the thermal pore water pressure (Equation (6)), but it can also change the magnitude of the thermal pore water pressure by affecting the value of Λ (Equations (10) and (11)). However, the effect of OCR on Λ is often ignored in existing calculation methods [9,26], which may be the main reason for overestimating the thermal pore water pressure of highly overconsolidated soil. To quantitatively analyze the effect of Λ on the thermal pore water pressure, two cases are given here, namely, Case 1: the predicted results without considering the variation of Λ ($\Lambda = 6.5$), and their comparison with the experimental results; and Case 2: the predicted results considering the variation of Λ ($\Lambda = 5.4, 5.0, \text{ and } 3.8$), and their comparison with the experimental results. The effect of Λ on the thermal pore water pressure is analyzed by comparing the coincidence between experimental results and predicted results. Figure 4a,b show the comparison of experimental results and predicted results for the two cases.

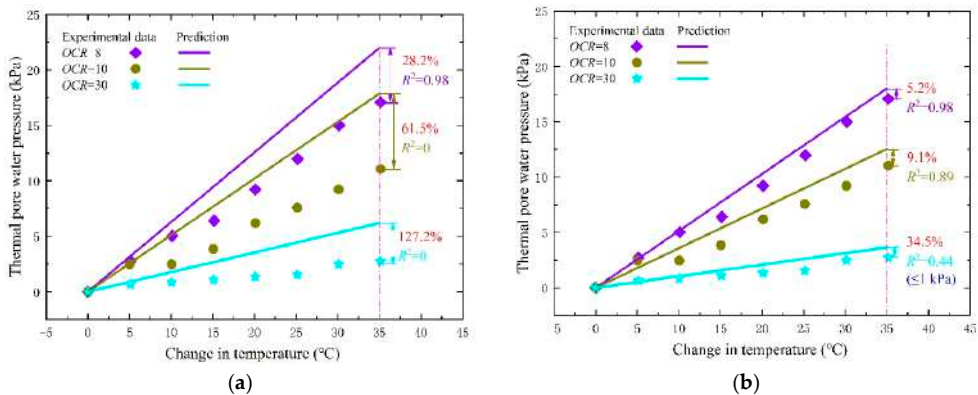


Figure 4. Comparison between experimental results and predicted results of (a) Case 1; (b) Case 2.

From Figure 4a, it can be observed that the predicted results without considering the variation of Λ will seriously overestimate the thermal pore water pressure. For clays with OCR equal to 10 and 30, the coefficients of determination (R^2) of predicted results are both 0. When the change in temperature is 35 °C, the difference between the experimental results and predicted results reaches 61.5% for the clay with OCR equal to 10, and the difference reaches 127.2% for the clay with OCR equal to 30. However, from Figure 4b, it can be found that the coincidence between the predicted results considering the variation of Λ and experimental results was greatly improved. Especially, when OCR is equal to 30, the accuracy of the predicted results was improved by 92.7%, which means that the variation of Λ with OCR cannot be ignored when predicting the thermal pore water pressure inside the highly overconsolidated clay.

6. Conclusions

In this study, by considering the effect of *OCR* on the parameter Λ and the nonlinear relationship between *OCR* and the thermal pore water pressure, a calculation method of thermal pore water pressure considering overconsolidation effect for saturated clay is proposed. Compared with previous calculation methods, the proposed calculation method has higher accuracy and the required parameters are easy to obtain. Moreover, through applying the calculation method and comparing the predicted results of the calculation method with the experimental data, the following conclusions can be drawn:

- Based on the proposed calculation method, the critical threshold of *OCR* (4.3) for determining whether the value of Λ will vary with *OCR* is obtained. When the clay is in slightly overconsolidated state, i.e., $1 < OCR \leq 4.3$, the value of Λ is the same as that of normally consolidated clay. However, when the clay is in a highly overconsolidated state, i.e., $OCR > 4.3$, the value of Λ of overconsolidated clay is smaller than that of normally consolidated clay, and gradually decreases with the increase of *OCR*.
- The proposed calculation method can accurately predict the evolution of thermal pore water pressure under undrained conditions, and is supported by some undrained heating test results of overconsolidated saturated clay, which can provide a theoretical basis for the design of thermo-active structures.
- The effect of *OCR* on thermal pore water pressure is related to the heating rate. However, the calculation method proposed in this study does not consider the influence of heating rate. The follow-up work can explore the comprehensive effects of *OCR* and heating rate on the thermal pore water pressure under undrained conditions theoretically and experimentally.

Author Contributions: Conceptualization, Z.Z.; methodology, Z.Z.; validation, Z.Z. and G.T.; formal analysis, Z.Z. and G.T.; investigation, Z.Z. and G.T.; writing—original draft preparation, Z.Z. and G.T. All authors have read and agreed to the published version of the manuscript.

Funding: This research was funded by the Second Tibetan Plateau Scientific Expedition and Research (STEP) Program (No. 2019QZKK0905).

Informed Consent Statement: Not applicable.

Data Availability Statement: Data are contained within the article.

Acknowledgments: Zhihong Zhang is supported by the Second Tibetan Plateau Scientific Expedition and Research (STEP) Program (No. 2019QZKK0905).

Conflicts of Interest: The authors declare no conflict of interest.

References

1. Abuel-Naga, H.M.; Bergado, D.T.; Ramana, G.V.; Grino, L. Experimental evaluation of engineering behavior of soft Bangkok clay under elevated temperature. *J. Geotech. Geoenviron. Eng.* **2006**, *132*, 902–910. [[CrossRef](#)]
2. Monfared, M.; Sulem, J.; Delage, P.; Mohajerani, M. On the THM behaviour of a sheared Boom clay sample: Application to the behaviour and sealing properties of the EDZ. *Eng. Geol.* **2012**, *124*, 47–58. [[CrossRef](#)]
3. Cheng, W.; Hong, P.Y.; Pereira, J.M.; Cui, Y.J.; Tang, A.M.; Chen, R. Thermo-elasto-plastic modeling of saturated clays under undrained conditions. *Comput. Geotech.* **2020**, *125*, 103688. [[CrossRef](#)]
4. Abuel-Naga, H.M.; Lorenzo, G.A.; Bergado, D.T. Current state of knowledge on thermal consolidation using prefabricated vertical drains. *Geotech. Eng. J. SEAGS AGSSEA* **2013**, *44*, 132–141.
5. Pothiraksanon, C.; Bergado, D.T.; Abuel-Naga, H.M. Full-scale embankment consolidation test using prefabricated vertical thermal drains. *Soils Found.* **2010**, *50*, 599–608. [[CrossRef](#)]
6. Brochard, L.; Honorio, T. Thermo-poro-mechanics under adsorption applied to the anomalous thermal pressurization of water in undrained clays. *Acta Geotech.* **2021**, *24*, 2713–2727. [[CrossRef](#)]
7. Li, H.; Kong, G.; Wen, L.; Yang, Q. Pore pressure and strength behaviors of reconstituted marine sediments involving thermal effects. *Int. J. Geomech.* **2021**, *21*, 06021008. [[CrossRef](#)]
8. Campanella, R.G.; Mitchell, J.K. Influence of temperature variations on soil behavior. *J. Soil Mech. Found. Div.* **1968**, *94*, 709–734. [[CrossRef](#)]

9. Ghaaowd, I.; Takai, A.; Katsumi, T.; McCartney, J.S. Pore water pressure prediction for undrained heating of soils. *Environ. Geotech.* **2015**, *4*, 70–78. [[CrossRef](#)]
10. Abuel-Naga, H.M.; Bergado, D.T.; Bouazza, A. Thermally induced volume change and excess pore water pressure of soft Bangkok clay. *Eng. Geol.* **2007**, *89*, 144–154. [[CrossRef](#)]
11. Ghabezloo, S.; Sulem, J. Stress dependent thermal pressurization of a fluid-saturated rock. *Rock Mech. Rock Eng.* **2009**, *42*, 1. [[CrossRef](#)]
12. Burghignoli, A.; Desideri, A.; Miliziano, S. A laboratory study on the thermomechanical behavior of clayey soils. *Can. Geotech. J.* **2000**, *37*, 764–780. [[CrossRef](#)]
13. McCartney, J.S. Thermal volume change of unsaturated silt under different stress states and suction magnitudes. *E3S Web Conf. EDP Sci.* **2016**, *9*, 09009. [[CrossRef](#)]
14. Bai, B.; Yang, G.C.; Li, T.; Yang, G.S. A thermodynamic constitutive model with temperature effect based on particle rearrangement for geomaterials. *Mech. Mater.* **2019**, *139*, 103180. [[CrossRef](#)]
15. Bing, B.; Yan, W.; Dengyu, R.; Fan, B. The effective thermal conductivity of unsaturated porous media deduced by pore-scale SPH simulation. *Front. Earth Sci.* **2022**, *10*, 943853.
16. Bai, B.; Zhou, R.; Cai, G.Q.; Hu, W.; Yang, G.C. Coupled thermo-hydro-mechanical mechanism in view of the soil particle rearrangement of granular thermodynamics. *Comput. Geotech.* **2021**, *137*, 104272. [[CrossRef](#)]
17. Liu, Q.; Deng, Y.B.; Mao, W.Y.; Deng, Y.B. The influence of over consolidation ratio on thermal consolidation properties of clay. *J. Disaster. Prev. Mitigation. Eng.* **2019**, *39*, 607–614.
18. Cekerevac, C.; Laloui, L. Experimental study of thermal effects on the mechanical behaviour of a clay. *Int. J. Numer. Anal. Methods Geomech.* **2004**, *28*, 209–228. [[CrossRef](#)]
19. Di Donna, A.; Laloui, L. Response of soil subjected to thermal cyclic loading: Experimental and constitutive study. *Eng. Geol.* **2015**, *190*, 65–76. [[CrossRef](#)]
20. Houhou, R.; Sutman, M.; Sadek, S.; Laloui, L. Microstructure observations in compacted clays subjected to thermal loading. *Eng. Geol.* **2021**, *287*, 105928. [[CrossRef](#)]
21. Baldi, G.; Hueckel, T.; Pellegrini, R. Thermal volume changes of the mineral-water system in low-porosity clay soils. *Can. Geotech. J.* **1988**, *25*, 807–825. [[CrossRef](#)]
22. Towhata, I.; Kuntiwattanakul, P.; Seko, I.; Ohishi, K. Volume change of clays induced by heating as observed in consolidation tests. *Soils Found.* **1993**, *33*, 170–183. [[CrossRef](#)]
23. Sultan, N.; Delage, P.; Cui, Y.J. Temperature effects on the volume change behavior of boom clay. *Eng. Geol.* **2002**, *64*, 135–145. [[CrossRef](#)]
24. Hueckel, T.; Borsetto, M. Thermoplasticity of saturated soils and shales: Constitutive equations. *J. Geotech. Eng.* **1990**, *116*, 1765–1777. [[CrossRef](#)]
25. Yao, Y.P.; Zhou, A.N. Non-isothermal unified hardening model: A thermo-elasto-plastic model for clays. *Geotech.* **2013**, *63*, 1328–1345. [[CrossRef](#)]
26. Wang, K.J.; Hong, Y.; Wang, L.Z.; Li, L.L. Effect of heating on the excess pore water pressure of clay under undrained condition. *Chin. J. Rock Mech. Eng.* **2017**, *36*, 2288–2296.
27. Takai, A.; Ghaaowd, I.; McCartney, J.S.; Katsumi, T. Impact of drainage conditions on the thermal volume change of soft clay. *Geo-Chicago* **2016**, *2016*, 32–41.
28. Uchaipichat, A.; Khalili, N. Experimental investigation of thermo-hydro-mechanical behaviour of an unsaturated silt. *Geotech.* **2009**, *59*, 339–353. [[CrossRef](#)]
29. Schofield, A.; Wroth, P. *Critical State Soil Mechanics*; McGraw-Hill: London, UK, 1973.
30. Lou, X.M.; Li, D.N.; Yang, M. Statistical analysis for rebound deformation parameters of silty clay at bottom of deep excavation in Shanghai. *J. Tongji Univ.* **2012**, *40*, 535–540.
31. He, P.; Wang, W.D.; Xu, Z.H. Empirical correlations of compression index and swelling index for Shanghai clay. *Rock. Soil. Mech.* **2018**, *39*, 3773–3782.
32. Zhou, K.; Sun, D.A. Experiments on compression characteristics of remoulded soft clay in shanghai. *J. Shanghai Univ.* **2009**, *15*, 99–104.
33. Shi, W.; Wang, J.; Guo, L.; Hu, H.T.; Jin, J.Q.; Jin, F.Y. Undrained cyclic behavior of overconsolidated marine soft clay under a traffic-load-induced stress path. *Mar Georesour. Geotechnol.* **2018**, *36*, 163–172. [[CrossRef](#)]
34. Wang, J.; Zhuang, H.; Guo, L.; Wu, T.Y.; Yuan, Z.H.; Sun, H.L. Secondary compression behavior of over-consolidated soft clay after surcharge preloading. *Acta Geotech.* **2022**, *17*, 1009–1016. [[CrossRef](#)]

Article

Experimental Study on the Shear Strength of Silt Treated by Xanthan Gum during the Wetting Process

Junran Zhang *, Zhihao Meng, Tong Jiang, Shaokai Wang, Jindi Zhao and Xinxin Zhao

Henan Province Key Laboratory of Geomechanics and Structural Engineering, North China University of Water Resources and Electric Power, Zhengzhou 450045, China; z20201020288@stu.ncwu.edu.cn (Z.M.); jiangtong@ncwu.edu.cn (T.J.); wangshaokai@ncwu.edu.cn (S.W.); x201810207162@stu.ncwu.edu.cn (J.Z.); zhaoxinxin@ncwu.edu.cn (X.Z.)

* Correspondence: zhangjunran@ncwu.edu.cn; Tel.: +86-15890092736

Abstract: Traditional materials such as fly ash and lime are generally used to improve soils but can severely pollute the environment. Eco-friendly protocols, such as the application of xanthan gum, are therefore essential for soil treatment. In this study, a series of microscopic tests, water retention characteristics tests, and shear tests were carried out on silt, which are known to have poor engineering properties, to explore the effect and mechanism of xanthan gum treatment on the water retention and shear strength characteristics of silt during the wetting process. The results show that the water retention capacity of the treated silt increases with increasing xanthan gum content, and a hysteresis effect is clearly observed. The cohesion and internal friction angle of the silt strongly decrease with increasing water content, and the strength significantly weakens. However, the strength of the silt treated with xanthan gum is consistently higher than that of the untreated silt. The microscopic tests show that soil pores are gradually filled by xanthan gum with good water-retaining properties, thus significantly enhancing the water retention capacity. Furthermore, the hydrogel that cements the soil particles forms by the bonding effects between xanthan gum and soil particles, which greatly improves the silt strength.

Citation: Zhang, J.; Meng, Z.; Jiang, T.; Wang, S.; Zhao, J.; Zhao, X. Experimental Study on the Shear Strength of Silt Treated by Xanthan Gum during the Wetting Process. *Appl. Sci.* **2022**, *12*, 6053. <https://doi.org/10.3390/app12126053>

Academic Editor: Bing Bai

Received: 19 May 2022

Accepted: 13 June 2022

Published: 14 June 2022

Publisher's Note: MDPI stays neutral with regard to jurisdictional claims in published maps and institutional affiliations.



Copyright: © 2022 by the authors. Licensee MDPI, Basel, Switzerland. This article is an open access article distributed under the terms and conditions of the Creative Commons Attribution (CC BY) license (<https://creativecommons.org/licenses/by/4.0/>).

Keywords: xanthan gum; silt; water retention capacity; strength; wetting process; microscopic tests

1. Introduction

Soil treatment measures (e.g., cement, lime, fly ash) are commonly used to improve the strength and water retention capacity of soils [1]. Traditional materials such as Portland cement have long been used in geotechnical engineering to treat soil, but a large amount of CO₂ is emitted during the production process of cement and lime [2]. One ton of Portland cement production has been shown to release approximately one ton of CO₂, and one ton of lime output releases approximately 0.86 tons of CO₂ [3]. Alternative materials, such as metakaolin and calcium hydroxide mixtures, alkaline aluminosilicate minerals, and fly ash-based inorganic polymer concrete, have therefore emerged to control and reduce carbon emissions [4–6]. Microbial soil treatment not only protects the ecological environment by controlling carbon emissions compared with traditional and inorganic methods but also significantly improves the strength and ductility of treated soils [7]. Microbial technology, namely biopolymers, has been applied to improve soil mass. For example, the unconfined compressive strength of 0.5% biopolymer was shown to be higher than that of 10% cement after treatment. The large-scale commercialization of biopolymers has good economic feasibility due to the high cost of cement in less-developed countries and can help improve the strength and durability of geotechnical engineering [8]. Driven by this huge catalytic potential and differing from traditional geotechnical engineering soil treatment technology, improved microbial soil treatment technology has been explored, including microbial and inanimate microbial improvement technology.

Since the onset of the 21st century, a series of studies have addressed different kinds of microbial technologies for soil treatment: synthetic hydrophilic polyacrylamide additives can improve the strength and stability of different soils [9]; casein and sodium caseinate biopolymers can improve the strength of sand [10]; the Panstrains of Enterobacteriaceae cultivated by cell-free fermentation liquid can stabilize soil [11]; and microbial-induced calcium precipitation technology (MICP) can strengthen and stabilize soil [12]. Recent studies showed that biopolymers could produce hydrogels and induce a pore-blocking effect, which can significantly reduce the permeability, whereas calcite precipitated by MICP does not have such a strong pore-blocking effect [13]. Inanimate microbial technology does not require a strict culture environment and offers greater advantages in enhancing the water stability of soil. Inanimate microbial technology can also produce hydrogel colloid and promote the transport of heavy metals in contaminated soil to improve the soil and protect the environment [14].

Numerous suitable biopolymers for soil improvement have emerged in recent years, and biopolymers have become popularized in engineering. For example, the commercial, large-scale production of composite fiber polymer has been applied [15], and the polymer lignin is widely used in manufacturing industries [16,17]. Polyacrylamide polymers have been widely used in the United States to irrigate land and control sand erosion and runoff protection, as well as to construct helicopter landing pads to reduce dust pollution [10]. Recent studies showed that gellan gum and agar gum could significantly improve soil durability [18], that xanthan gum can maintain water for vegetation growth in the soil to prevent desertification [19], and that both xanthan gum and gellan gum can improve the dynamic characteristics of sand [20]. Adding a small amount of biopolymer can greatly improve the soil strength, and guar gum is more advantageous for treating collapsible soil and clay using the wet mixing method, but xanthan gum is superior when treating silty fine-grained soil [21–23]. Xanthan gum can be used as a stabilizer for slope protection in geotechnical engineering. Xanthan gum also has a low application cost and very competitive price compared with other biopolymers [24].

In the late 20th century, Wallingford and Sanchez pointed out that xanthan gum is more capable of absorbing water than other polysaccharide polymers [25,26]. Xanthan gum can be used to effectively improve the water retention capacity of engineering soil, such as through hydraulic seepage barriers and underground pollution stabilization [14,24,27]. Zhou et al. [28] verified that xanthan gum significantly enhances the water retention of soil. Because xanthan gum can separate soil particles and fill soil pores, the pores of sand become larger [29], and its water retention performance is very strong [30], thus improving the water retention capacity of the soil.

Ayeldeen and Qureshi et al. [21,31] indicated that the addition of xanthan gum could improve the collapsibility resistance of collapsible soil, as well as the water disintegration resistance and strength of sandy soil. Cabalar et al. [32] showed that the compaction degree, viscosity, and strength of clays treated with xanthan gum were enhanced at low water content. Chang et al. [33] found that the unconfined compressive strength (UCS) of drying soil tended to stabilize upon increasing the xanthan gum content to a certain range. According to the UCS test results of Latifi [34], stability can be achieved by adding xanthan gum to bentonite and kaolinite at low water content. Soldo et al. [35] found that the strength of soil with 2% xanthan gum content is close to the maximum at low water content. Soldo and Sujatha et al. [36,37] indicated that water content is an important factor affecting soil strength and that the strength of silty sand and silt treated with xanthan gum is greatly improved at low water content. Engineering soil must usually be cured for a few days to reach a low water content state. Because the water content of engineering soil is low, the soil strength is generally high but easily affected by rainfall infiltration, which can reduce the soil strength and stability. Most soil treatment studies conducted strength tests in the range of high suction, but few tests have focused on soil strength over the entire range of water content of soil treated by xanthan gum. Recent studies showed a significant decrease in the wetting strength of sand after treatment with biopolymer

guar gum [38]. However, for sand treated with xanthan gum, the wetting strength was greater than the initial strength [39]. Based on the above research results, further in-depth tests were carried out to systematically study the influence of xanthan gum on the wetting strength characteristics of silt over the full range of water content.

The objective of this study was to investigate the effect and mechanism of the strength weakening characteristics of silt treated with xanthan gum (XG-silt) during the wetting process. A series of microscopic tests, water retention characteristics tests, and direct shear tests were carried out on XG-silt using scanning electron microscopy, mercury porosimeter, a WP4C dew point potential meter, and a Shear Trac-II test system. The experimental results qualitatively and quantitatively reveal the variation law and internal mechanism of the wetting strength characteristics of XG-silt, which provides a useful scientific basis for the design and construction of related geotechnical engineering projects.

2. Materials and Methods

2.1. Materials

Figure 1 shows that Henan Province is located in the North China Plain of the middle and lower reaches of the Yellow River, where silt is widely distributed. The silt sample location is at an engineering project in the Xing-yang area, west of Zhengzhou city in northern Henan Province, which adjoins the south bank of the Yellow River. The experimental alluvial silt has poor early strength and water stability [40,41]. Xanthan gum is therefore used to strengthen the silt in the Yellow River flooding area due to the complex engineering properties of silt.

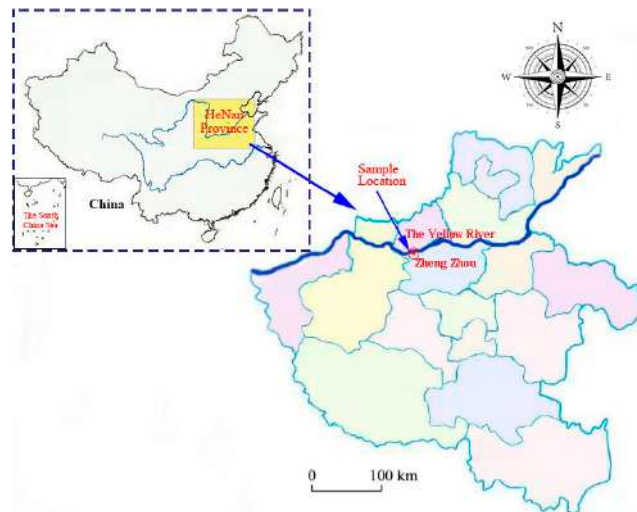
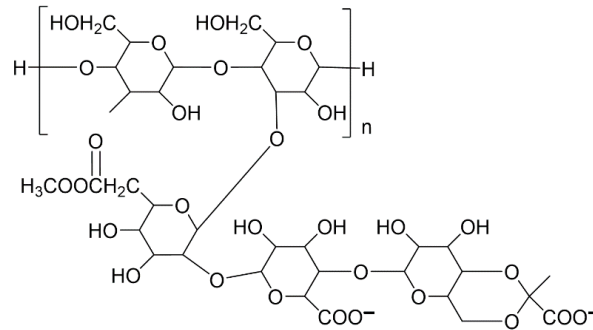


Figure 1. Silt sample location.

Xanthan gum is a high molecular anionic polysaccharide polymer produced by the aerobic fermentation of *Xanthomonas* and carbohydrates. It is carbon neutral, sustainable and reproducible, stable to acid, alkali, and heat, and has excellent compatibility with a variety of salts. It is made from non-food crops at a low cost and can be prepared in large quantities [26]. The xanthan gum used to treat the silt was purchased from Fu Feng Biotechnology Co., Ltd. in Inner Mongolia. The reagent was of food grade and analytical grade. The storage environment conditions were 25 °C and 35% relative humidity. Pictures of the dry silt and xanthan gum are shown in Figure 2.

Table 2. Basic physical properties of xanthan gum.

Product	Grade	Viscosity/CP	Color	State	Shear Performance Value
XG	food grade	1475	light beige	powder	7.7

**Figure 4.** Molecular structure of xanthan gum.

2.2. Methods

2.2.1. Sample Preparation

Soil samples were prepared following the dry method [42], which was commonly used in previous tests. The dried silt powder was fully mixed with dried xanthan gum. Water was then added, and the mixture was stirred evenly. Based on previous experimental studies, the optimal mass ratio (m_{bp}/m_s) of dried XG and dried silt in the water retention characteristics tests was set as 0.0%, 0.5%, 1.0%, 1.5%, and 2.0%, and the optimal mass ratio in the direct shear tests was set as 2.0% [21,33,34,43]. In order to ensure the uniformity of XG-silt, dry soil was stirred and mixed evenly with XG of the corresponding quality. Deionized water was added to form wet soil that avoids the influence of additional chemical components in the water. The soil was then sealed at a constant temperature for 24 h until the water was fully infiltrated. The initial water content of the specimen was 15%, and 92% of the maximum dry density, $\rho_d = 1.63 \text{ g/cm}^3$, was selected as the initial dry density. After specimen preparation, a vacuum pump was used to vacuum and saturate the specimen for testing.

2.2.2. Scanning Electron Microscopy Tests

The specimen was rapidly frozen with liquid nitrogen ($-190 \text{ }^\circ\text{C}$) and vacuum-pumped for 24 h with a vacuum freeze-drying apparatus to ensure the specimen reached the dry state when the water of the specimen was completely sublimated. The dry specimens were then sliced into suitable sheet sizes, and scanning electron microscope (SEM) tests were performed at different magnifications ($\times 50$, $\times 100$, $\times 200$, $\times 500$, $\times 1000$, $\times 2000$, $\times 5000$, and $\times 10,000$) using a JBM-7500F field emission SEM (JEOL, Japan). Only four suitable magnification images ($\times 200$, $\times 2000$, $\times 5000$, and $\times 10,000$) were selected to fully present the results.

2.2.3. Mercury Intrusion Tests

The pores of the soil sample are assumed to be cylindrical. Mercury is non-infiltrating and therefore does not flow into solid pores. Under low pressure, mercury first intrudes into the gaps and large pores, then gradually intrude into the micropores with increasing mercury pressure:

$$P = -2\sigma \cdot \cos \theta / r \tag{1}$$

where P is the mercury intrusion pressure [Pa], r is the pore radius [m], σ is the surface tension of the intrusion liquid, $\sigma = 0.484 \text{ N/m}$, and θ is the contact angle (130°).

2.2.4. Water Retention Characteristics Test

The saturated specimens were dried and wetted at constant humidity and temperature. The suction was intermittently measured using a WP4C dew point water potential meter (Figure 5). The test specimen’s initial size was $d_0 = 33 \text{ mm}$ and $h_0 = 7 \text{ mm}$.



Figure 5. WP4C dewpoint potential meter.

2.2.5. Direct Shear Tests

The size of the test specimen was $d_0 = 64 \text{ mm}$ and $h_0 = 25 \text{ mm}$. Saturated specimens with 0.0% and 2.0% XG content were dried and wetted. The initial water content of the specimens was 22%. The drying and wetting paths of the specimens are shown in Figure 6. The specimens were uniformly dried to a state of 2% water content (drying path AB) and then wetted to a different water content (2%, 4%, 8%, 16%, or 22%). Fast shear tests were then carried out under vertical stresses of 50, 100, and 200 kPa. The automatic direct shear and residual shear test system is shown in Figure 7. The Shear Trac-II test system was operated by computer shear software and the control panel of the shear apparatus to receive immediate feedback on the loads and displacements monitored by the sensors.

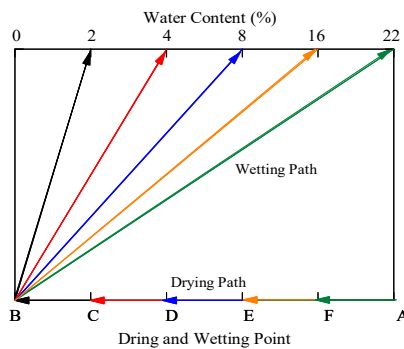


Figure 6. Drying and wetting paths.

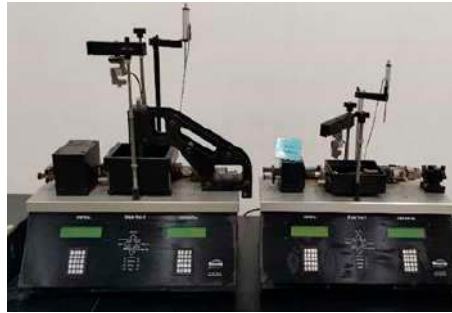


Figure 7. Shear Trac-II test system.

3. Results and Discussion

3.1. SEM Images of Xanthan Gum-Treated Silt

Figures at four suitable magnifications ($\times 200$, $\times 2000$, $\times 5000$, and $\times 10,000$) were present for microscopic analysis. At $\times 200$ magnification, the macroscopic structure of soil particle distribution can be seen. At the magnification of $\times 2000$, $\times 5000$, and $\times 10,000$, the internal microstructure of soil can be clearly observed. The following are the conclusions based on SEM pictures.

Figure 8a–c show the SEM test results of XG-silt at $\times 200$ magnification. The mass cementation between the silt particles and XG becomes increasingly large with increasing XG content.

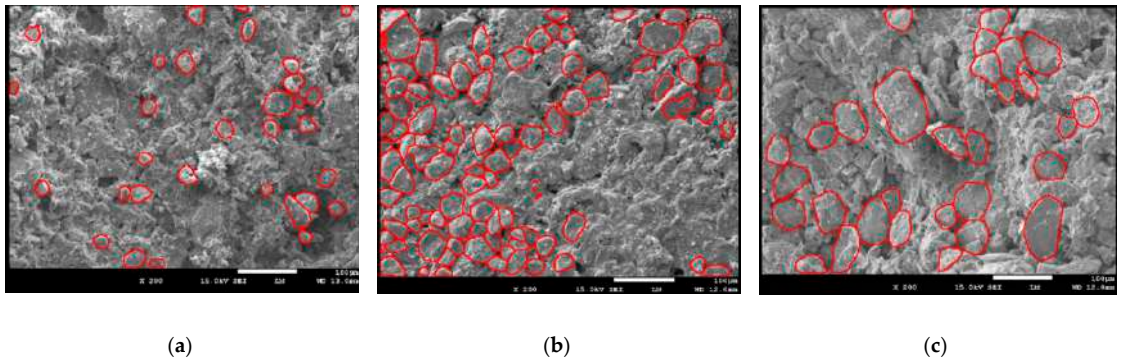


Figure 8. SEM pictures of XG-silt at $\times 200$ magnification: (a) $m_{bp}/m_s = 0\%$; (b) $m_{bp}/m_s = 1.0\%$; (c) $m_{bp}/m_s = 2.0\%$.

Figure 9a–c show the SEM images of XG-silt at $\times 2000$ magnification. The pore diameter decreases with increasing XG content.

Figure 10a–c show the SEM images of XG-silt at $\times 5000$ magnification. A comparison shows that more soil particles bonded together with increasing XG content, and the small particles became soil mass with cementation [44]. The gaps and pores of the samples were also gradually filled with XG with increasing XG content, showing observable cementation, and the samples became increasingly dense.

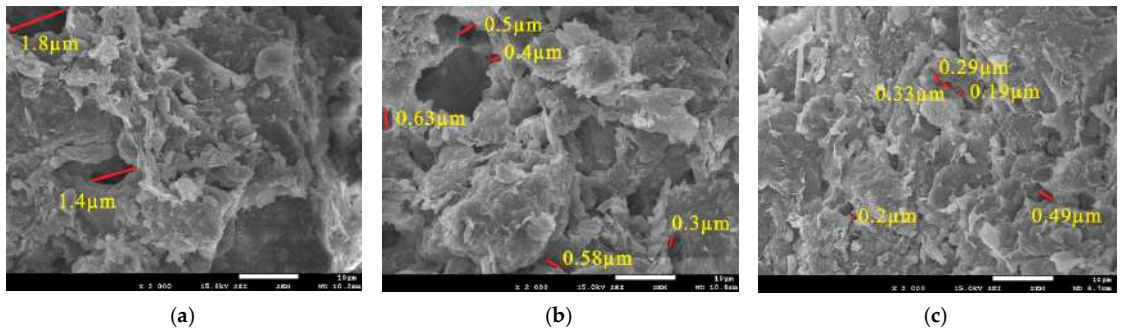


Figure 9. SEM pictures of XG-silt at $\times 2000$ magnification: (a) $m_{bp}/m_s = 0\%$; (b) $m_{bp}/m_s = 1.0\%$; (c) $m_{bp}/m_s = 2.0\%$.

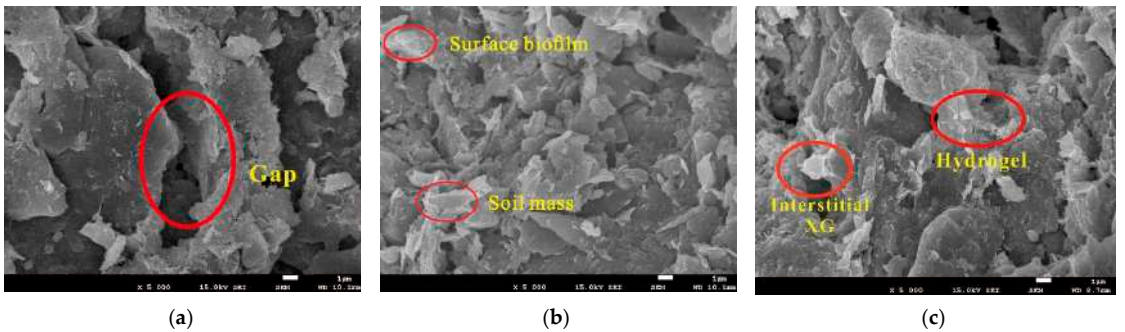


Figure 10. SEM pictures of XG-silt at $\times 5000$ magnification: (a) $m_{bp}/m_s = 0\%$; (b) $m_{bp}/m_s = 1.0\%$; (c) $m_{bp}/m_s = 2.0\%$.

Figure 11a–c show the SEM images of XG-silt at $\times 10,000$ magnification. Part of the XG formed a biofilm covering the surface of soil particles with increasing XG content, and the other part formed bridge connections (biological polymerization chains) between the aggregate gap [21,37,42]. Additionally, the small particle aggregates became larger with closer connections.

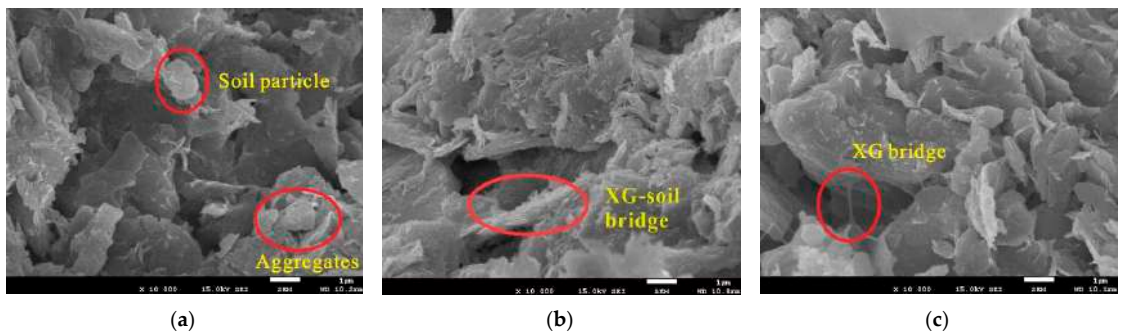


Figure 11. SEM pictures of XG-silt at $\times 10,000$ magnification: (a) $m_{bp}/m_s = 0\%$; (b) $m_{bp}/m_s = 1.0\%$; (c) $m_{bp}/m_s = 2.0\%$.

3.2. Mercury Intrusion Test

The pore size distribution of the treated specimens with different XG contents was investigated, which is helpful in analyzing the interaction between the silt and XG. Figure 12a,b show the cumulative pore size and differential pore size, respectively.

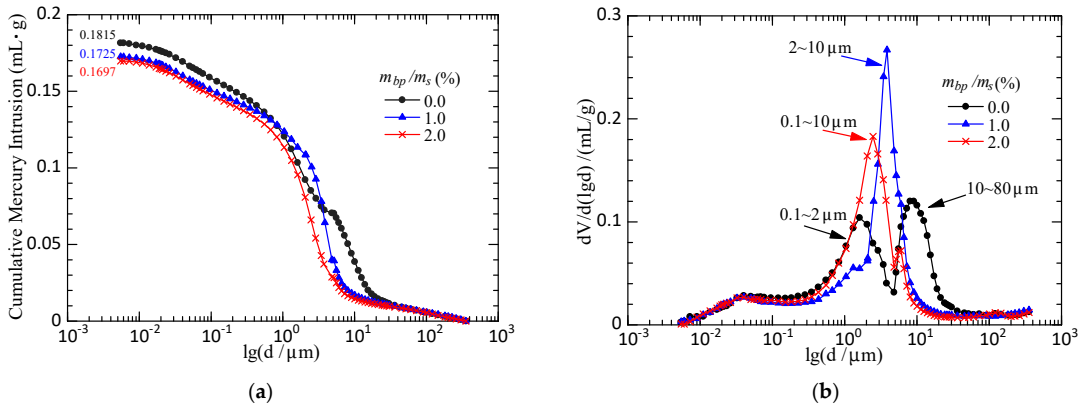


Figure 12. Mercury intrusion pore size distribution: (a) cumulative curves; (b) differential curves.

Kodikara et al. [45] found that there are aggregates in the soil, which leads to different pore sizes. The pore size distribution of soil is therefore generally bimodal and manifested as micropore and macropore peaks. Figure 12a shows that the cumulative pore intrusion of the mercury intrusion test specimens decreases from 0.1815 mL/g for XG-free silt to 0.1697 mL/g for silt with 2% XG, which implies that the pore size distribution decreases with increasing XG content. Figure 12b shows when 1% XG is added to pure silt, the large pores (10–80 μm) are gradually connected by XG hydrogels and reduced to medium pores (2–10 μm). Small pores (0.1–2 μm) in the silt are then filled with XG, and their number gradually decreases. The number of large and small pores in silt, therefore, strongly decreases, while the number of medium pores significantly increases. The pore size distribution of silt also turns into unimodal pore size distribution. Upon increasing the XG content from 1% to 2%, the medium pores in the silt are gradually connected by the filling of XG and hydrogels, resulting in a significant reduction in the number of medium pores and a large increase in the number of small pores.

3.3. Water Retention Characteristics Test

Figure 13 shows the water retention characteristic curve of the XG-silt specimens. Figure 13a,b show the drying and wetting curves, respectively, and Figure 14 shows the drying–wetting hysteresis curve. Figure 13a,b show that the drying curves all shift to the upper right with increasing XG content, which reflects an increase in the water retention capacity of the treated specimens. Especially in the range of low suction, the water retention capacity of the silt significantly increases with increasing XG content. Because XG carries carboxylic acid (–COOH) and hydroxyl (–OH) with a negative charge, it can interact with cations in the soil particles to generate a capillary force, thus absorbing and retaining more water [46].

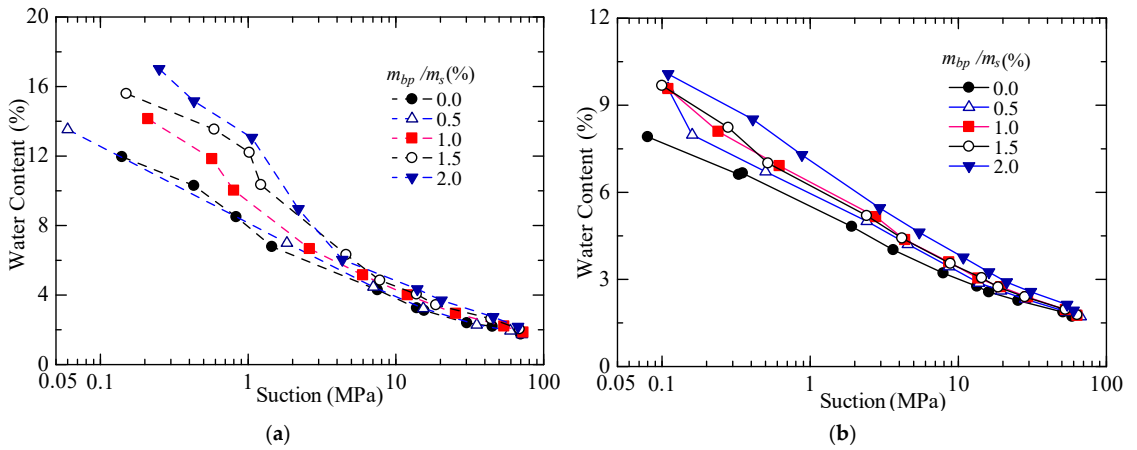


Figure 13. Water retention curves of silt with different XG contents: (a) drying process; (b) wetting process.

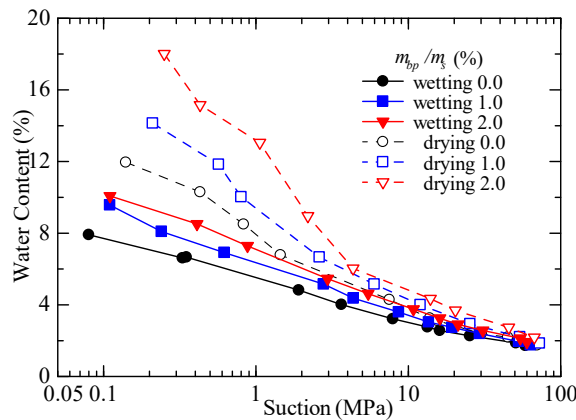


Figure 14. Drying–wetting hysteresis curve of silt with different XG contents.

Figure 14 shows that the water retention capacity of the treated specimens during the drying process is stronger than that during the wetting process, which is related to the water retention hysteretic effect of the soil during drying [47–49]. The hysteretic circle area between the drying and wetting curves of the treated specimens also gradually increases with increasing XG content. The drying and wetting curves of specimens tend to be consistent in the high-suction range [50].

The SEM and mercury intrusion test results show that more biofilms covered the surface of the soil particles with increasing XG content, and the bridging connections are found in the silt pores, which gradually filled with XG. The water retention capacity of the treated silt increased due to the strong water-retaining properties of XG [25,26,29,51], and the hysteretic circle area between the drying and wetting curves also gradually increased. Previous experimental studies show that more water can be retained in soil pores after treatment with XG, which is consistent with the water retention characteristics test results of this study. Additionally, XG has a stronger water retention capacity than other polymers, which can improve the survival rate of vegetation in severely arid areas [19,52].

3.4. Direct Shear Test

3.4.1. Shear Strength Characteristics of Silt

Figure 15 shows the shear strength–displacement relation curves of pure silt with water contents of 2%, 4%, 8%, 16%, and 22%. The peak strength and residual strength of the silt specimens gradually increased with increasing vertical stress.

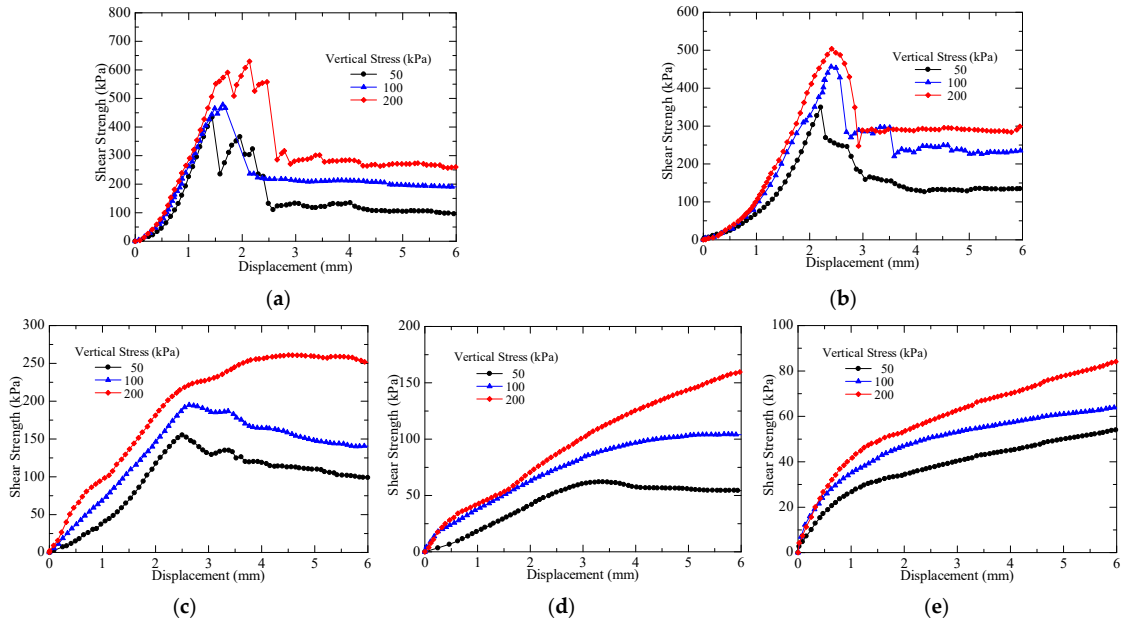


Figure 15. Shear strength of the silt samples with different water contents ($m_{hp}/m_s = 0\%$): (a) $w = 2\%$; (b) $w = 4\%$; (c) $w = 8\%$; (d) $w = 16\%$; (e) $w = 22\%$.

When the water content was 2% and 4%, the shear strength–displacement relation curves of pure silt showed a stress-softening phenomenon, and the peak strength was higher than the residual strength. When the water content was 16% and 22%, the shear strength–displacement relation curves of pure silt showed a stress-hardening phenomenon. When the water content was 8%, and the vertical stress was 50 kPa and 100 kPa, the shear strength–displacement relation curves of pure silt showed a stress-softening phenomenon, and when the vertical stress was 200 kPa, the shear strength–displacement relation curve displayed a stress-hardening phenomenon. The results show that with the increase in vertical pressure, the soil began to show a stress-hardening phenomenon [53,54].

Figure 15c,d show the stress softening into stress hardening of pure silt with water content increasing from 8% to 16%.

3.4.2. Strength Characteristics of Xanthan Gum-Treated Silt

Figure 16 shows the shear strength–displacement relation curves of the XG-silt samples with different water content. The peak strength and residual strength of the treated silt were found to gradually increase with the increase in vertical stress.

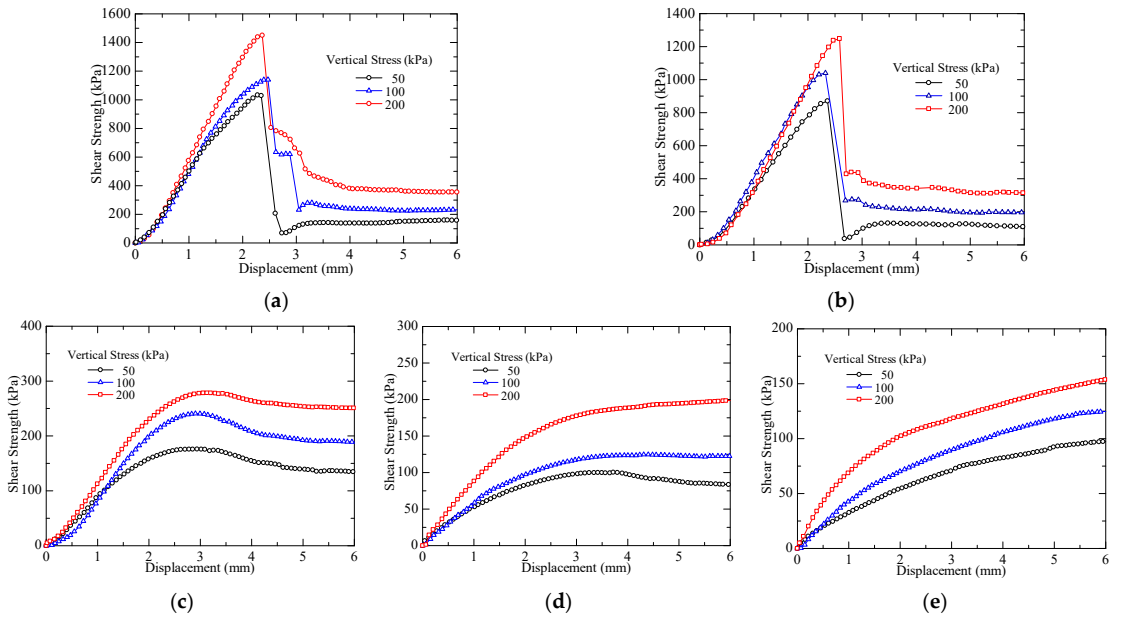


Figure 16. Shear strength of xanthan gum-treated silt with different water contents ($m_{bp}/m_s = 2\%$): (a) $w = 2\%$; (b) $w = 4\%$; (c) $w = 8\%$; (d) $w = 16\%$; (e) $w = 22\%$.

When the water content was 2%, 4%, and 8%, the shear strength–displacement relation curves of the treated silt showed the stress-softening phenomenon. When the water content was 22%, the shear strength–displacement relation curves of the treated silt showed a stress-hardening phenomenon. When the water content was 16%, and the vertical pressure was 50 kPa, the shear strength–displacement relation curve of pure silt showed a stress-softening phenomenon, and when the vertical stress was 100 kPa and 200 kPa, shear strength–displacement relation curves showed a stress-hardening phenomenon.

Figure 16c,d show the stress softening into stress hardening with water content increasing from 8% to 16% after the addition of XG.

3.4.3. Relationship between Strength and Water Content

Figure 17 shows the shear strength–displacement relation curves of the pure silt and XG-silt specimens with different water contents under vertical stress of 100 kPa. The strength of the silt specimens gradually increased with decreasing water content, as did the strength of the XG-silt specimens.

3.4.4. Variation Rules of Shear Strength Parameters

Figure 18 shows the relationship curves of water content, cohesion c , and internal friction angle ϕ of silt. Table 3 summarizes the parameters of the direct shear strength tests before and after silt treatment during the wetting process. Table 3 and Figure 18 show that at low water content (2–4%), the c values of XG-silt increased by more than a factor of 2.3, and ϕ increased by more than a factor of 1.5. However, when the water content was lower than 8%, the sample strength was enhanced both before and after treatment, whereas c and ϕ only slightly increased. At high water contents (16% and 22%), c increased by factors of 1.4 and 1.8 times, respectively, and ϕ increased by factors of 1.4 and 1.9. The experimental results are consistent with those of Soldo et al. [35,36] and Chang et al. [55]. Additionally, the test results showed that the addition of XG can greatly improve the strength and stability of silt during the wetting process.

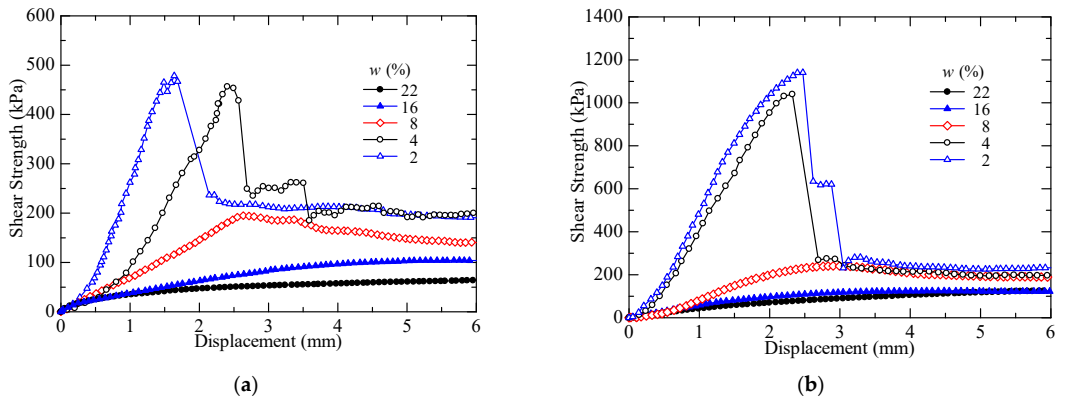


Figure 17. Wetting strength of the silt specimens with different water contents under a vertical stress of 100 kPa: (a) $m_{bp}/m_s = 0\%$; (b) $m_{bp}/m_s = 2\%$.

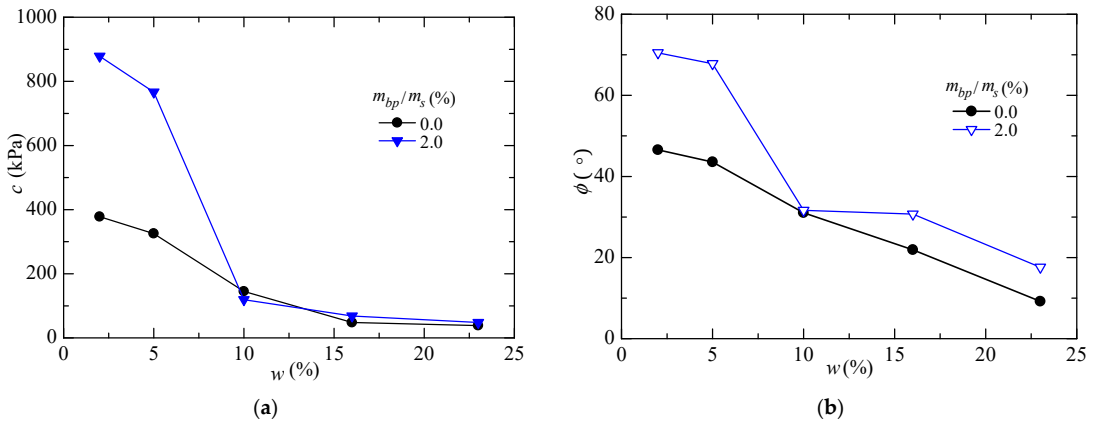


Figure 18. Comparison of shear strength parameters before and after treatment: (a) w - c relation curve; (b) w - ϕ relation curve.

3.4.5. Discussion on Strength Mechanisms

According to the mercury intrusion test result, the pore size distribution of the silt specimen is bimodal. Therefore, in the shear process, the internal stress of the silt specimen is not uniform. By comparing Figures 15a and 16a, it is obvious that the pore structure in the silt greatly affects the shear stress of the soil and thus further affects the strength and stability of the soil in the range of low water content. According to SEM pictures and mercury intrusion test results, with the increase in XG content, the pores of silt are gradually filled with XG cement. Compared with Figures 15 and 16, it can be concluded that the stress-hardening phenomenon of the silt treated by XG is more obvious than silt when the water content is 2%, 4%, and 8% because the pores of the silt treated by XG are supported by XG, which expands after absorbing moisture. Therefore, the water content of stress softening into stress hardening increased from 8% to 16%. The results indicate that XG can improve the strength and stability of soil after improving the micropore structure of the soil.

Table 3. Strength properties of the XG-silt specimens under different conditions (m_{bp}/m_s).

w (%)	σ_v (kPa)	$m_{bp}/m_s = 0\%$			$m_{bp}/m_s = 2\%$			Increment of c	Increment of ϕ
		τ_f (kPa)	c (kPa)	ϕ (°)	τ_f (kPa)	c (kPa)	ϕ (°)		
2	50	434.4			1033			2.32	1.515
	100	478.5	378.15	46.55	1141	878.50	70.50		
	200	591			1450				
4	50	349			870.7			2.36	1.557
	100	456.6	325.45	43.57	1040	766.70	67.82		
	200	503.7			1248				
8	50	155.2			155.2			1.22	1.019
	100	240.8	147.3	31.05	256.9	165.20	31.65		
	200	256.6			278.5				
16	50	62.11			100.5			1.42	1.402
	100	97.45	48.09	21.91	123.6	68.15	30.71		
	200	125.5			188.3				
22	50	45.03			59.03			1.81	1.916
	100	57.2	38.58	9.19	70.94	69.63	17.61		
	200	70.1			93.42				

The mercury intrusion test results indicate that the pore size distribution of the silt specimen is bimodal. The dispersed pore distribution of the specimens results in an unstable structure. The silt specimen is easily disturbed by external loads; thus, the strength of the silt specimen is small. After adding XG, the silt pore size decreased, the pore size distribution changed into a unimodal pore size distribution, and the pore structure stability improved. The water retention capacity and shear strength of the silt, therefore, significantly increased. The SEM test results showed that the cohesion and internal friction angle of the silt specimens under different water content was significantly higher because XG blocks the pores of soil and produces a hydrogel that can bond silt particles together [39,55–57].

4. Conclusions

A series of microscopic tests, water retention tests, and shear tests were carried out to explore the effect and mechanism of the strength characteristics of silt treated with xanthan gum. The main conclusions are as follows.

The drying and wetting curves of the specimens all shifted to higher water retention capacity with increasing xanthan gum content, and the hysteretic circle area between the drying and wetting curves also gradually increased. Microscopic analysis showed that the pores of the specimens gradually filled with increasing xanthan gum content, and xanthan gum itself has strong water-retaining properties. The water retention capacity of the treated silt therefore increased.

The peak strength and residual strength of the specimens gradually increase with increasing vertical stress. The shear strength, cohesion, and internal friction angle of the pure and treated silt specimens significantly increased with decreasing water content. During the wetting process, the strength of the pure and treated silt specimens all significantly weakened with increasing water content, but the strength of the treated silt was notably higher than that without treatment. The microscopic analysis showed that xanthan gum fills the uneven pores in silt during the wetting process, which makes the pore distribution more uniform and the pore structure more stable. Xanthan gum forms hydrogel bonded with the silt particles, and the cementation between the soil particles was notable, thus significantly increasing the strength of the silt treated by xanthan gum.

As an eco-friendly and efficient material, xanthan gum can improve the strength and stability of silt after rainfall infiltration. Therefore, xanthan gum can be used to improve the engineering properties of soil during many projects, such as deep foundation treatment, slope treatment, highway subgrade treatment, etc. The shear strength prediction model based on experimental data needs to be further studied.

Author Contributions: Conceptualization, J.Z. (Junran Zhangand), Z.M. and T.J.; methodology, J.Z. (Junran Zhangand), Z.M. and J.Z. (Jindi Zhao); data curation, J.Z. (Junran Zhangand), J.Z. (Jindi Zhao), X.Z. and Z.M.; writing—original draft preparation, Z.M.; writing—review and editing, J.Z. and S.W.; visualization, Z.M.; supervision, J.Z. (Junran Zhangand); project administration, J.Z. (Junran Zhangand) and T.J.; funding acquisition, J.Z. (Junran Zhangand) and T.J. All authors have read and agreed to the published version of the manuscript.

Funding: This study is financially supported by the National Natural Science Foundation of China (Grant No. 41602295), the Foundation for University Key Teacher by the Ministry of Education of Henan Province (Grant No. 2020GGJS-094), the Key Scientific Research Projects of Colleges and Universities in Henan Province (Grant No. 21A410002), and the Doctoral Student Innovation Foundation of NCWU.

Conflicts of Interest: The authors declare no conflict of interest. The funders had no role in the design of the study; in the collection, analyses, or interpretation of data; in the writing of the manuscript, or in the decision to publish the results.

References

- Wang, Y.; Zhang, H.; Zhang, Z. Experimental Study on Mechanics and Water Stability of High Liquid Limit Soil Stabilized by Compound Stabilizer: A Sustainable Construction Perspective. *Sustainability* **2021**, *13*, 5681. [[CrossRef](#)]
- Kim, Y.; Worrell, E. CO₂ Emission Trends in the Cement Industry: An International Comparison. *Mitig. Adapt. Strat. Glob. Change* **2002**, *7*, 115–133. [[CrossRef](#)]
- Thangaraj, R.; Thenmozhi, R. Sustainable concrete using high volume fly ash from thermal power plants. *Ecol. Environ. Ment Conservat.* **2013**, *19*, 461–466.
- Alonso, S.; Palomo, A. Alkaline activation of metakaolin and calcium hydroxide mixtures: Influence of temperature, activator concentration and solids ratio. *Mater. Lett.* **2001**, *47*, 55–62. [[CrossRef](#)]
- Krivenko, P.V.; Kovalchuk, G.Y. Directed synthesis of alkaline aluminosilicate minerals in a geocement matrix. *J. Mater. Sci.* **2007**, *42*, 2944–2952. [[CrossRef](#)]
- Sofi, M.; van Deventer, J.S.J.; Mendis, P.A.; Lukey, G.C. Bond performance of reinforcing bars in inorganic polymer concrete (IPC). *J. Mater. Sci.* **2007**, *42*, 3107–3116. [[CrossRef](#)]
- Lee, S.; Chung, M.; Park, H.M.; Song, K.-I.; Chang, I. Xanthan Gum Biopolymer as Soil-Stabilization Binder for Road Construction Using Local Soil in Sri Lanka. *J. Mater. Civ. Eng.* **2019**, *31*, 06019012. [[CrossRef](#)]
- Chang, I.; Jeon, M.; Cho, G.-C. Application of Microbial Biopolymers as an Alternative Construction Binder for Earth Buildings in Underdeveloped Countries. *Int. J. Polym. Sci.* **2015**, *2015*, 326745. [[CrossRef](#)]
- Georgees, R.N.; Hassan, R.A.; Evans, R.P. A potential use of a hydrophilic polymeric material to enhance durability properties of pavement materials. *Constr. Build. Mater.* **2017**, *148*, 686–695. [[CrossRef](#)]
- Fatehi, H.; Abtahi, S.M.; Hashemolhosseini, H.; Hejazi, S.M. A novel study on using protein based biopolymers in soil strengthening. *Constr. Build. Mater.* **2018**, *167*, 813–821. [[CrossRef](#)]
- Liu, J.; Ali, A.; Su, J.; Wu, Z.; Zhang, R.; Xiong, R. Simultaneous removal of calcium, fluoride, nickel, and nitrate using microbial induced calcium precipitation in a biological immobilization reactor. *J. Hazard. Mater.* **2021**, *416*, 125776. [[CrossRef](#)] [[PubMed](#)]
- Hosseinpour, Z.; Najafpour-Darzi, G.; Latifi, N.; Morowvat, M.; Manahiloh, K.N. Synthesis of a biopolymer via a novel strain of *Pantoea* as a soil stabilizer. *Transp. Geotech.* **2020**, *26*, 100425. [[CrossRef](#)]
- Choi, S.-G.; Chang, I.; Lee, M.; Lee, J.-H.; Han, J.-T.; Kwon, T.-H. Review on geotechnical engineering properties of sands treated by microbially induced calcium carbonate precipitation (MICP) and biopolymers. *Constr. Build. Mater.* **2020**, *246*, 118415. [[CrossRef](#)]
- Bai, B.; Nie, Q.; Zhang, Y.; Wang, X.; Hu, W. Cotransport of heavy metals and SiO₂ particles at different temperatures by seepage. *J. Hydrol.* **2021**, *597*, 125771. [[CrossRef](#)]
- Van de Velde, K.; Kiekens, P. Biopolymers: Overview of several properties and consequences on their applications. *Polym. Test.* **2002**, *21*, 433–442. [[CrossRef](#)]
- Lora, J.H.; Glasser, W.G. Recent Industrial Applications of Lignin: A Sustainable Alternative to Nonrenewable Materials. *J. Polym. Environ.* **2002**, *10*, 39–48. [[CrossRef](#)]

17. Ortsi, W.J.; Roa-Espinosa, A.; Sojka, R.E.; Glenn, G.M.; Imams, S.H.; Erlacher, K.; Pedersen, J.S. Use of Synthetic Polymers and Biopolymers for Soil Stabilization in Agricultural, Construction, and Military Applications. *J. Mater. Civ. Eng.* **2007**, *19*, 58–66. [[CrossRef](#)]
18. Chang, I.; Prasadhi, A.K.; Im, J.; Cho, G.-C. Soil strengthening using thermo-gelation biopolymers. *Constr. Build. Mater.* **2015**, *77*, 430–438. [[CrossRef](#)]
19. Chang, I.; Prasadhi, A.K.; Im, J.; Shin, H.-D.; Cho, G.-C. Soil treatment using microbial biopolymers for anti-desertification purposes. *Geoderma* **2015**, 253–254, 39–47. [[CrossRef](#)]
20. Im, J.; Tran, A.T.; Chang, I.; Cho, G.-C. Dynamic properties of gel-type biopolymer-treated sands evaluated by Resonant Column (RC) Tests. *Géoméch. Eng.* **2017**, *12*, 815–830. [[CrossRef](#)]
21. Ayeldeen, M.; Negm, A.; El-Sawwaf, M.; Kitazume, M. Enhancing mechanical behaviors of collapsible soil using two biopolymers. *J. Rock Mech. Geotech. Eng.* **2017**, *9*, 329–339. [[CrossRef](#)]
22. Dehghan, H.; Tabarsa, A.; Latifi, N.; Bagheri, Y. Use of xanthan and guar gums in soil strengthening. *Clean Technol. Environ. Policy* **2019**, *21*, 155–165. [[CrossRef](#)]
23. Ghasemzadeh, H.; Modiri, F. Application of novel Persian gum hydrocolloid in soil stabilization. *Carbohydr. Polym.* **2020**, *246*, 116639. [[CrossRef](#)] [[PubMed](#)]
24. Chang, I.; Lee, M.; Tran, A.T.P.; Lee, S.; Kwon, Y.-M.; Im, J.; Cho, G.-C. Review on biopolymer-based soil treatment (BPST) technology in geotechnical engineering practices. *Transp. Geotech.* **2020**, *24*, 100385. [[CrossRef](#)]
25. Wallingford, L.; Labuza, T.P. Evaluation of the Water Binding Properties of Food Hydrocolloids by Physical/Chemical Methods and in a Low Fat Meat Emulsion. *J. Food Sci.* **1983**, *48*, 1–5. [[CrossRef](#)]
26. Sánchez, V.; Bartholomai, G.; Pilosof, A. Rheological properties of food gums as related to their water binding capacity and to soy protein interaction. *LWT Food Sci. Technol.* **1995**, *28*, 380–385. [[CrossRef](#)]
27. Khachatoorian, R.; Petrisor, I.G.; Kwan, C.-C.; Yen, T.F. Biopolymer plugging effect: Laboratory-pressurized pumping flow studies. *J. Pet. Sci. Eng.* **2003**, *38*, 13–21. [[CrossRef](#)]
28. Zhou, C.; So, P.; Chen, X. A water retention model considering biopolymer-soil interactions. *J. Hydrol.* **2020**, *586*, 124874. [[CrossRef](#)]
29. Bouazza, A.; Gates, W.; Ranjith, P. Hydraulic conductivity of biopolymer-treated silty sand. *Geotechnique* **2009**, *59*, 71–72. [[CrossRef](#)]
30. Rosenzweig, R.; Shavit, U.; Furman, A. Water Retention Curves of Biofilm-Affected Soils using Xanthan as an Analogue. *Soil Sci. Soc. Am. J.* **2012**, *76*, 61–69. [[CrossRef](#)]
31. Qureshi, M.U.; Chang, I.; Al-Sadarani, K. Strength and durability characteristics of biopolymer-treated desert sand. *Géoméch. Eng.* **2017**, *12*, 785–801. [[CrossRef](#)]
32. Cabalar, A.F.; Awraheem, M.H.; Khalaf, M.M. Geotechnical Properties of a Low-Plasticity Clay with Biopolymer. *J. Mater. Civ. Eng.* **2018**, *30*, 04018170. [[CrossRef](#)]
33. Chang, I.; Im, J.; Prasadhi, A.K.; Cho, G.-C. Effects of Xanthan gum biopolymer on soil strengthening. *Constr. Build. Mater.* **2015**, *74*, 65–72. [[CrossRef](#)]
34. Latifi, N.; Horpibulsuk, S.; Meehan, C.L.; Majid, M.Z.A.; Tahir, M.M.; Mohamad, E.T. Improvement of Problematic Soils with Biopolymer—An Environmentally Friendly Soil Stabilizer. *J. Mater. Civ. Eng.* **2016**, *29*, 10. [[CrossRef](#)]
35. Soldo, A.; Miletić, M.; Auad, M.L. Biopolymers as a sustainable solution for the enhancement of soil mechanical properties. *Sci. Rep.* **2020**, *10*, 267. [[CrossRef](#)]
36. Soldo, A.; Miletić, M. Study on Shear Strength of Xanthan Gum-Amended Soil. *Sustainability* **2019**, *11*, 6142. [[CrossRef](#)]
37. Sujatha, E.R.; Atchaya, S.; Sivasaran, A.; Keerdthe, R.S. Enhancing the geotechnical properties of soil using xanthan gum—An eco-friendly alternative to traditional stabilizers. *Bull. Eng. Geol. Environ.* **2021**, *80*, 1157–1167. [[CrossRef](#)]
38. Chang, I.; Im, J.; Lee, S.-W.; Cho, G.-C. Strength durability of gellan gum biopolymer-treated Korean sand with cyclic wetting and drying. *Constr. Build. Mater.* **2017**, *143*, 210–221. [[CrossRef](#)]
39. Lee, S.; Chang, I.; Chung, M.-K.; Kim, Y.; Kee, J. Geotechnical shear behavior of Xanthan Gum biopolymer treated sand from direct shear testing. *Géoméch. Eng.* **2017**, *12*, 831–847. [[CrossRef](#)]
40. Zhu, Z.-D.; Liu, S.-Y.; Shao, G.-H.; Hao, J.-X. Research on silts and silts treated with stabilizers by triaxial shear tests. *Rock Soil Mech.* **2005**, *12*, 1967–1971. [[CrossRef](#)]
41. Zhang, J.-W.; Kang, F.-X.; Bian, H.-L.; Yu, H. Experiments on unconfined compressive strength of lignin modified silt in Yel-low river flood area under freezing-thawing cycles. *Rock Soil Mech.* **2020**, *S2*, 1–6. [[CrossRef](#)]
42. Ni, J.; Li, S.-S.; Ma, L.; Geng, X.-Y. Performance of soils enhanced with eco-friendly biopolymers in unconfined compression strength tests and fatigue loading tests. *Constr. Build. Mater.* **2020**, *263*, 120039. [[CrossRef](#)]
43. Latifi, N.; Rashid, A.S.A.; Siddiqua, S.; Majid, M.Z.A. Strength measurement and textural characteristics of tropical residual soil stabilised with liquid polymer. *Measurement* **2016**, *91*, 46–54. [[CrossRef](#)]
44. Chang, I.; Im, J.; Cho, G.-C. Introduction of Microbial Biopolymers in Soil Treatment for Future Environmentally-Friendly and Sustainable Geotechnical Engineering. *Sustainability* **2016**, *8*, 251. [[CrossRef](#)]
45. Kodikara, J.; Barbour, S.; Fredlund, D. Changes in clay structure and behaviour due to wetting and drying. In Proceedings of the 8th Australian-New Zealand Conference on Geomechanics, Hobart, TAS, Australia, 15–17 February 1999.

46. Lee, J.; Fratta, D.; Akin, I. Shear strength and stiffness behavior of fine-grained soils at different surface hydration conditions. *Can. Geotech. J.* **2021**, *99*, 1–12. [[CrossRef](#)]
47. Bai, B.; Wang, Y.; Rao, D.-Y.; Bai, F. The effective thermal conductivity of unsaturated porous media deduced by pore-scale SPH simulation. *Front. Earth Sci.* **2022**. [[CrossRef](#)]
48. Bai, B.; Xu, T.; Nie, Q.; Li, P. Temperature-driven migration of heavy metal Pb²⁺ along with moisture movement in unsaturated soils. *Int. J. Heat Mass Transf.* **2020**, *153*, 119573. [[CrossRef](#)]
49. Bai, B.; Zhou, R.; Cai, G.; Hu, W.; Yang, G. Coupled thermo-hydro-mechanical mechanism in view of the soil particle rearrangement of granular thermodynamics. *Comput. Geotech.* **2021**, *137*, 104272. [[CrossRef](#)]
50. Sun, D.A.; Zhang, J.R.; Lu, H.B. Soil-water characteristic curve of Nanyang expansive soil in full suction range. *Rock Soil Mech.* **2013**, *34*, 1839–1846. [[CrossRef](#)]
51. Narjary, B.; Aggarwal, P.; Singh, A.; Chakraborty, D.; Singh, R. Water availability in different soils in relation to hydrogel application. *Geoderma* **2012**, *187–188*, 94–101. [[CrossRef](#)]
52. Tran, T.P.A.; Chang, I.; Cho, G.-C. Soil water retention and vegetation survivability improvement using microbial biopolymers in drylands. *Geomech. Eng.* **2019**, *17*, 475–483. [[CrossRef](#)]
53. Wang, Y.-X.; Shao, S.-J.; Wang, Z.; Liu, A.-G. Experimental study on the unloading characteristics of coarse aggregate under true triaxial shear loading. *J. Rock Mech. Eng.* **2020**, *39*, 1503–1512. [[CrossRef](#)]
54. Bai, B.; Yang, G.-C.; Li, T.; Yang, G.-S. A thermodynamic constitutive model with temperature effect based on particle rearrangement for geomaterials. *Mech. Mater.* **2019**, *139*, 103180. [[CrossRef](#)]
55. Chang, I.; Cho, G.-C. Shear strength behavior and parameters of microbial gellan gum-treated soils: From sand to clay. *Acta Geotech.* **2019**, *14*, 361–375. [[CrossRef](#)]
56. Chen, C.; Wu, L.; Perdjon, M.; Huang, X.; Peng, Y. The drying effect on xanthan gum biopolymer treated sandy soil shear strength. *Constr. Build. Mater.* **2019**, *197*, 271–279. [[CrossRef](#)]
57. Chang, I.; Kwon, Y.-M.; Im, J.; Cho, G.-C. Soil consistency and interparticle characteristics of xanthan gum biopolymer-containing soils with pore-fluid variation. *Can. Geotech. J.* **2018**, *56*, 1206–1213. [[CrossRef](#)]

Article

Long-Term Performance of the Water Infiltration and Stability of Fill Side Slope against Wetting in Expressways

Yuedong Wu, Xiangyu Zhou and Jian Liu *

Key Laboratory of Ministry of Education for Geomechanics and Embankment Engineering, Hohai University, Nanjing 210098, China; hhuwyd@163.com (Y.W.); zxy1152021469@hhu.edu.cn (X.Z.)

* Correspondence: 20170053@hhu.edu.cn; Tel.: +86-1836-296-0323

Abstract: Different settlements and instabilities of unsaturated subgrade subjected to wetting have been paid increasing attention in the southeast coastal areas of China. However, the treatments are costly when they are used in engineering. In addition, the long-term performances of the treatments are unclear. Based on seepage theory for unsaturated soils, a novel subgrade using a capillary barrier was proposed in this study to reduce the different settlements and stabilities. Compared with previous studies, a capillary barrier was merely applied in the landfill. The long-term performance and feasibility of a capillary barrier applied in a tilted subgrade slope is worthy of study, particularly in humid climates. Using Geo-Studio, the feasibility was verified by comparing a conventional subgrade with a subgrade using a capillary barrier in southeast coastal areas in terms of pore-water pressure, water content, settlement, and the safety factor. The numerical results showed that the subgrade using a capillary barrier could provide significant improvements in the performance of reducing the impact of pore-water pressure distribution it suffered from, so as to lead to smaller different settlements. The vertical settlement of the pavement using a capillary barrier over a 1 year period was 1 cm. Compared with a conventional subgrade, the settlement fell by 94%, and the safety factor increased by 15% for the subgrade using the capillary barrier.

Keywords: unsaturated subgrade; capillary barrier; distress control of wetting

Citation: Wu, Y.; Zhou, X.; Liu, J. Long-Term Performance of the Water Infiltration and Stability of Fill Side Slope against Wetting in Expressways. *Appl. Sci.* **2022**, *12*, 5809. <https://doi.org/10.3390/app12125809>

Academic Editor: Bing Bai

Received: 2 April 2022

Accepted: 4 June 2022

Published: 7 June 2022

Publisher's Note: MDPI stays neutral with regard to jurisdictional claims in published maps and institutional affiliations.



Copyright: © 2022 by the authors. Licensee MDPI, Basel, Switzerland. This article is an open access article distributed under the terms and conditions of the Creative Commons Attribution (CC BY) license (<https://creativecommons.org/licenses/by/4.0/>).

1. Introduction

With the development of social economy and the requirements of modern transportation, expressways have become a focus during city construction [1]. Different from buildings, strict requirements are considered for the foundation of expressways such as the evaluation index of the expressway (i.e., fast, security, economy, and comfort). However, many problems still exist after an expressway's construction. Firstly, the safety of the expressway is affected directly by the instability of the subgrade. Secondly, if different settlement occurs on the expressway pavement, the driving speed is reduced. Moreover, the impact force caused by slowing down the driving speed is further exacerbated by the extent of the unevenness of the expressway pavement. Therefore, a vicious circle is formed, which further affects driving safety and causes huge economic losses [2]. These problems have seriously affected the use of expressways, especially in areas in southeast coastal provinces where the economy is developing rapidly. They are located in the region of a continental monsoon climate zone with relatively high rainfall in China. Therefore, in these areas, the subgrades have been greatly affected after completion by atmospheric conditions that include rainfall and evaporation. The instability and different settlement become more prominent under the influence of wet conditions [3].

For expressways, the foundation soil is located above the groundwater table isoline and is in an unsaturated state. In the unsaturated subgrade, the volumetric moisture content increases with rainfall. Therefore, the strength of the foundation soil is minimized, and it leads to instability and different settlement of the subgrade. In order to prevent

instability and reduce different settlements after completion, a long–short pile composite foundation [4,5] is adopted. This enables piles of different lengths and stiffnesses to carry more loads with a decrease in the proportion of the load on the soil in the subgrade. Moreover, it makes up for the decrease in the soil strength caused by wetting deformation. However, the pile foundation greatly increases the cost of an expressway’s construction, and the long-term performance of the pile is still unclear. The composite foundation using foamed cement banking (FCB) as a replacement is another effective treatment measure [6]. FCB is a light-weight material with low density, high strength, and low permeability. By minimizing its weight and permeability, the instability and settlement problems are effectively delayed due to the wetting deformation of the expressway pavement. However, FCB is still in the research stage. The influencing factors of its strength and permeability are still unclear. Wang [7] used a soil stabilizer to reinforce the silty clay for the subgrade. He studied the pavement’s performance with a mixture composed of the best proportion, which provided the basis and reference for similar engineering applications. Apart from using a soil stabilizer, Zhao [8] proposed that the recycled fine soil of construction waste with a diameter under 5 mm could be used in expressway subgrade. The soil was validated as a good subgrade material through basic experiments. However, the existing improvements were all treatment methods based on materials without considering the wetting distress on the long-term performance. The construction cost has increased because of these methods, and long-term performance under wetting and drying cycles is unclear. Hence, we propose effective measures to block the infiltrating rainwater in the subgrade through a capillary barrier.

A capillary barrier has been widely used in landfill cover systems, because of its advantages of long service life, ease of construction, and environment conservation [9,10]. It consists of fine layers over coarse layers, which are composed of different properties. Soil properties are very important in engineering. Different soil particles play an important role in the subgrade soil, which affect soil erodibility and the infiltration rate of water. Arunrat et al. [11] pointed out the variations in soil properties and explained how soil erodibility is affected. Wang et al. [12] showed that the different properties and the different poultry compost amendments to the soils resulted in distinct runoff, sediment yield, and soil erodibility values. With the different permeability coefficients of these two soil layers under unsaturated conditions, the fine-grained layer, used as a buffer, can store and transfer infiltrating water effectively [13]. Ross [14] and Stormont [15] derived the evaluation index of capillary barriers through the theory of the permeability coefficients of two soils. The evaluation index is the distance downslope, called the diversion length. It has been verified that a capillary barrier can effectively block the infiltrating rainwater within the diversion length [16,17]. Rahardjo [18] proposed that a capillary barrier could be used to protect the slope. The waterproof effect of a capillary barrier was verified through field tests and through the same way the application of a capillary barrier to the slope was studied and found to be feasible. Wu et al. [19] proposed that a capillary barrier could be applied as a cover barrier to protect the expressway subgrade from wetting distress. Previous studies focused on the effect and mechanism of a capillary barrier applied to landfills in dry climates. However, the performance of a capillary barrier in humid climates is still unclear. In other words, the performance of a capillary barrier applied to a slope shoulder is still unclear in humid climates in China’s southeast coastal areas. Meanwhile, the environment of expressways in the southeast coastal areas of China is generally humid compared with the relatively dry landfill cover system. Due to the presence of these peculiarities, it is necessary to verify the rationality of the application of the capillary barrier on the expressway.

This paper firstly explains the mechanism of moisture migration in the unsaturated subgrade and proposes effective measures to block the infiltrating rainwater in the subgrade through capillary barrier. Then, the anti-seepage effect of the capillary barrier is introduced. Comparing the numerical simulation results of the subgrade with or without a capillary barrier, the feasibility of applying a capillary barrier to the subgrade was verified. Finally,

the results were evaluated and focused on the role of the capillary barrier in the anti-seepage performance by simulating their changes in moisture content, pore-water pressure, settlement, and safety factor of the subgrade under rainfall conditions in the southeast areas of China.

2. Reinforcement Mechanism of Subgrades with a Capillary Barrier

In the southeast coastal areas of China, the groundwater table is generally below the original ground, and the subgrade is generally in an unsaturated state. Therefore, the soil strength is directly influenced by the distribution of matric suction in the subgrade soil. The matric suction is a manifestation of the energy produced by the water in the soil due to the capillary effect. Numerically, it is equal to the pore-air pressure minus the pore-water pressure ($u_a - u_w$). Based on the M-C model, Fredlund and Rahardjo [20] proposed a formula for the shear strength of unsaturated soil:

$$\tau_u = c' + (\sigma - u_a) \tan(\phi') + (u_a - u_w) \tan(\phi^b) \tag{1}$$

where τ_u is the shear strength of unsaturated soil; c' is effective cohesion; u_a is the pore air pressure; u_w is the pore-water pressure; ϕ' is the effective internal friction angle; ϕ^b is the shear strength increase rate with the change in matric suction. Figure 1 shows the traditional subgrade structure. After the expressway is completed, the pavement is an asphalt layer with good waterproofness. However, the fill slope is generally exposed in the atmosphere. When it rains, moisture flows into the subgrade from the slope shoulder. Because the subgrade is under unsaturated conditions, the soil suction in the subgrade is large, and the suction at the shoulder slope is small. Moisture gradually inflows into the subgrade soil along the suction gradient line. It is worth noting that the almost horizontal water flow is unsaturated flow. Therefore, the moisture content of the subgrade soil continues to increase, and the suction continues to decrease. According to formula (1), it can be seen that the reduction in shear strength is directly influenced by the reduction in suction, which may lead to the shear deformation and instability of the subgrade. Figure 2a shows the soil water characteristic curve of the subgrade soil. The water-entry value was approximately 6 kPa and the air-entry value was approximately 28 kPa. The difference between the water-entry value and the air-entry value of the subgrade soil was approximately 22 kPa. However, the standard design value of the vehicle load on the expressway was only 10.5 kPa [21]. Therefore, the strength change caused by the wetting subgrade should not be ignored.

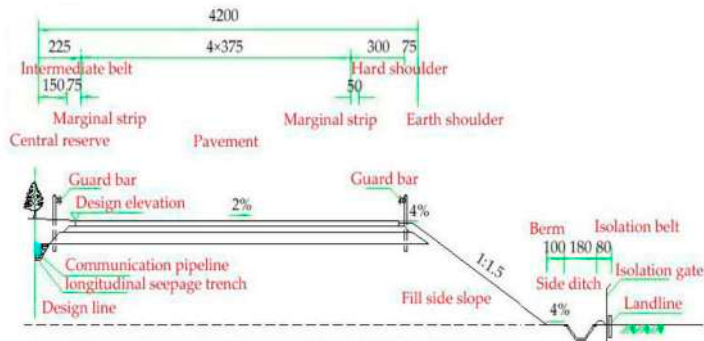
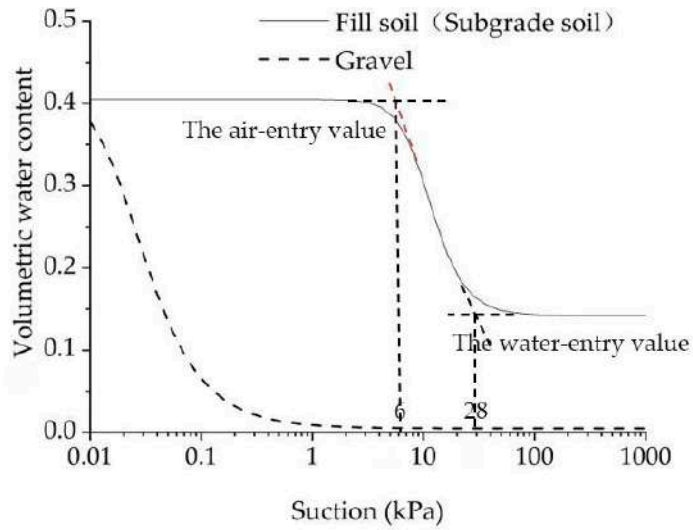
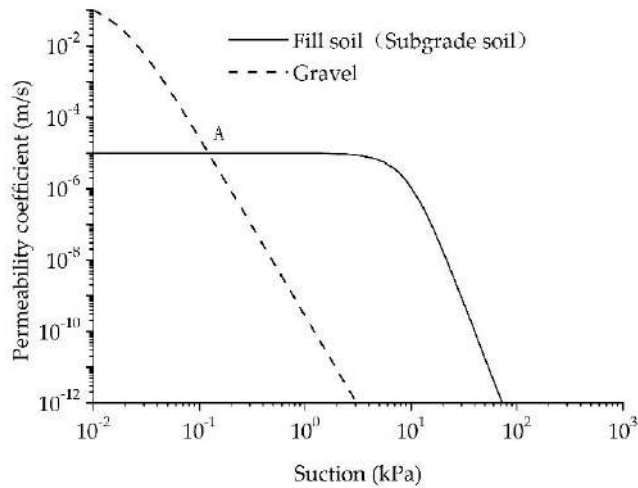


Figure 1. Schematic diagram of a standard subgrade (unit: mm).



(a)



(b)

Figure 2. (a) Soil water characteristic curves and (b) permeability function of soils used in the subgrade.

In order to avoid the decrease in soil strength due to the presence of rainfall, this paper proposes to add a capillary barrier on the fill slope to protect the subgrade. The fine-grained soil in the capillary barrier was filled with the soil near the expressway. Gravel or sand was used as the coarse-grained soil. The fill slope soil from the surface to bottom was the fill near the expressway, gravel, and subgrade soil. Figure 2 shows the soil water characteristic curves and permeability coefficient curves of the two soils. The unsaturated permeability coefficients were estimated using the Mualem model [22].

$$k = k_s S_e^{0.5} \left(\int_0^{S_e} \frac{dS_e}{\psi} / \int_0^1 \frac{dS_e}{\psi} \right)^2 \tag{2}$$

where k_s is equal to the saturated permeability coefficient; S_e is equal to the effective saturation; ψ is equal to the soil suction. The slope in the soil water characteristic curve of the coarse-grained soil was steeper because of its large pores. Thereby, its water-holding capacity was worse, and the permeability coefficient curve was also steeper. The volumetric water content and permeability coefficient have a nonlinear distribution under different suction ranges. The suction where the permeability coefficients of two soils are equal is the critical failure suction, as shown in Figure 2b, which is the suction at point A.

With the water content continuously increasing when it rains, soil suction decreases. Rainwater enters the capillary barrier along the slope shoulder and inflows into the fill due to the fact of gravity. When soil suction is higher than the critical failure suction, the permeability coefficient of the fill is higher than that of the gravel. At this time, water accumulates only at the interface between the gravel and the fill. It does not breakthrough into the gravel layer. Because the capillary barrier is tilted, the moisture accumulated at the interface is drained laterally along the interface. When soil suction is less than the critical failure suction, the capillary barrier fails. At the interface, the diversion length is the distance from the point where the suction is equivalent to the critical failure suction to the surface of slope. It was evidently shown that the capillary barrier is effective within the diversion length. Walter [23], Tami [24], and Aubertin [25] pointed out that the diversion length of the capillary barrier was influenced by the slope angle, thickness of the fine-grained soil, the properties of the fine-grained and coarse-grained soils, layer thickness, rainfall condition, etc. They all focused on the landfill cover system. Compared with the landfill, the slope length of the subgrade is relatively shorter, and the blocking effect of rainwater is better.

3. Calculation Model of the Subgrade with a Capillary Barrier

It is difficult to study wetting deformation using an analytical solution. For one thing, the soil water characteristic curve and the permeability coefficient equation of soils are both nonlinear. For another, the strength constitutive relationships of soils are complicated. To quantitatively analyze the deformation and stability of the subgrade protected by a capillary barrier during the rainfall, Geo-Studio 2018 R2 software (version 9.1.1.16749) was used to carry out a numerical simulation study in this paper. Geo-Studio is an overall analysis tool for a set of geological structure model software. The test sections in this paper included SLOPE/W (slope stability analysis module), SEEP/W (groundwater seepage analysis module), and SIGMA/W (rock and soil stress and deformation analysis module).

3.1. Mesh and Model

Figure 3 shows the model of the subgrade with a capillary barrier. The figure on the horizontal axis means the distance from the road's central line. The figure on the vertical axis means the height of the pavement to the bedrock. A subgrade section was selected in Guangzhou. The height of the foundation was 20 m. The height of the subgrade was 6 m. The slope of the shoulder was 1:1.5. Due to the symmetry of the subgrade, the simulation only took half of the subgrade for the research. This paper studied two subgrade models: (1) a conventional subgrade; (2) a subgrade using a capillary barrier. The conventional subgrade was composed of a single soil layer, while the subgrade protected by a capillary barrier added a capillary barrier on the slope shoulder. The subgrade soil was used as fill with a thickness of 0.3 m. The thickness of the gravel was 0.2 m.

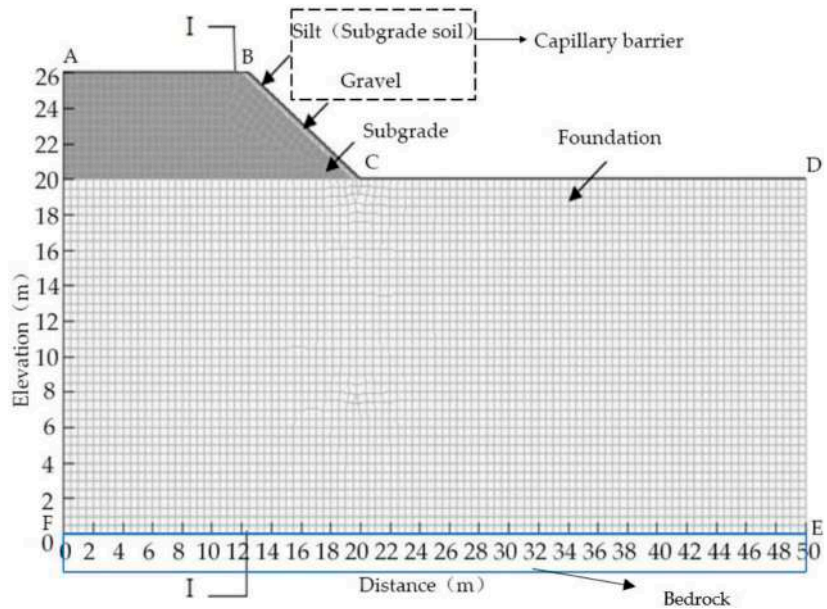


Figure 3. Mesh of the subgrade with a capillary barrier (unit: m).

3.2. Material Properties

The physical properties of soils for the subgrade with a capillary barrier are shown in Tables 1 and 2. Based on the data in Figure 4, the coefficient of uniformity of the gravel was 14 and that of the fill soil was 6.4. The coefficient of the curvature of the gravel was 2.8 and that of the fill soil was 1.2. According to the Standard for Classification of Engineering Soils [26], the fill soil was classified as the silty clay of well gradation, and the gravel was well graded. The soil involved in this paper included foundation soil, subgrade soil, and gravel. In view of the similar moisture migration properties of the foundation and the subgrade, the identical hydraulic characteristic parameters were used for the subgrade and the foundation to facilitate the study. In the numerical simulation, the soil water characteristic curve of the subgrade soil was based on the test data from Jun Luo [3]. The soil water characteristic curve of the gravel was based on the test data used by Morris et al. [27]. The saturated permeability coefficient of the soil was measured by the constant head method. However, the unsaturated permeability coefficient equation was predicted on the basis of the soil water characteristics using the van Genuchten functions as shown in Figure 2. The ideal elastoplastic M-C model was adopted as the mechanical model for the deformation, and the strength parameters of the foundation soil and subgrade soil were determined by consolidated drained triaxial tests. The results of the triaxial shear test are shown in Table 1. The gravel was only 0.2 m thick due to the fact of its small thickness. In order to ensure the calculations were convenient, the strength characteristics were set to elastic materials and the data, listed in Table 1, were selected based on the elastic modulus test by Yuedong Wu et al. [28].

Table 1. The physical properties of various soils for the subgrade with a capillary barrier.

Type of Soil Layer	Maximum Dry Density (g/cm ³)	Optimum Moisture Content (%)	Liquid Limit (%)	Plastic Limit (%)	Plasticity Index
Foundation	1.675	15.03	82	23	11
Subgrade	1.675	15.03	82	23	11
Gravel	2.168				

Table 2. Strength properties of the various soils for the subgrade with a capillary barrier.

Type of Soil Layer	Bulk Density (kN/m ³)	Elastic Modulus (MPa)	Poisson's Ratio	c' (kPa)	φ' (°)	φ ^b (°)
Foundation	18.3	20	0.35	1	23	11
Subgrade	18.3	20	0.35	5	26	13
Gravel	18.3	40	0.35	-	-	-

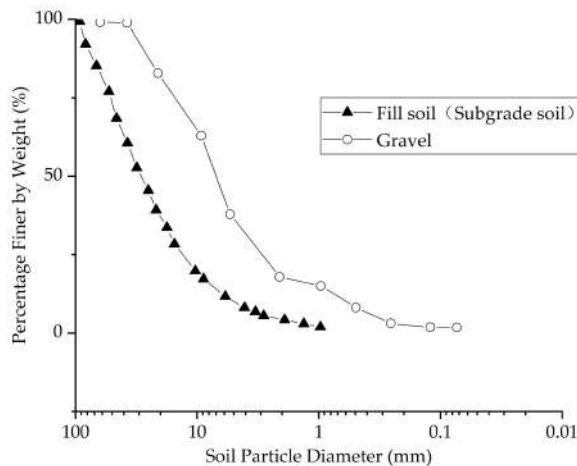


Figure 4. Grain size distribution of the soils.

3.3. Simulation Steps and Boundary Conditions

In order to simulate the impact of rainfall on the expressway, it was necessary to eliminate other factors that cause settlement. This paper simulated the following four steps.

The first step was to perform an analysis on the stress and deformation (SIGMA/W) of the subgrade. The design load on the pavement (AB) was set to complete the load and geo-stress balance. According to the expressway design code, the standard design load of the pavement was 10.5 kPa. The left and right boundaries (i.e., AF and DE) were set to the displacement boundary condition, restraining in the horizontal direction. The bottom boundary (EF) was set to the displacement boundary conditions, restraining in the horizontal and vertical directions.

The second step was to conduct a water seepage analysis (SEEP/W) on the subgrade and design the flow boundary conditions on the shoulder slope (BC) and the ground (CD). The annual precipitation in Guangdong, eastern Guangxi, Fujian, Jiangxi, and most of Zhejiang along the southeast coast of China is 1500–2000 mm. The middle and lower reaches of the Yangtze River are 1000–1600 mm. The Huaihe River, Qinling Mountains, and the Liaodong Peninsula have an annual precipitation of 800–1000 mm. Moreover, the

seasonal distribution is uneven, with summer accounting for approximately 50% of the annual rainfall. Particularly, in this study, we focused on the long-term performance of the subgrade. The subgrade soil can store water. Unsaturated drainage still occurs from the topsoil when it does not rain. Therefore, the most extreme rainfall intensity was selected, which was 1000 mm in the summer and the rainfall on the rainfall surface was set to 1.27×10^{-7} m/s. In order to fully study the law of subgrade infiltration, the duration was chosen as 365 days, which considered the humid climate in the eastern coastal area. Due to the large stiffness and small deformation, we assumed that the impermeable bedrock was the bottom of the groundwater. Considering the surface runoff, the set flow boundary was a flow boundary condition that allowed for correction. The bottom boundary condition (EF) was the pressure head boundary condition. Assuming that the initial water level was 3 m below the ground, the pressure head of EF was set to 17 m.

The third step was to perform stress and deformation analysis (SIGMA/W) on the subgrade at the corresponding time. Using the stress conditions in step 1 and the pore-water pressure results at different moments in step 2 as suction conditions, the deformation response in the wetting conditions was calculated. The boundary conditions were the same as in Step 1 and Step 2. The results obtained were calculated with the load and geo-stress balance as the starting point.

In the fourth step, the slope stability analysis (SLOPE/W) of the subgrade was performed. The initial stress condition was the result of step 3. The initial pore-water pressure distribution condition was the result of step 2. The boundary conditions were the same as in step 1.

4. Numerical Simulation Results

4.1. The Law of Moisture Migration in the Subgrade

When the conventional subgrade was subjected to rainfall, the rainwater flowed from the slope shoulder of the expressway to the inside of the subgrade soil, as shown in Figure 5a. This led to a decrease in the pore-water pressure of the soil near the shoulder. But far away from the expressway shoulder, the distribution of the pore-water pressure was almost unaffected. This was mainly due to the effect of gravity, which limits the scope of moisture migration. The influence range of the rainfall in the conventional subgrade was approximately 3 m.

Compared with the conventional subgrade, the subgrade using a capillary barrier was far less affected by rain. In the subgrade with a capillary barrier, water was mainly diverted laterally from the fine-grained soil of the capillary barrier. The distribution of the pore-water pressure in the subgrade and the foundation was almost horizontal, but the flow was concentrated at the bottom of the expressway's slope shoulder. In order to more effectively minimize the impact of rainfall on the pore-water pressure in the foundation, it is recommended that a drainage ditch connecting the fine-grained soil layer be constructed at the base of the slope during the site's construction to facilitate drainage.

It is worth noting that the impermeability of the pavement is very important for the subgrade using a capillary barrier. If there are many cracks in the expressway pavement, rainwater will infiltrate into the subgrade along the cracks, which will lead to a decrease in the pore-water pressure of the subgrade. Under this condition, the suction in the subgrade soil is first reduced to a critical failure suction, and the capillary barrier loses its blocking effect.

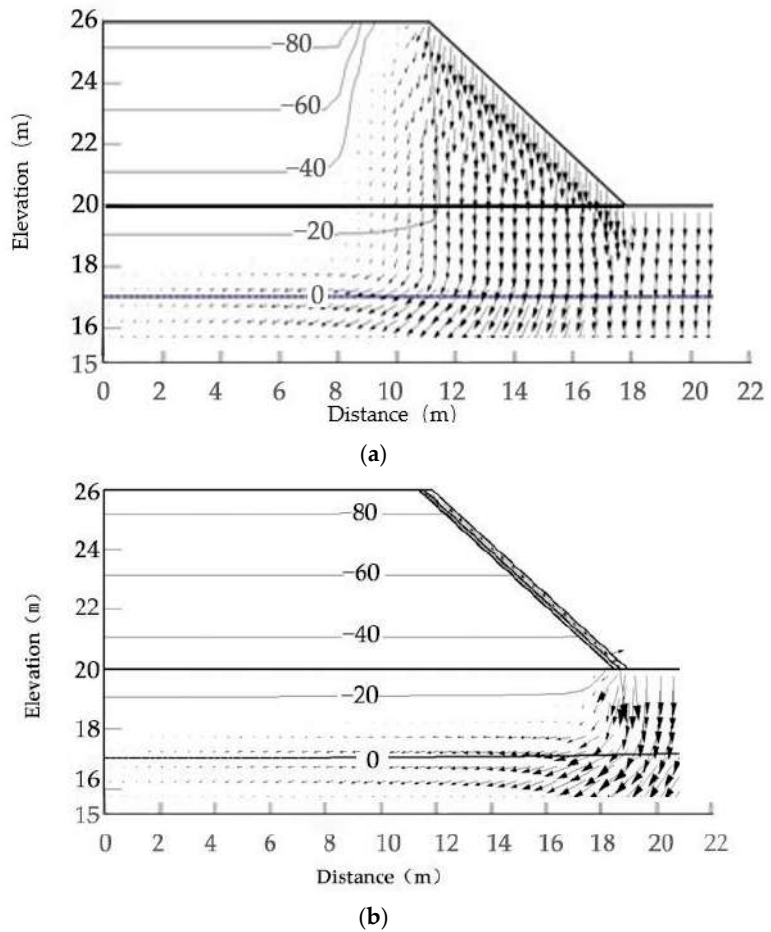


Figure 5. Pore-water pressure distribution in (a) traditional subgrade; (b) the subgrade with a capillary barrier at the end of the year.

Due to a deeper-seated slide, which often happens on the top of the slope, the pore-water pressure at the interface I-I was taken as the abscissa, and the elevation was taken as the ordinate (the elevation of CD was 0) to quantitatively study the impact of rainwater on the pore-water pressure, which is plotted as Figure 6. Under the action of rainwater, the soil in the middle and upper layers of the conventional subgrade was greatly affected. In the upper soil, the largest pore-water pressure was -31 kPa; in the middle soil, the pore-water pressure was maintained at approximately -25 kPa; the bottom soil was almost unaffected by rain and almost coincided with the hydrostatic pressure distribution. This distribution curve was not the same as the wetting law of a single-layer of soil [29], which is mainly due to the different intrusion surfaces of rainwater. The lateral slope in the subgrade was the rainwater immersion surface.

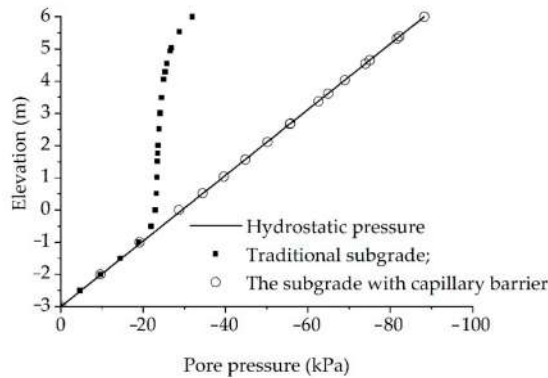


Figure 6. Pore-water pressure profiles at section I-I.

The subgrade using a capillary barrier was less affected by rain, and its pore-water pressure distribution almost coincided with the hydrostatic pressure distribution line. It can be seen that the blocking effect of the capillary barrier on the subgrade was more obvious. The capillary barrier used as a landfill cover system has been proven to be unsuitable for humid climates [16,17], but as a subgrade protection layer, the capillary barrier is suitable for humid climates. This is mainly due to the short length of the tilted slope in the subgrade, which is completely within the diversion length. In the middle and upper soils, the pore-water pressure in the subgrade protected by a capillary barrier is lower than that of the conventional subgrade. The difference between the two subgrades shows a nonlinear distribution, and the maximum was 57 kPa. Compared with the traditional capillary barrier, the pore-water pressure was reduced by 180%. It can be seen that the impact of the rainfall on the strength of subgrade cannot be ignored. It is worth noting that the value of ϕ^b in Formula (1) was generally different from that of ϕ . Therefore, the contribution of the pore-water pressure to the shear strength was also different from that of the additional stress (σ).

Figure 7 shows the change trend in the volumetric moisture content with elevation. The volumetric moisture content in the subgrade (elevation 0–6 m) was basically constant, which was mainly because the pore-water pressure in the subgrade was basically greater than the inflow value of the fill. In this case, a very small change in the water content caused a huge change in the pore-water pressure. The water-holding capacity of conventional subgrade was basically maintained at 0.17, while the water content of the subgrade with capillary barrier was at 0.14. Compared with the conventional subgrade, the moisture content of the subgrade protected by the capillary barrier was reduced by 18%.

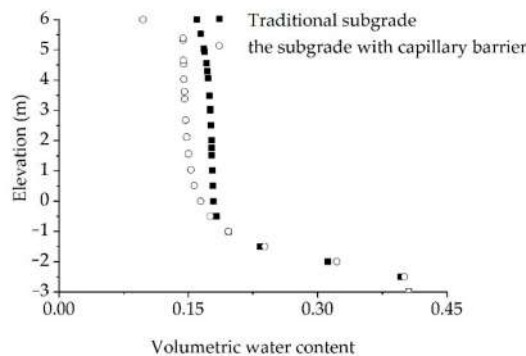


Figure 7. Volumetric water content profiles at section I-I.

4.2. Settlement and Deformation Law

Changes in the pore-water pressure caused changes in the shear strength. Figure 8 shows the deformation vector arrows of the subgrade protected by a capillary barrier. The subgrade with a capillary barrier was basically not affected by rainfall, while settlement still occurred. This was mainly because the slight change in the pore-water pressure at the bottom of the expressway shoulder slope caused the strength in the uplift area of the slip surface to decrease, which led to the shear deformation of the subgrade.

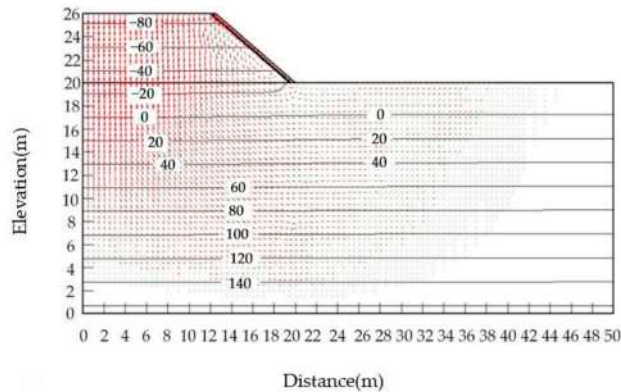


Figure 8. Deformation vector arrows of the subgrade with a capillary barrier.

Figure 9 shows the change trend in the expressway’s pavement AB settlement with horizontal displacement. In the nonaffected area, the settlement of the conventional subgrade was relatively small, which was only 1 cm. While in the affected area, the settlement was large, which was up to 16 cm. Large different settlements occurred at the shoulder and in the subgrade. The different settlement was up to 15 cm. However, the subgrade using a capillary barrier had a ground settlement of approximately 1 cm in the affected zone and the noninfluenced zone. The different settlement was also relatively small. Surprisingly, even if the pore-water pressure in the subgrade did not change, the subgrade still had a certain amount of settlement. This was mainly caused by the shear deformation of the foundation.

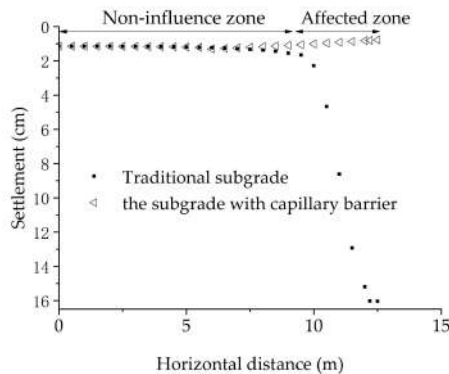


Figure 9. Comparison of the settlement in the different subgrades.

4.3. Variation Law of Safety Factor

The safety factor can be used to reflect the possibility of slope instability to a certain extent. As the subgrade and foundation are influenced by rainfall, the pore-water pressure in the traditional subgrade decreased, which reduced the overall safety factor of the subgrade.

The safety factor was reduced from 1.35 to 1.15 in one year as shown in Figure 10, and the decrease in the safety factor with time was nonlinear. The safety factor of the subgrade protected by the capillary barrier was almost unchanged. This was mainly due to the better blocking effect of the capillary barrier. In one year, the safety factor of the subgrade using a capillary barrier increased by 15% compared to the traditional subgrade.

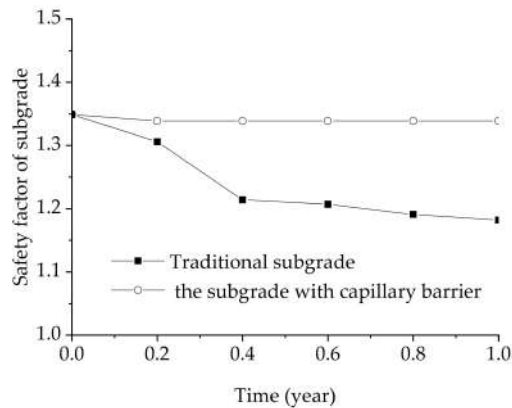


Figure 10. Comparison of the safety factor in the different subgrades.

5. Conclusions

In this study, we first proposed effective measures to block the infiltrating rainwater in the subgrade through a capillary barrier. Secondly, using the numerical simulation method, we conducted studies on the mechanism and stability of the capillary barrier used in the subgrade to control distress against wetting. The subgrade with a capillary barrier could effectively use the different permeability coefficients of the different types of soil to achieve an anti-seepage effect, which minimized the deformation of the subgrade and increased stability. Using the numerical simulation method, this paper analyzed the pore-water pressure distribution, settlement, and safety factor of the conventional subgrade and the subgrade protected by the capillary barrier. Through a comparison of the numerical results of the two subgrades, the following conclusions were drawn:

- (1) The pore-water pressure of the subgrade protected by the capillary barrier was hardly affected by rainfall. Compared with the conventional subgrade, the pore-water pressure was reduced by 180%, and the pore-water pressure distribution was close to the hydrostatic pressure distribution. The moisture content of the conventional subgrade was effectively reduced by approximately 18% by using a capillary barrier;
- (2) The settlement of the subgrade using a capillary barrier was uniform and small, and is only 1 cm. Compared with the conventional subgrade, the settlement was reduced by 94%. The safety factor of the subgrade using a capillary barrier was almost unchanged. Compared with the conventional subgrade, the safety factor increased by 15%;
- (3) In humid climates, it is feasible to use subgrades with a capillary barrier to reduce the deformation and stability problems caused by humidification.

6. Recommendations for Future Study

This was a preliminary study that merely focused on the feasibility of a capillary barrier for the subgrade. The parameters of soil were selected from the literature to study the feasibility. In the future, specific subgrade soils will be used to conduct experiments for more in-depth research. Furthermore, the capillary barrier was used as the cover layer for natural materials without manual treatments, which can effectively block the infiltrating rainwater. It can be applied in many areas including slope stability. It can prevent rainwater infiltration so as to improve the slope's stability. However, it cannot be applied in humid

climates due to the fact of its poor water storage capacity. In the future, more studies should be carried out on improving its water storage capacity by using new materials with high water storage capacity and methods so as to be applies more in engineering.

Author Contributions: The formal analysis, formula reasoning, and the performance of the experiment, as well as the original draft preparation were completed by X.Z.; Review and editing were completed by Y.W. and J.L. All authors have read and agreed to the published version of the manuscript.

Funding: This research was funded by the Fundamental Research Funds for the Central Universities (grant numbers: B210202034, B200204036, and B200204032).

Institutional Review Board Statement: Not applicable.

Informed Consent Statement: Not applicable.

Data Availability Statement: Data sharing not applicable. No new data were created or analyzed in this study.

Conflicts of Interest: The authors declare no conflict of interest.

References

- Ni, X.; Ma, Y.; Gao, B.; Xue, S.; Bai, P.; Huo, X.; Bian, X. *2013–2017 China Highway Industry Investment Analysis and Prospect Forecast Report*; CIC: Beijing, China, 2012.
- Zheng, S. Study on the Settlement of Bridge Embankment Expressway Opened Traffic in Soft Subsoil. Master’s Thesis, Hohai University, Nanjing, China, 2010.
- Luo, J. The Research on Moisture Migration In Silt Embankment and Differential Settlement Formation Mechanism for Widened Road. Master’s Thesis, Changsha University of Science & Technology, Changsha, China, 2006.
- Gong, X. *Theory of Composite Foundations and Engineering Applications*; China Architecture and Building Press: Beijing, China, 2002; pp. 76–79.
- Liu, J. Application and Research of Long-Short-Pile Composite Foundation on Soft Foundation of Motorway. Master’s Thesis, Hohai University, Nanjing, China, 2010.
- Wu, Y.; Liu, J. Research on foamed cement banking for non-uniform differential settlement in used super highway. In *Architecture, Civil and Environmental Engineering*; ACEE 2011; Hohai University: Nanjing, China, 2011; Volume 6, pp. 5334–5337.
- Wang, D. Experimental Study on Pavement Performance of the Fine-Grained Soil Stabilized by Soil Stabilizer. Master’s Thesis, Zhengzhou University, Zhengzhou, China, 2010.
- Zhao, D. Research on properties of expressway subgrade using the recycled fine soil of construction waste. *World Build. Mater.* **2010**, *34*, 42–44.
- Hauser, V.L.; Weand, B.L.; Gill, M.D. *Alternative Landfill Covers*; Prepared for Air Force Center for Environmental Excellence, Technology Transfer Division; Brooks AFB: San Antonio, TX, USA, 2001.
- Benson, C.H.; Khire, M.V. *Earthen Covers for Semi-Arid and Arid Climates*; Geotechnical Special Publication: Reston, VA, USA, 1995.
- Arunrat, N.; Sreenonchai, S.; Kongsurakan, P.; Hatano, R. Assessing Soil Organic Carbon, Soil Nutrients and Soil Erodibility under Terraced Paddy Fields and Upland Rice in Northern Thailand. *Agronomy* **2022**, *12*, 537. [[CrossRef](#)]
- Wang, G.; Fang, Q.; Wu, B.; Yang, H.; Xu, Z. Relationship between soil erodibility and modeled infiltration rate in different soils. *J. Hydrol.* **2015**, *528*, 408–418. [[CrossRef](#)]
- Rahardjo, H.; Krisdani, H.; Leong, E. Application of unsaturated soil mechanics in capillary barrier system. In *Third Asian Conference on Unsaturated Soils*; Science Press: Alexandria, NSW, Australia, 2005; pp. 127–137.
- Benjamin, R. The diversion capacity of capillary barriers. *Water Resour. Res.* **1990**, *26*, 2652–2659.
- Stormont, J.C. The effect of constant anisotropy on capillary barrier performance. *Water Resour. Res.* **1995**, *31*, 783–785. [[CrossRef](#)]
- Stormont, J.C. The effectiveness of two capillary barriers on a 10% slope. *Geotech. Geol. Eng.* **1996**, *14*, 243–267. [[CrossRef](#)]
- Qian, X.; Koerner, R.M.; Gray, D.H. *Geotechnical Aspects of Landfill Design and Construction*; Prentice Hall: Hoboken, NJ, USA, 2002; pp. 562–567.
- Rahardjo, H.; Hua, C.J.; Leong, E.C.; Santoso, V.A. Performance of an instrumented slope under a capillary barrier system. In *Proceedings of the Fifth International Conference of Unsaturated Soils, Barcelona, Spain, 6–8 September 2010*; pp. 1279–1284.
- Wu, Y.; Diao, H.; Liu, J.; Chen, R.; Shi, X. A Embankment Construction and Method to Prevent Wetting Distress Control for Highway. China Patent 201310408929.3, 30 August 2016.
- Fredlund, D.G.; Rahardjo, H. *Soil Mechanics for Unsaturated Soils*; John Wiley & Sons: New York, NY, USA, 1993; pp. 267–269.
- JTG D60-2004*; General Code for Design of Highway Bridges and Culverts. China Communications Press: Beijing, China, 2004; pp. 53–55.
- Mualem, Y. A new model for predicting the hydraulic conductivity of unsaturated porous media. *Water Resour.* **1976**, *12*, 513–522. [[CrossRef](#)]

23. Walter, M.T.; Kim, J.S.; Steenhuis, T.S.; Parlange, J.Y.; Heilig, A.; Braddock, R.D.; Selker, J.S.; Boll, J. Funneled flow mechanisms in a sloping layered soil-Laboratory investigation. *Water Resour. Res.* **2000**, *36*, 841–849. [[CrossRef](#)]
24. Tami, D.; Rahardjo, H.; Leong, E.C.; Fredlund, D.G. Design and laboratory verification of a physical model of sloping capillary barrier. *Can. Geotech. J.* **2004**, *41*, 814–830. [[CrossRef](#)]
25. Aubertin, M.; Cifuentes, E.; Apithy, S.A.; Bussière, B.; Molson, J.; Chapuis, R.P. Analyses of water diversion along inclined covers with capillary barrier effects. *Can. Geotech. J.* **2009**, *46*, 1146–1164. [[CrossRef](#)]
26. GB/T 50145-2007; Standard for Classification of Engineering Soils. Ministry of Construction of the People’s Republic of China: Beijing, China, 2007.
27. Morris Carl, E.; Stormont John, C. Parametric study of unsaturated drainage layers in a capillary barrier. *J. Geotech. Geoenviron. Eng.* **1999**, *125*, 1057–1065. [[CrossRef](#)]
28. Wu, Y.; Wang, W.; Liu, J.; Ji, K. Test research on compaction effect of expressway embankment with sand-gravel-cobble mixture. *Rock Soil Mech.* **2012**, *33*, 211–216.
29. Zhan, L.T.; Ng, C.W. Analytical analysis of rainfall infiltration mechanism in unsaturated soils. *Int. J. Geomech.* **2004**, *4*, 273–284. [[CrossRef](#)]

Article

An Experimental Study on the Migration of Pb in the Groundwater Table Fluctuation Zone

Jihong Qu ^{1,2,*}, Tiangang Yan ^{1,2}, Yifeng Zhang ^{1,2}, Yuepeng Li ^{1,2}, Ran Tian ^{1,2}, Wei Guo ^{1,2} and Jueyan Jiang ^{1,2}

¹ College of Geosciences and Engineering, North China University of Water Resources and Electric Power, Zhengzhou 450046, China; ytg@stu.ncwu.edu.cn (T.Y.); yyds1231110@163.com (Y.Z.); liyuepeng@ncwu.edu.cn (Y.L.); tianran0227@163.com (R.T.); gwmengyeah@163.com (W.G.); jiangjueyan@stu.ncwu.edu.cn (J.J.)

² Collaborative Innovation Center for Efficient Utilization of Water Resources, Zhengzhou 450046, China

* Correspondence: qujihong@ncwu.edu.cn; Tel.: +86-133-9370-9096

Abstract: As a result of fluctuations in the shallow groundwater table, hydrodynamic conditions change alongside environmental conditions and hydrogeochemical processes to affect pollutant migration. The study aimed to investigate the migration, adsorption, and desorption characteristics of Pb on fine, medium, and coarse sand in the water table fluctuation zone by using several laboratory methods, including the kinetic aspects of Pb²⁺ adsorption/desorption and water table fluctuation experiments. The results showed that the adsorption and desorption curves fit the Elovich equation well at a correlation coefficient above 0.9. In the adsorption and desorption kinetic experiments for fine, medium, and coarse sand collected and from the floodplain, the maximum adsorption capacity of Pb²⁺ was 2367 mg·kg⁻¹, 1848 mg·kg⁻¹, and 1544 mg·kg⁻¹, respectively. The maximum desorption capacity of Pb²⁺ was 29.18 mg·kg⁻¹, 62.38 mg·kg⁻¹, and 81.60 mg·kg⁻¹, respectively. In environments with pH greater than 4, the adsorption capacity was proportional to the pH, but the desorption capacity decreased as the pH increased in water. As the water table varied, the lowest pH occurred in the polluted medium we set initially. When the distance between the pollutants and sample solution grew further, pH increased, and the Pb²⁺ concentration decreased in the sample solution. In the column experiment of water table fluctuations on coarse sand, Pb²⁺ migrated nearly 5 cm upward from the original pollutant and migrated less than 10 cm downward from that. In our experiments on medium and fine sand, the upward and downward migration distances were <5 cm. The groundwater table fluctuations, pH variation, and Pb concentration currently influence the migration of Pb.

Keywords: kinetic adsorption and desorption; groundwater table fluctuations; Pb; migration; experimental study

Citation: Qu, J.; Yan, T.; Zhang, Y.; Li, Y.; Tian, R.; Guo, W.; Jiang, J. An Experimental Study on the Migration of Pb in the Groundwater Table Fluctuation Zone. *Appl. Sci.* **2022**, *12*, 3870. <https://doi.org/10.3390/app12083870>

Academic Editor: Bing Bai

Received: 1 March 2022

Accepted: 10 April 2022

Published: 12 April 2022

Publisher's Note: MDPI stays neutral with regard to jurisdictional claims in published maps and institutional affiliations.



Copyright: © 2022 by the authors. Licensee MDPI, Basel, Switzerland. This article is an open access article distributed under the terms and conditions of the Creative Commons Attribution (CC BY) license (<https://creativecommons.org/licenses/by/4.0/>).

1. Introduction

As an essential water source, groundwater plays a significant role in supplying urban and rural residents with water. The water table fluctuates under natural and human factors, such as rainfall, evaporation, exploitation [1], and recharge [2]. The area between the highest and lowest groundwater table is referred to as the groundwater table fluctuation zone [3,4]. Water table fluctuations allow both saturated and unsaturated soil to alternate within the environment. These fluctuations cause significant changes in the biochemical characteristics of that zone [5], including the adsorption, desorption, and dilution of pollutants, which correspondingly alter the groundwater environment. The influence of water table fluctuations on pollutant migration and transformation has attracted the attention of scholars.

Current studies mainly focus on solute migration and transformation, such as nitrogen [6], organic matter [7], heavy metals [8–10], and groundwater quality [11] under water table fluctuations. Liu et al. studied the nitrate change law under water table rise

using a sandbox model experiment, finding that the water environment gradually changed into a state of relative reduction, and the lateral flow of the experiment was conducive to the migration of nitrate [12]. Liu et al. studied the variation in nitrate concentration for two water table fluctuation conditions (the water table stayed constant and varied by 20 cm/10 days) [13]. Tian et al. adopted an experimental simulation involving three kinds of groundwater tables and different surface runoff velocities to study nitrate change laws on solute migrates to the soil surface. Their results showed that the solute transport process shares an essential relationship with surface runoff velocity and the groundwater table [14]. Wang et al. simulated and verified the regularity of soil salt migration under water table fluctuations at different groundwater depths using a laboratory column experiment with homogenous medium. They assumed that the capillary pressure and temperature field variation caused by water table fluctuations significantly influence the migration of organic pollutants [15]. Wang et al. used the TMVOC model (a numerical simulator for three-phase non-isothermal flow of water, soil gas, and a multi-component mixture of volatile organic chemicals) to simulate how benzene, toluene, ethylbenzene, and o-xylene (BTEX) migrate in areas caused by steam extraction under natural attenuation and groundwater table fluctuations [16]. Oostrom et al. used a two-dimensional sandbox to study the distribution of pollutants migrating from their source into soil and groundwater under water table fluctuations. They observed that pollutants migrate with the infiltrated water flow and dissolve when the water table rises, increasing the pollutant concentration in the sample solution [17]. Bustos Medina et al. studied iron hydroxide blockage in wells and its effect on groundwater table fluctuations. This blockage affects indexes such as the water table, pH, EC (electrical conductivity), and DO (dissolved oxygen). By adopting hydrogeochemical simulations, Medina et al. determined the minerals' reaction mode, such as iron ions and manganese ions in the aquifer [18]. Li et al. explored the nitrogen transport law for fluctuations in different water tables using laboratory-based column experiments and numerical simulation. Their results showed that groundwater table fluctuations influence the variation of dissolved oxygen in the solution and decrease the nitrate and ammonium concentrations, which is conducive to removing ammonium [19]. Liu et al. employed a numerical model to predict changes in Beijing's groundwater table when the South–North Water Diversion Project was open. They also analyzed changes to the vadose zone and the impact of solid waste on the groundwater environment [20]. On account of the South–North Water Diversion Project, Cao et al. analyzed chemical quality predictions in the Baoding Plain for when the groundwater table rises using hydrogeochemical simulations [21].

Heavy metals (Pb) pose potential risks to the soil ecosystem and human health [22–24]. China and other nations have focused on soil pollution prevention and control plans and the study of Pb migration characteristics [25,26]. Domestic and foreign scholars have studied the adsorption, desorption, and migration of heavy metal pollutants such as Cu, Cr, and Zn in soil [27–30]. Nonetheless, there are few reports on the migration laws of heavy metals under groundwater table fluctuations. Therefore, in this article, technical methods, including adsorption and desorption tests, water table fluctuation experiments, etc., were used to analyze the distribution characteristics of Pb in the vadose and saturated zones under different typical media. Our methods help research the migration of Pb in the groundwater table fluctuation zone and provide theoretical support for heavy metal pollution treatments for soil and groundwater, remediation, and protection.

2. Materials and Methods

2.1. Sample Collection and Process

The sample medium used in our laboratory was collected from the floodplain of the Yellow River in Mengjin District, Luoyang City, Henan Province. The sampling location is scoured by the Yellow River all the year round. As a result, the soil medium is relatively clean, and the background concentration of Pb is small, which has little influence on the laboratory experiment. Laboratory experiments need to separate sand into coarse medium and fine medium. The sample sand was collected and processed using the Technical

Specification for Soil Environmental Monitoring's quarter method [31]. Then, the sample sand was dried and crushed in the laboratory. Finally, the sample was divided into three typical media, including coarse, medium, and fine sand in the pH range of 8.5–9.3 with an organic matter content range of 0.241–1.070 g·kg⁻¹. The basic physical and chemical properties of the soil are shown in Table 1.

Table 1. Physical and chemical properties of soil.

Sample	Particle Size (mm)	pH	Organic Matter Content (g·kg ⁻¹)
Coarse sand	0.5–1.0	8.5	0.241
Medium sand	0.25–0.5	8.8	0.587
Fine sand	0.125–0.25	9.3	1.070

2.2. Experimental Equipment

The following devices were employed for the adsorption and desorption kinetic aspects of Pb²⁺: a digital water bath oscillator, high-speed desktop centrifuge, and microwave.

The experimental devices for water table fluctuations include a 90 cm long column, water tank with 25 L volume, peristaltic pump with 100 rpm speed, piezometer tube, and soil solution sampler. We set eight openings for sampling in every column at heights of 20, 30, 35, 40, 45, 50, 55, and 60 cm. The experimental devices are shown in Figure 1.

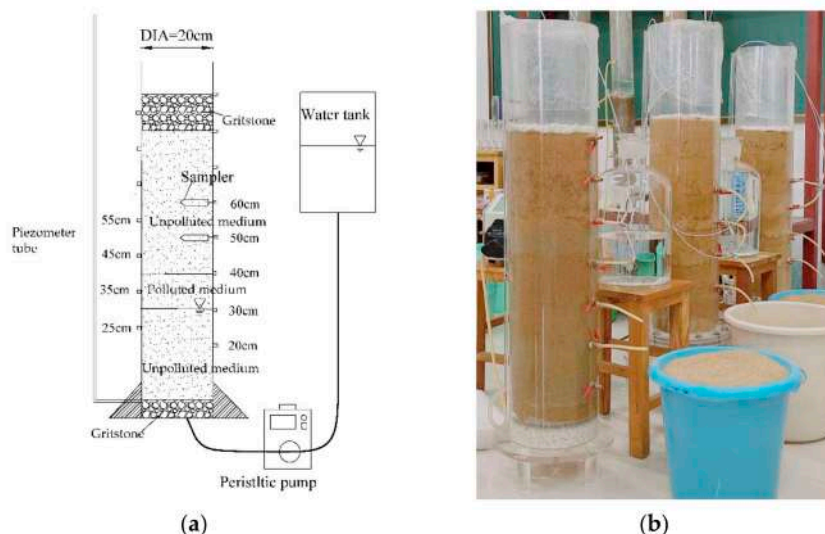


Figure 1. Experimental devices for the water table fluctuations. (a) The schematic diagram. (b) The field experiment diagram.

2.3. Experimental Methods

2.3.1. Adsorption and Desorption Experimental Methods of Pb

In this work, we completed the adsorption and desorption experiments, including the adsorption kinetics experiment, the desorption kinetics experiment, and the Pb adsorption and desorption quantities due to pH variation, in the laboratory. The experimental principle for adsorption was as follows: For the experiment, 50 mL of a 200 mg·L⁻¹ Pb(NO₃)₂ solution was prepared mixing sample sand (the sample sand was divided into coarse, medium, and fine sand). After mingling, the supernatant liquids, which were samples obtained in 5, 10, 15, 20, 30, 60, 90, 120, 180, 240, 360, 480, 720, and 1440 min, passed through the oscillator for centrifugal filtration. The experimental principle for desorption was as follows. The desorption process resembles the first step of the adsorption process, i.e., the pollutant was

mixed with the sand medium. After shaking this mixture for 24 h, the filtered samples were passed through centrifugal filtration. Then, 50 mL of a 0.01 mg·L⁻¹ NaNO₃ solution appended the filtered samples. The desorption time was the same as the adsorption time. The supernatant liquids were left behind by the oscillator via centrifugal filtration. The adsorption experiment at pH range of 4 to 6 and desorption experiment at pH range of 4 to 9 were as follows: Combining 50 mL of 500 mg·L⁻¹ Pb(NO₃)₂ solution with 10 g of sample sand, the pH of the background solution was adjusted to target values, such as pH 4, 5, 6, with either HCl or NaOH. When reaching the equilibrium (1440 min), the supernatant liquids and residue for adsorption were obtained through centrifugal filtration. The residue was obtained at the end of the experiment on the adsorption due to pH variation. The solutions at pH 4, 5, 6, 7, 8, 9 were added to the residue. Then the mixture was shaken using oscillator (200 rpm·min⁻¹), the supernatant liquids for desorption were obtained through centrifugal filtration. The following equations reveal the calculation formulae for the adsorption and desorption capacities [32]:

$$Q_{\text{ads}} = \frac{V(C_1 - C_2)}{M} \quad (1)$$

$$Q_{\text{des}} = \frac{VC_3}{M} \quad (2)$$

where Q_{ads} is the adsorption capacity for the medium (mg·kg⁻¹), Q_{des} is the desorption capacity for the medium (mg·kg⁻¹), V is the supernatant volume (mL), C_1 is the original concentration for adsorption aspect (mg·L⁻¹), C_2 is the supernatant concentration for adsorption aspect (mg·L⁻¹), M is the mass of the sand sample (g), C_3 is the supernatant concentration for desorption aspect (mg·L⁻¹).

2.3.2. Experimental Methods for Water Table Fluctuations

The columns were filled with sand collected and processed from the field, including coarse, medium, and fine sand. The column was filled with gritstone around the 5 cm length, unpolluted medium around the 30 cm length, polluted medium around the 10 cm length, unpolluted medium around the 40 cm length, and gritstone around the 10 cm length, respectively, from bottom to top. A Pb(NO₃)₂ solution was mixed with the sample sand to produce 2000 mg·kg⁻¹ contaminated mixture. After loading, the deionized water at pH 7 flowed up from the base of the column, whose pressure tube was used to measure the water table. The peristaltic pump controlled the water table variation, rising or falling. The initial water table was set in the column at the beginning of the experiment at about 20 cm high. Then, the water table was adjusted to increase 10 cm per day until it had continuously risen to 60 cm by adjusting the peristaltic pump. The same method was applied to the water table decrease, which decreased 10 cm per day until it reached a height of 20 cm. This process represented the completion of one water table fluctuation cycle. In the column for water table fluctuations, two cycles were continuously conducted. Figure 2 shows how the water table varies with time. In order to further understand the migration process of Pb in the medium under water table fluctuations, the Pb²⁺ concentration adsorbed in the medium was measured by digestion treatment after the experiment. The sampling medium was obtained from the 20–60 cm height at an interval of 5 cm.

2.3.3. Experimental Test Instrument

According to the groundwater quality standard (GB/T 14848-2017) and other standards, the Pb concentrations for the sample solution and sample sand were detected by a flame atomic adsorption spectrophotometer (FAAS, Manufacturer: Beijing Ruili Analytical Instrument Co. Ltd., Beijing, China). The pH of the solution was detected using the glass electrode method (Micro600, Manufacturer: Palintest Co. Ltd., Newcastle, UK). The medium sample was digested under microwave irradiation. The Pb contents were determined by FAAS.

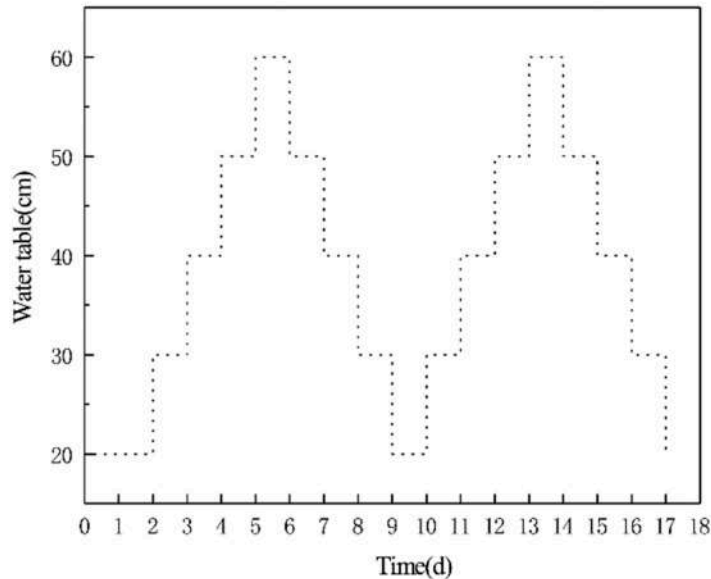


Figure 2. Water table fluctuations process.

3. Results and Discussion

3.1. The Curve of Adsorption and Desorption Kinetics

Figure 3 shows the curves of adsorption and desorption kinetics of Pb. The adsorption and desorption capacities of Pb^{2+} in the three sand media were significantly dissimilar. The adsorption and desorption quantity reached equilibrium in 1440 min. The maximum adsorption capacity of fine sand, medium sand, and coarse sand were $2366.6 \text{ mg}\cdot\text{kg}^{-1}$, $1847.6 \text{ mg}\cdot\text{kg}^{-1}$, and $1543.8 \text{ mg}\cdot\text{kg}^{-1}$, respectively. The maximum desorption capacity of coarse sand, medium sand, and fine sand were $81.6 \text{ mg}\cdot\text{kg}^{-1}$, $62.38 \text{ mg}\cdot\text{kg}^{-1}$, and $29.18 \text{ mg}\cdot\text{kg}^{-1}$, respectively. Compared to the hyperbolic diffusion model, pseudo-second-order model and Weber–Morris model, the data fit well to the Elovich model against various time ranges because the minimum R^2 value was 0.90. The fitting parameters are shown in Table 2. Based on the adsorption kinetics experiment data, Pb^{2+} in the contaminated solution was adsorbed rapidly onto the sampling sand within 240 min. The adsorption quantity gradually was stable from 240 to 1440 min in the experiment; this implies several points that adsorb Pb^{2+} quickly on the medium surface at the initial stage. The effective points that adsorb Pb^{2+} gradually decreased with increasing reaction time, which gradually weakened the adsorption capacity until it reached equilibrium. The experiment's result aligned with the study of Ren, L. [33]. The same conditions occurred in the desorption kinetics experiment.

Figure 4 illustrates the effects of pH on the adsorption and desorption of sand medium. The adsorption capacity of Pb^{2+} in three sand media gradually increased at pH range of 4 to 6. The desorption capacity gradually decreased with increasing pH and the desorption quantity steadily approached equilibrium when the pH was between 8 and 9. Fine sand's adsorption and desorption capacities showed almost no change at different pH levels compared with medium and coarse sand. When the pH increased, the competitive adsorption sites of hydrogen ions in the medium decreased, and heavy metals mainly existed in the combined state of hydroxide or carbonic acid. This state is not conducive to their migration in the medium and increases adsorption capacity. These experimental conclusions are consistent with the literature [30,34].

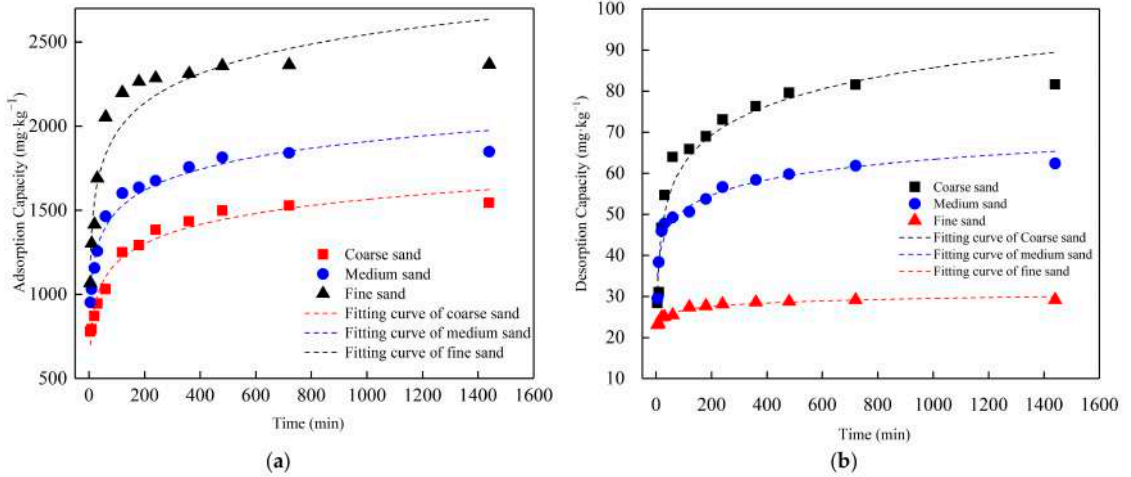


Figure 3. Curves of adsorption and desorption kinetics of Pb in different media: (a) the adsorption quantity variation of Pb based on adsorption kinetics; (b) the desorption quantity variation of Pb based on desorption kinetics.

Table 2. Kinetic parameters for adsorption and desorption of Pb in different media.

Category	Media	Elovich Equation			Hyperbolic Diffusion Equation			Pseudo-Second-Order Equation		Weber–Morris Equation		
		a_1	b_1	R^2	a_2	b_2	R^2	k_1	R^2	k_2	c	R^2
adsorption	Coarse sand	437.20	163.15	0.96	0.5513	0.0159	0.81	0.00005	0.72	24.52	851.0	0.81
	Medium sand	667.04	179.76	0.97	0.6171	0.0140	0.74	0.00006	0.83	25.81	1139.9	0.74
	Fine sand	799.14	252.62	0.90	0.6326	0.0143	0.60	0.00005	0.95	33.89	1497.1	0.60
desorption	Coarse sand	15.18	10.21	0.94	0.5208	0.0176	0.69	0.0008	0.96	1.43	42.50	0.69
	Medium sand	26.14	5.39	0.94	0.6465	0.0124	0.72	0.0022	0.81	0.77	40.33	0.72
	Fine sand	21.00	1.24	0.97	0.8298	0.0062	0.76	0.0165	0.55	0.18	24.21	0.76

Note: The data were fitted to the Elovich equation: $Q = a_1 + b_1 \ln t$, the hyperbolic diffusion equation: $Q/Q_{max} = a_2 + b_2 t^{1/2}$, the pseudo-second-order equation: $Q = k_1 Q_{max}^2 t / (1 + k_1 Q_{max} t)$ and the Weber–Morris equation: $Q = k_2 t^{1/2} + c$, respectively, where Q is the adsorption/desorption capacity; t is time; a_1 and a_2 refer to constant associated with maximum adsorption/desorption amount for the Elovich equation and the pseudo-second-order equation, respectively, b_1 and b_2 refer to adsorption/desorption rate coefficient, k_1 and k_2 refer to adsorption/desorption rate coefficient for pseudo-second-order model and Weber–Morris model, respectively, c is constants related to the medium for Weber–Morris model, Q_{max} refers the equilibrium adsorption/desorption capacity for coarse sand, medium sand and fine medium.

3.2. pH Variation of Sample Solution on Water Table Fluctuation Zone

In Section 3.1, pH is one of the major factors affecting the adsorption and desorption capacities of Pb. Figure 5 illustrates pH variation at different sampling port heights in the water table fluctuation experiment on three typical media. The average pH variation at different sampling port heights is shown in Figure 6. The vertical direction of the column shows the distribution properties of pH in the sample solution. Firstly, pH decreased and then increased from the top to the bottom. The lowest pH often occurred at the height of 35 cm (pH = 4.7), where the location of original pollutants was consistent. The average pH of the three typical media followed the sequence of fine sand > medium sand > coarse sand. The aforementioned changes may be attributed to the increasing groundwater table since Pb^{2+} was not only adsorbed by the adsorption sites on the surface of soil particles, but also possibly combined with OH^- ions to obtain $Pb(OH)_2$ precipitation. Consequently, the concentration of OH^- ions decreased, so that the pH decreased in the solution, which resulted in a higher pH the further the distance. As the water table rose, the Pb^{2+} in the

solution was absorbed to saturation by the medium. A pH range from 4.5 to 7.5 was detected in the sample solution by coarse sand, at pH range from 5.1 to 7.8 by medium sand, and a pH range from 7.1 to 7.7 by fine sand. A comparison of the average pH values for the three typical media revealed that pH at different grain diameters generally followed the order of: coarse sand > medium sand > fine sand.

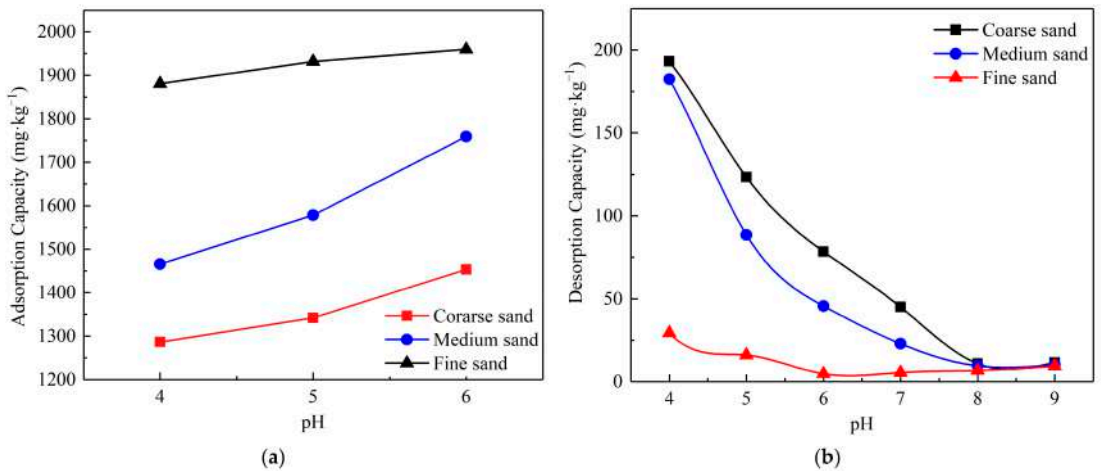


Figure 4. Effects of pH on adsorption (a) and desorption (b) on different media, including coarse, medium, and fine sand.

3.3. Migration Law of Pb Due to Water Table Fluctuations

Due to the strong adsorption capacity of fine sand, the migration ability of Pb in fine sand is weak. The Pb of each sample solution in the columns did not reach the instrument's detection limit (the instrument's detection limit (TAS-990A) is 0.01 mg/L). Therefore, we only analyzed the migration law of Pb in coarse and medium sand in this article. During groundwater table fluctuations, the variation in Pb concentration at different sample solutions is shown in Figure 7a (coarse sand) and Figure 7b (medium sand). The results of how Pb concentration is altered with water table fluctuations are shown in Table 3 and can be used to study the migration of Pb when the water table rises and falls in the experiment. Our analysis is as follows. (1) In the sample solution, when the height was 30 cm high in coarse sand, the water table height increased from 20 to 40 cm, and Pb^{2+} concentration increased in the range of 8.29–42.42% in the early-stage relative to the initial concentration on the first day. Then, with the water table fluctuations, Pb^{2+} concentration decreased in the range of 37.12–94.34%. This concentration declined by 9.54% on average within 8 days. (2) At the height of 35 cm for sample solutions in coarse sand, Pb^{2+} concentration decreased in the range of 4.01–97.47% with water table fluctuations. This concentration decreased by 6.68% on average within 14 days. (3) At the height of 40 cm for the sample solution in coarse sand, the concentration declined by 5.54% on average within 12 days. (4) At the height of 45 cm for the sample solution, Pb^{2+} was absorbed by coarse sand after 4 days. (5) At the heights of 30 and 40 cm for the sample solution in medium sand, Pb^{2+} was only detected on the first day. Afterward, Pb^{2+} was completely absorbed by the medium. (6) At the 30 and 40 cm heights for the sample solution in medium sand, Pb^{2+} concentration decreased in the range of 24.26–100%. This concentration decreased by 7.57% on average until the water table fluctuated at between 50 and 60 cm.

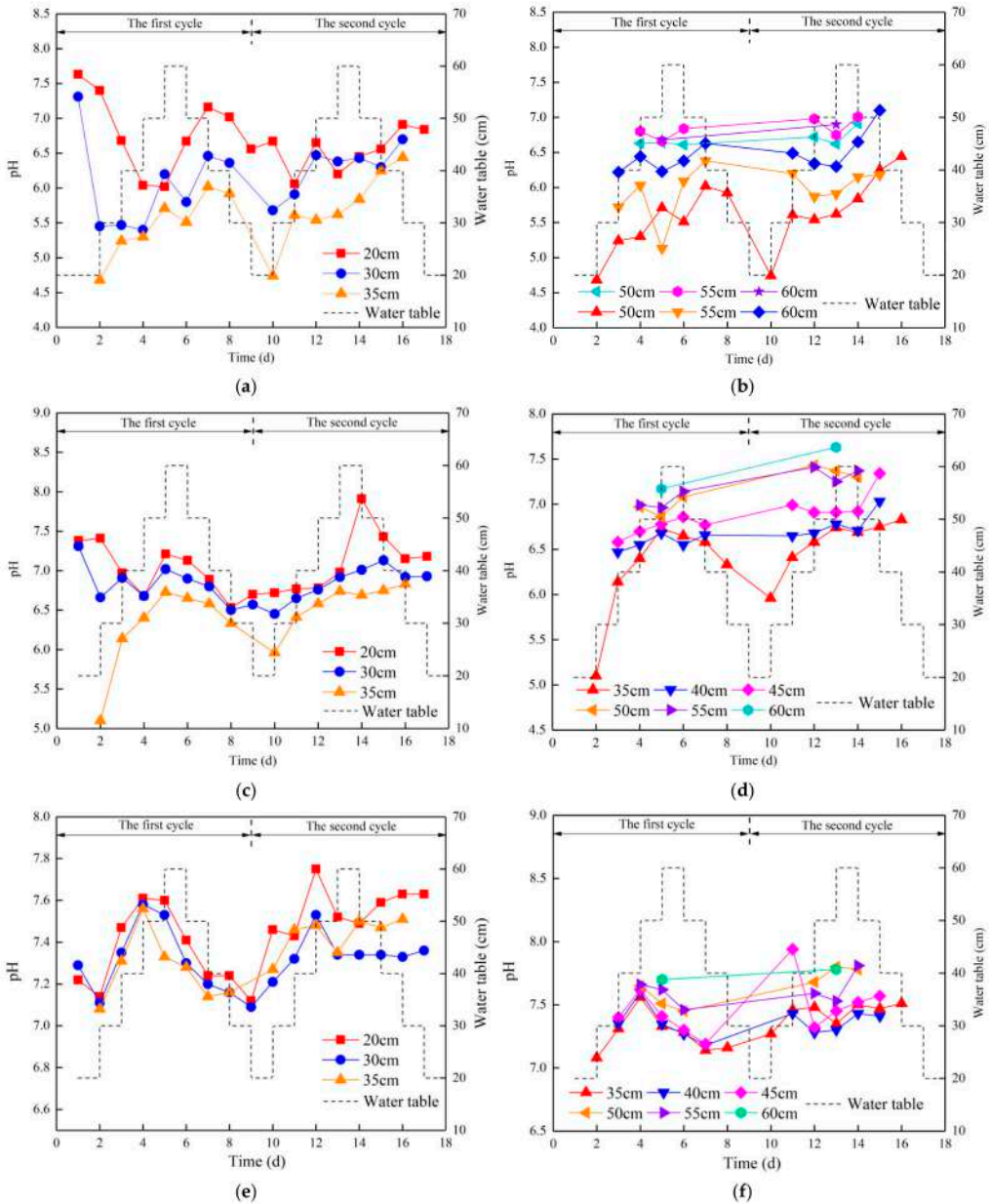


Figure 5. pH variation at different heights of sampling locations in the first and second cycles: (a) pH variation of coarse sand at sampling positions with heights of 20, 30, and 35 cm; (b) pH variation of coarse sand at sampling positions with heights of 35, 40, 45, 50, 55, and 60 cm; (c) pH variation of medium sand at sampling positions with heights of 20, 30, and 35 cm; (d) pH variation of medium sand at sampling positions with heights of 35, 40, 45, 50, 55, and 60 cm; (e) pH variation of fine sand at sampling positions with heights of 20, 30, and 35 cm; (f) pH variation of fine sand at sampling positions with heights of 35, 40, 45, 50, 55, and 60 cm.

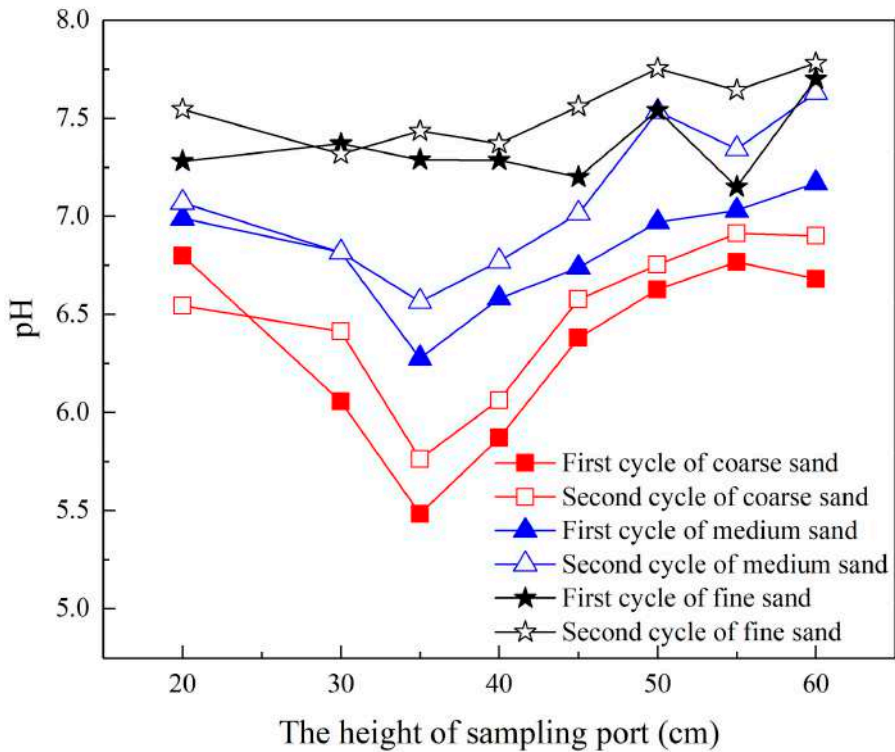


Figure 6. Average pH at different heights of sampling locations.

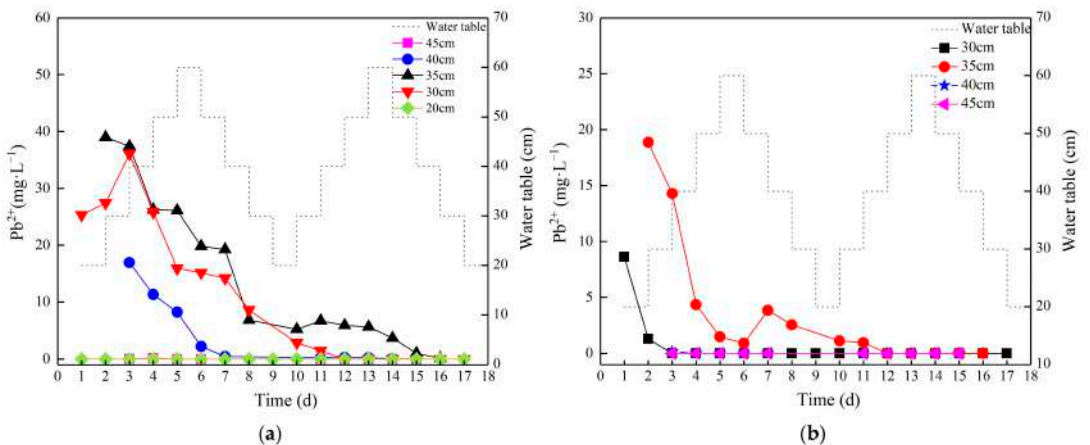


Figure 7. The Pb^{2+} concentrations vary in water table fluctuations. (a) The Pb^{2+} concentrations vary in columns filled with coarse sand; (b) the Pb^{2+} concentrations vary in columns filled with medium sand.

As seen in the analysis in Figure 5 of the pH and the water table, the closer the sample solution was to the pollutant in the rising water table, the lower the pH became, the greater the activity of Pb became, and the more desorption quantities resulted from polluted sand.

Therefore, at the height of 35 cm for the sample solution, Pb^{2+} concentration reached its maximum compared with the others. When the sample solutions were further away, the maximum concentration of Pb^{2+} was smaller. In a column of coarse sand, when the water table rose to 30 cm, the desorption quantity of Pb^{2+} reached its maximum, and the Pb^{2+} concentration in the solution reached its maximum. Throughout the whole experiment, the maximum concentration of Pb^{2+} at the 20, 30, 35, 40, and 45 cm sample solutions were 0.072, 36.061, 38.973, 16.941, and 0.042 $mg \cdot L^{-1}$, respectively. Figure 7b shows that the adsorption capacity of medium sand is greater than that of coarse sand; therefore, the migration capacity of Pb^{2+} in medium sand becomes weak compared with that in coarse sand. Based on Figure 7b, Pb^{2+} is only detected at the heights of 30, 35, and 40 cm. In these sample solutions, the highest concentrations are 8.619, 18.862, and 0.164 $mg \cdot L^{-1}$, respectively.

Table 3. Variation range of concentration of Pb in coarse and medium sand sampling ports with water table fluctuations.

Media	How Did the Water Table Fluctuate	Concentration Variation of Pb in the First Cycle (Compared with the Initial Concentration)				Concentration Variation of Pb in the Second Cycle (Compared with the Initial Concentration)			
		Sampling Port with Height of 40 cm	Sampling Port with Height of 35 cm	Sampling Port with Height of 40 cm	Sampling Port with Height of 45 cm	Sampling Port with Height of 30 cm	Sampling Port with Height of 35 cm	Sampling Port with Height of 40 cm	Sampling Port with Height of 45 cm
Coarse sand	20→30 cm	8.29%	-	-	-	-	-	-	-
	30→40 cm	42.42%	-4.01%	-	-	-88.82%	-86.67%	-	-
	40→50 cm	2.00%	-32.66%	-33.14%	285.71%	-94.34%	-82.83%	-98.91%	-
	50→60 cm	-37.12%	-33.04%	-51.56%	-100.00%	-	-84.93%	-98.48%	-
	60→50 cm	-40.23%	-49.12%	-87.05%	-	-	-85.60%	-98.82%	-
	50→40 cm	-43.94%	-50.60%	-97.42%	-	-	-90.68%	-99.68%	-
	40→30 cm	-65.96%	-82.47%	-	-	-	-97.47%	-	-
	30→20 cm	-	-	-	-	-	-	-	-
Medium sand	20→30 cm	-85.09%	-	-	-	-	-	-	-
	30→40 cm	-	-24.26%	-	-	-	-94.05%	-	-
	40→50 cm	-	-76.93%	-100.00%	-	-	-94.94%	-	-
	50→60 cm	-	-92.21%	-	-	-	-100.00%	-	-
	60→50 cm	-	-95.21%	-	-	-	-	-	-
	50→40 cm	-	-79.59%	-	-	-	-	-	-
40→30 cm	-	-86.50%	-	-	-	-	-	-	

Note: During the whole experiment, the concentrations in the solution sample at each sampling port did not reach the detection limit for columns filled with fine sand because of the strong adsorption capacities of fine and medium sand; therefore, they are not listed in this table. The “-” in the table indicates that the water sample was not obtained due to water table fluctuation limitations.

The experimental results of groundwater fluctuation showed that the underground water table rose to a height of 30 cm in coarse and medium sand after coming into contact with pollutants. The capillary band rose when the moisture content of the medium increased at the height of 30 cm. Then, Pb^{2+} in the medium dissolved into water under the effect of desorption. Pb^{2+} in the solution was still detectable since the water table fluctuated rapidly and Pb^{2+} in the solution had not been fully adsorbed by the medium. Reasons for why the concentration of Pb^{2+} decreased as the water table rose are as follows. (1) Due to the alkaline soil, the solution’s pH increased with the rising water table, resulting in OH^- and Pb^{2+} combining in the water to form precipitation. (2) The adsorption quantity of the unpolluted medium was stronger than that of the pollution medium. The rising of the water table brought about Pb^{2+} adsorption one more time. (3) The adsorption and desorption of Pb is affected by hydrodynamic conditions. The change in hydrodynamic conditions caused Pb^{2+} to be desorbed and Pb^{2+} adsorbed by the medium. These two reactions were mutual until the adsorption equilibrium was reached.

3.4. Migration Characteristics of Pb in Soils with a Fluctuating Water Table

Figure 8 shows how the contents of Pb adsorbed by the sand sample varied at different heights. The maximum Pb content occurred at the height of 35 cm in three columns. Trace amounts of Pb were detected at the height range of 25–45 cm. The analyses in Figures 5

and 8 show that the maximum Pb content occurred where the minimum pH was detected. Therefore, the presence of heavy metal Pb decreases pH as a consequence of acidic soil. Zhai L et al. determined that precipitates and complexes may solidify the soil, causing grievous pollution to soils and crops [35].

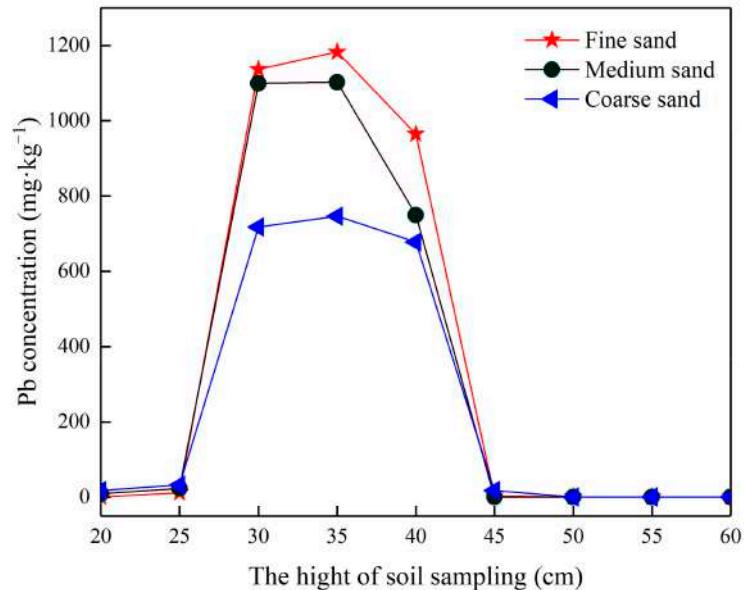


Figure 8. The variation of Pb concentration in the medium at different heights after experiments.

As the water table fluctuated, Pb^{2+} migrated upward or downward in the medium, but the migration distance of Pb^{2+} was more positively affected by the adsorption. The migration distance of Pb^{2+} in coarse sand was further than that in the medium sand or fine sand. The water table varied in coarse sand, the upward migration distance was only 5 cm high, and the downward migration distance was <10 cm high. In medium and fine sand, the upward and downward migration distance height was <5 cm.

4. Conclusions

- In the adsorption and desorption kinetic experiments for fine, medium, and coarse sand, the maximum adsorption capacity of Pb^{2+} was $2367 \text{ mg}\cdot\text{kg}^{-1}$, $1848 \text{ mg}\cdot\text{kg}^{-1}$, and $1544 \text{ mg}\cdot\text{kg}^{-1}$, respectively. The maximum desorption capacity of Pb^{2+} was $29.18 \text{ mg}\cdot\text{kg}^{-1}$, $62.38 \text{ mg}\cdot\text{kg}^{-1}$, and $81.60 \text{ mg}\cdot\text{kg}^{-1}$, respectively. For adsorption and adsorption experiments at different pH levels, the adsorption capacity of Pb^{2+} gradually increased and the desorption capacity gradually decreased with increasing pH in the sample solution at pH 4.0 and above. In these experiments, the desorption capacity held steady with an increase in pH from 8.0 to 9.0;
- In the water table fluctuation experiments, the pH detected in the sample solution varied with the water table fluctuation. The location was further away from the origin pollution we set, resulting in decreased pH in the sample solution. The minimum pH was consistent with the original pollution. At the same sample port, this universally followed the order of the medium's average pH: fine sand > medium sand > coarse sand. The Pb^{2+} concentration in the sample solution varies with time and water table fluctuations. Pb concentration in the medium results in Pb^{2+} forming desorption products in the solution that adsorb the experimental medium surfaces once again;

- The migration of Pb^{2+} is affected by pH in the solution, water table fluctuations, and the adsorption capacity of the medium. Water table fluctuations affect the desorption of Pb in the polluted medium. Consequently, the Pb^{2+} concentration in the solution changes. Then, the pH variation results in the adsorption and desorption capacities of Pb^{2+} changing as well;
- The effects of Pb's migration on groundwater table fluctuation zones are due to various factors. In this article, we only considered the water table, pH, and adsorption and desorption capacities in our analysis, which are the deficiencies of this work. Other meaningful factors will be added for future studies, such as dissolved oxygen, redox potential, etc.

Author Contributions: Conceptualization, J.Q.; methodology, T.Y.; validation, Y.Z.; formal analysis, Y.L.; investigation, R.T.; resources, W.G.; data curation, J.J.; writing—original draft preparation, J.Q.; writing—review and editing, J.Q. and T.Y.; funding acquisition, J.Q. All authors have read and agreed to the published version of the manuscript.

Funding: This research was funded by the Key R&D and Promotion Projects in Henan Province (202102310012), the Doctoral Research Fund of North China University of Water Resources and Electric Power (40651), and the Key Project of Science and Technology Research of Henan Education Department (14A170006).

Institutional Review Board Statement: Not applicable.

Informed Consent Statement: Not applicable.

Data Availability Statement: Data are contained within the article.

Conflicts of Interest: The authors declare no conflict of interest.

References

1. Li, W.; Wang, L.; Yang, H.; Zheng, Y.; Cao, W.; Liu, K. The groundwater overexploitation status and countermeasure suggestions of the North China Plain. *China Water Resour.* **2020**, *13*, 26–30.
2. Zhang, C.; Duan, Q.; Yeh, P.J.F.; Pan, Y.; Gong, H.; Gong, W.; Di, Z.; Lei, X.; Liao, W.; Huang, Z.; et al. The Effectiveness of the South-to-North Water Diversion Middle Route Project on Water Delivery and Groundwater Recovery in North China Plain. *Water Resour. Res.* **2020**, *56*, 10. [[CrossRef](#)]
3. Liu, X.; Zuo, R.; Wang, J.; He, Z.; Li, Q. Advances in researches on ammonia, nitrite and nitrate on migration and transformation in the groundwater level fluctuation zone. *Hydrogeol. Eng. Geol.* **2021**, *48*, 27–36.
4. Mu, E.; Ou, Y.; Dong, S.; Yang, J. Summary of research progress on groundwater level management. *Ground Water* **2019**, *41*, 33–34.
5. Rezaezhad, F.; Couture, R.M.; Kovac, R.; O Connell, D.; Van Cappellen, P. Water table fluctuations and soil biogeochemistry: An experimental approach using an automated soil column system. *J. Hydrol.* **2014**, *509*, 245–256. [[CrossRef](#)]
6. Zhang, D.; Cui, R.; Fu, B.; Yang, Y.; Wang, P.; Mao, Y.; Chen, A.; Lei, B. Shallow groundwater table fluctuations affect bacterial communities and nitrogen functional genes along the soil profile in a vegetable field. *Appl. Soil Ecol.* **2020**, *146*, 103368. [[CrossRef](#)]
7. Liu, Y.; Ding, A.; Liu, B.; Liang, X.; Li, S.; Zhang, L.; Yin, H. A review of the petroleum hydrocarbon contamination transformation performance in the zone of intermittent saturation. *Sci. Technol. Eng.* **2018**, *18*, 172–178.
8. Wu, Z.; Liu, G.; Qian, J.; Wei, Y.; Yue, Q. Experimental Study on the Vertical Migration of Pb from the Saturated Zone to Unsaturated Zone. *Environ. Sci. Technol.* **2019**, *42*, 36–41.
9. Rezaei, A.; Hassani, H.; Hassani, S.; Jabbari, N.; Fard Mousavi, S.B.; Rezaei, A. Evaluation of Groundwater Quality and Heavy Metal Pollution Indices in Bazman Basin, Southeastern Iran. *Groundw. Sustain. Dev.* **2019**, *9*, 100245. [[CrossRef](#)]
10. Rezaei, A.; Hassani, H.; Tziritis, E.; Fard Mousavi, S.B.; Jabbari, N. Hydrochemical characterization and evaluation of groundwater quality in Dalgan basin, SE Iran. *Groundw. Sustain. Dev.* **2020**, *10*, 100353. [[CrossRef](#)]
11. Yu, X. Groundwater Level Numerical Simulation Prediction and Its Environmental Influence Evaluation after the South-to-North Water Transferring Project. Master's Thesis, Jilin University, Changchun, China, 2004.
12. Liu, X.; Zuo, R.; Meng, L.; Li, P.; Li, Z.; He, Z.; Li, Q.; Wang, J. Study on the variation law of nitrate pollution during the rise of groundwater level. *China Environ. Sci.* **2021**, *41*, 232–238.
13. Liu, J.; Zhu, X.; Li, S.; Kang, L.; Ma, M.; Du, L. Effects of groundwater fluctuation on nitrate nitrogen transport after nitrogen application in cropland soil. *Chin. J. Eco-Agric.* **2021**, *29*, 154–162.
14. Tian, K.; Zhang, G.; Zheng, F. Chemical transport from soil into surface runoff under different ground-water tables. *J. Northwest A&F Univ.* **2009**, *37*, 193–200.
15. Wang, H.; Gao, W.; Ma, X. Research on the influence of groundwater level fluctuating on soil salin movement. *Sci. Technol. Innov. Her.* **2013**, *34*, 13–14.

16. Wang, Y.; Chen, L.; Yang, Y.; Li, J.; Tang, J.; Bai, S.; Feng, Y. Numerical simulation of BTEX migration in groundwater table fluctuation zone based on TMVOC. *Res. Environ. Sci.* **2020**, *33*, 634–642.
17. Oostrom, M.; Dane, J.H.; Wietsma, T.W. A review of multidimensional, multifluid, intermediate-scale experiments: Flow Behavior, Saturation Imaging, and Tracer Detection and Quantification. *Vadose Zone J.* **2007**, *6*, 610–637. [[CrossRef](#)]
18. Bustos Medina, D.A.; van den Berg, G.A.; van Breukelen, B.M.; Juhasz-Holterman, M.; Stuyfzand, P.J. Iron-hydroxide clogging of public supply wells receiving artificial recharge: Near-well and in-well hydrological and hydrochemical observations. *Hydrogeol. J.* **2013**, *21*, 1393–1412. [[CrossRef](#)]
19. Li, X.; Yang, T.; Bai, S.; Xi, B.; Zhu, X.; Yuan, Z.; Wei, Y.; Li, W. The effects of groundwater table fluctuation on nitrogen migration in aeration zone. *J. Agro-Environ. Sci.* **2013**, *32*, 2443–2450.
20. Liu, Y.; Sun, Y.; Yin, K. Prediction of groundwater environment in Beijing after water entering the capital by the South-north Water Diversion. *Hydrogeol. Eng. Geol.* **2005**, *05*, 93–96.
21. Cao, W.; Yang, H.; Gao, Y.; Nan, T.; Wang, Z.; Xu, S. Prediction of groundwater quality evolution in the Baoding Plain of the SNWDP benefited regions. *J. Hydraul. Eng.* **2020**, *51*, 924–935.
22. Cheng, X. Research progress of lead pollution on soil. *Ground Water* **2011**, *33*, 65–68.
23. Lee, J.; Son, Y.; Pratheeshkumar, P.; Shi, X. Oxidative stress and metal carcinogenesis. *Free Radic. Biol. Med.* **2012**, *53*, 742–757. [[CrossRef](#)] [[PubMed](#)]
24. Rezaei, A.; Hassani, H.; Fard Mousavi, S.B.; Jabbari, N. Evaluation of Heavy Metals Concentration in Jajarm Bauxite Deposit in Northeast of Iran Using Environmental Pollution Indices. *Malays. J. Geosci.* **2019**, *3*, 12–20. [[CrossRef](#)]
25. Shi, X.; Li, L.; Zhang, T. Water Pollution Control Action Plan, a Realistic and Pragmatic Plan—An Interpretation of Water Pollution Control Action Plan. *Environ. Prot. Sci.* **2015**, *41*, 1–3.
26. Ge, F.; Yun, J.; Xu, K.; Zhang, M.; Xu, L.; Li, Y.; Zhang, A. Progress of research on environmental criteria for lead in soil. *J. Ecol. Rural Environ.* **2019**, *35*, 1103–1110.
27. Singh, O.V.; Labana, S.; Pandey, G.; Budhiraja, R.; Jain, R.K. Phytoremediation: An overview of metallic ion decontamination from soil. *Appl. Microbiol. Biotechnol.* **2003**, *61*, 405–412. [[CrossRef](#)]
28. Singh, S.P.; Ma, L.Q.; Harris, W.G. Heavy Metal Interactions with Phosphatic Clay: Sorption and Desorption Behavior. *J. Environ. Qual.* **2001**, *30*, 1961–1968. [[CrossRef](#)]
29. Jacques, D.; Šimúnek, J.; Mallants, D.; van Genuchten, M.T. Modelling coupled water flow, solute transport and geochemical reactions affecting heavy metal migration in a podzol soil. *Geoderma* **2008**, *145*, 449–461. [[CrossRef](#)]
30. Zhang, R.; Yao, S.; Ao, Y. Vertical transport rules of Cu, Cd, Pb in the surface of soil. *J. Shanghai Jiaotong Univ. (Agric. Sci.)* **2013**, *31*, 67–71.
31. China National Environmental Monitoring Centre; Nanjing Environmental Monitoring Center Station. Technical Specification for Soil Environmental Monitoring (HJ/T 166-2004). Available online: <http://www.mee.gov.cn/image20010518/5406.pdf> (accessed on 9 December 2004).
32. Azouzi, R.; Charef, A.; Hamzaoui, A.H. Assessment of effect of pH, temperature and organic matter on zinc mobility in a hydromorphic soil. *Environ. Earth Sci.* **2015**, *74*, 2967–2980. [[CrossRef](#)]
33. Ren, L. Adsorption-Desorption Characteristics Research of Pb, Cr, Ni in Sediment and Soil. Master’s Thesis, Jilin Agricultural University, Changchun, China, 2017.
34. Zheng, S. Studies on the Transformation and Transport of Heavy Metals in Typical Chinese Agricultural Soi. Master’s Thesis, Zhejiang University, Hangzhou, China, 2010.
35. Zhai, L.; Chen, T.; Liao, X.; Yan, X.; Wang, L.; Xie, H. Pollution of agricultural soils resulting from a tailing spill at a Pb-Zn mine: A case study in Huanjiang Guangxi Province. *Acta Sci. Circumstantiae* **2008**, *6*, 1206–1211.